Spring 5-19-2017

Aerodynamics and Shock Buffet of a Transonic Airfoil in Ground Effect

Boshun Gao
Washington University in St. Louis

WASHINGTON UNIVERSITY IN ST. LOUIS

School of Engineering and Applied Science
Department of Mechanical Engineering and Material Science

Thesis Examination Committee:
Ramesh Agarwal, Chair
David Peters
Qiulin Qu

Aerodynamics and Shock Buffet of a Transonic Airfoil in Ground Effect

by

Boshun Gao

A dissertation presented to the School of Engineering and Applied Science
of Washington University in St. Louis
in partial fulfillment of the requirements for the degree of
Master of Science

May 2017
St. Louis, Missouri

Table of Contents

List of Figures

List of Tables

Nomenclature

C_D	=	drag coefficient
C_L	=	lift coefficient
$C_{D,low}$	=	drag coefficient on the lower surface of the airfoil
$C_{L,low}$	=	lift coefficient on the upper surface of the airfoil
$C_{D,up}$	=	drag coefficient on the lower surface of the airfoil
$C_{L,up}$	=	lift coefficient on the upper surface of the airfoil
C_p	=	pressure coefficient
α	=	angle of attack
c	=	chord length of the airfoil
h	=	ground clearance
p	=	local pressure
p_∞	=	freestream pressure
U_∞	=	freestream velocity
T	=	time of one period
t*	=	nondimensional time
$\boldsymbol{n}$	=	unit vector normal to the airfoil surface
$\boldsymbol{j}$	=	unit vector along y axis
$\boldsymbol{\tau}$	=	shear stress on the airfoil surface
f	=	frequency
ρ	=	air density
T	=	time period in unsteady simulation

M	=	Mach number
Re	=	Reynolds number based on chord length
Δt	=	time step for the unsteady simulation
y^+	=	dimensionless wall distance of the first mesh layer
f	=	frequency
k	=	reduced frequency

Acknowledgments

I would like to take this opportunity to express my appreciation to those who helped me with various aspects during my research in computation fluid dynamics lab at Washington University in St. Louis.

First of all, I want to thank Professor Ramesh Agarwal for his guidance and patience throughout my research. His talent, both industrial and academic rich CFD experience inspired and encouraged me to explore the academic world in fluid dynamics.

I would like to thank Dr. Qiulin Qu for all the effort he put in to help me from the very beginning to the very end. The brilliant mind of Dr. Qu combined with his experience in fluid dynamics has contributed immensely to this thesis. I would also like to thank Xu Han for exchanging ideas during this research; his knowledge in computer science and fluid dynamics helped me enormously.

I would also like to thank my another committee member, Dr. Peters, for taking the time to read this thesis and attend the defense.

Boshun Gao

Washington University in St. Louis

May 2017

Dedication

I would like to dedicate this thesis to my parents (Qingnian Gao and Xiuling Wu) for their unconditional support.

I will never succeed without their guidance, influence and encouragement.

ABSTRACT OF THE THESIS

Aerodynamics and Shock Buffet of a Transonic Airfoil in Ground Effect

by

Boshun Gao

Master of Science in Mechanical Engineering

Washington University in St. Louis, 2017

Research Advisor: Professor Ramesh K. Agarwal

The Wing in Ground Effect (WIG) aircraft operates with larger lift to drag ratio compared to a conventional aircraft at low subsonic Mach numbers. To increase the traffic volume of the WIG aircraft, one possible way is to increase the flight speed, which can result in transonic flow. Currently the studies on transonic flight in ground effect are very few. The goal of this research is to study the aerodynamics and flow physics of a typical transonic RAE2822 airfoil at angles of attack (AOA) from 0 to 12 deg. and Mach numbers from 0.5 to 0.8 in ground effect by varying the ground clearance above the ground. The compressible Reynolds-Averaged Navier-Stokes equations with Spalart-Allmaras (SA) turbulence model are solved using the commercial CFD solver ANSYS FLUENT. For flight near the flat ground surface, some interesting shock formations and flow phenomenon are obtained due to transonic flow. For the unsteady shock buffet phenomenon on the upper surface, the buffet boundary in the Angle of Attack (AOA) – Mach number (Ma) plane shrinks with the decreasing ground clearance. Compared to the unbounded flow field, there exists a steady shock on the lower surface of the airfoil in ground effect for low

AOAs because the channel between the lower surface of the supercritical airfoil and the ground is a typical converging-diverging shape, resulting in decrease in lift and increase in drag. For extreme conditions of very small ground clearance, small AOA and high Mach numbers, a new coupling between the shock buffets on the lower and the upper surface of the airfoil is observed. The unsteady aerodynamics of transonic flow in the presence of a wavy ground is also analyzed. For flight on the wavy ground, there is phase lead in the unsteady aerodynamic performance of the airfoil at various ground clearance compared to that in case of flat ground.

Chapter 1: Introduction

This part introduces the background of the ground effect, transonic flight, and the shock buffet phenomenon. The simulation software used in this research is also briefly described.

1.1 Ground Effect

Typical commercial aircraft fly at around 35000 feet above the ground at Mach number around 0.8. However, a Wig aircraft also needs to operate safely near a flat ground or wavy surface like river or ocean. The ground effect is favorable for a WIG craft since the ground effect can increase the effective angle of attack thereby increasing the aerodynamic efficiency (L/D) of the WIG [1-5] resulting in less fuel consumption and higher operating efficiency. A wing-in ground (WIG) aircraft cruises near height which is generally a ground less than the length of the aircraft's wingspan to generating extra lift by having a high-pressure distribution on the lower surface of the airfoil. WIG aircraft usually fly at low subsonic Mach number < 0.3. For subsonic flow past an airfoil in ground effect, numerous experiments and simulations have been conducted over the years. Aerodynamic ground effect of NACA6409 was experimentally investigated by Jung et al. [6] to investigate the influence of aspect ratio of the wing, end plates, angles of attack (AOA), and ground clearance. Zhang et al. [7] experimentally studied the aerodynamic behavior of a cambered, two-element, high-lift wing in ground effect. Qu et al. [8] numerically studied the effect of wide range of AOA on aerodynamic forces on an airfoil in ground effect. Yang et al. [9] conducted a numerical investigation of the effect of viscosity and compressibility on the aerodynamics of a 2D NACA0012 wing in ground effect. Doig et al. [10] numerically studied the transonic RAE2822 airfoil and the effect of lower surface shock on the aerodynamic forces. In his paper, several simulations involving shock buffet were found but not analyzed in great detail.

1.1.1 2D Ground Effect

For an airfoil of long span, the 2D chord-dominated ground effect has been extensively investigated. The physics behind the increase in lift in ground effect is that the airflow blocking effect from the convergent passage between the lower surface and the ground causes the pressure on the lower surface to increase; the upper surface pressure also increases because of the streamlines' upward deflection. When the airflow blocking effect is greater than the streamlines' deflection, an increase in lift is observed.

1.2 Transonic Flight

When the velocity of the airflow exceeds the local speed of sound, a shock wave appears. The freestream Mach number at which a shockwave first appears on an airfoil is called the critical Mach number. The critical Mach number not only depends on the aircraft speed, but also on the local environment like temperature since the local speed of sound equals $\sqrt{\gamma RT}$. Modern commercial jet engine powered aircraft are designed to operate at transonic speeds to achieve higher operating efficiency. Typically, the airflow over the upper surface of the airfoil gains larger speed compared to freestream velocity, therefore a shock wave appears on the upper surface of the airfoil for freestream Mach number greater than the critical Mach number.

1.2.1 Sound Barrier

For subsonic flight, the linearized compressibility correction of Prandtl-Glauert gives $C_p = \frac{C_{p,0}}{\sqrt{1-M_\infty^2}}$, while for supersonic flight, the linearized supersonic theory gives $C_p = \frac{C_{p,0}}{\sqrt{M_\infty^2-1}}$. However, these relationships are obtained from linearized perturbation velocity potential equation which does not hold for transonic flight. From the experiments, C_D becomes very large for freestream Mach

number close to critical Mach number, $M > M_c$. This is the concept of sound barrier. The value of freestream Mach number at which the drag has sudden increase is defined as the drag-divergence Mach number. The existence of sound barrier requires more powerful jet engines and better designed wings for transonic flight.

1.2.2 Supercritical Airfoils

The design of supercritical airfoils from 1945 to 1965 was focused on achieving higher critical Mach number. Researchers found that thinner the airfoil, higher is the critical Mach number; thus the aircraft could operate at a higher speed without the appearance of a shock. The limitation of the thin airfoil design is that the structural integrity and functionality of the airfoil can be greatly impaired. The alternative approach is to delay the drag-divergence Mach number by designing a relatively flat top airfoil with high camber and large radius at the leading edge; the supersonic region above the airfoil will have lower local values of Mach number thereby reducing the shock strength and creating less drag.

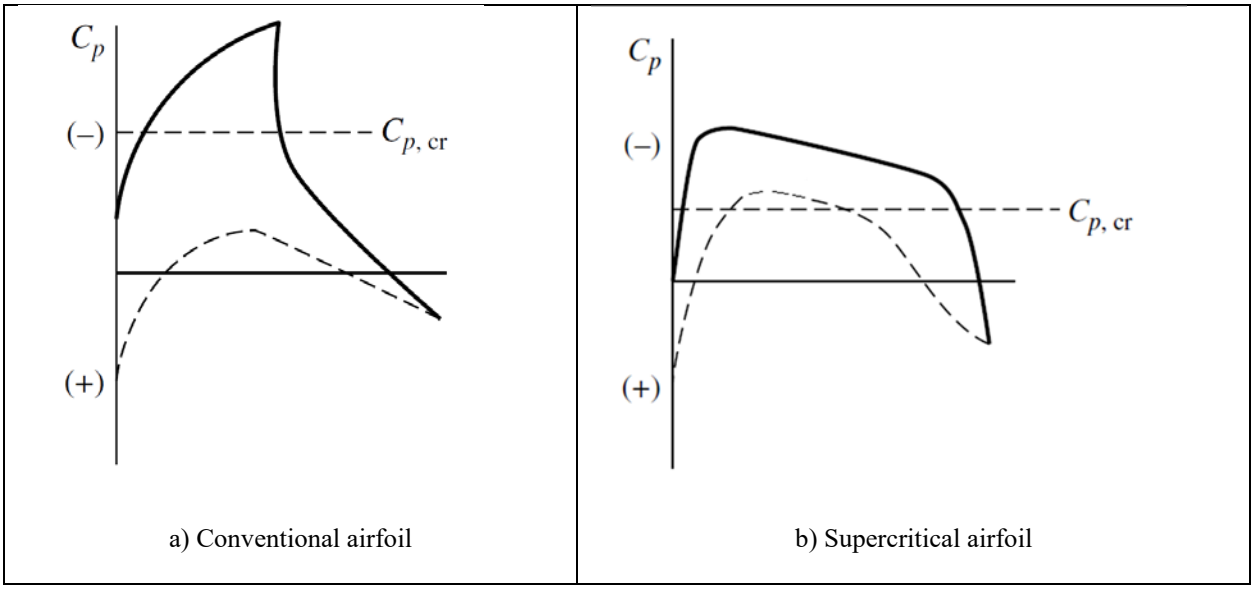

a) Conventional airfoil

b) Supercritical airfoil

Figure 1.1 Pressure coefficient distribution for different airfoils at transonic speed

1.3 Shock Buffet

When transonic flow conditions, especially at moderate to high Mach number, the relatively weak shock interacts with a boundary layer inducing a small region of separation. This my result in a self-sustained shock buffet causing the flow field to oscillate. This can be highly problematic if the shock buffet frequency is in the same range as the vibration frequency of the structure creating resonance, causing the structure to undergo limit cycle oscillations leading its possible failure. Many experiments and numerical simulations have been conducted to understand the physical mechanism behind the buffet phenomenon in fifty years. [11-21]

1.3.1 Shock Buffet on a Biconvex Airfoil

For symmetric biconvex airfoil at zero angle of attack, due to symmetry, the shock oscillates on the upper and lower surface of the airfoil in anti-phase. There are three possible types of shock movements: type A wherein two shocks have nearly sinusoidal motion and the shocks never disappear; type B of two shocks having different dynamic effects with one shock becoming very weak and degenerating into a weak pressure wave seen in photographic studies; and type C of two shocks having only the upstream periodic motion and alternating between the upper and lower surface [11].

1.3.2 Shock Buffet on a Supercritical Airfoil

The buffet of supercritical airfoils has been relatively less studied. The experiments by Lee et al. [20-22] provide extensive set of data. The shock buffet phenomenon on a supercritical airfoil has been explained by B.H.K. Lee [22] by combining the downstream propagation of disturbances and the upstream propagation of waves in the separated flow regions. Q. Xiao et al. [23] performed a numerical study on a BGK No.1 supercritical airfoil; their results confirm that the pressure waves behind the shock through the separated region interact with the upstream-moving waves outside

the separated region. The oscillation period also agrees well with the buffet model proposed by B.H.K Lee [22].

1.4 Commercial CFD Flow Solver ANSYS

The simulation software used in this study is ANSYS, which is a widely used commercial simulation software in industry. For flow simulations, ANSYS Fluent includes RANS and LES turbulence models and a wide variety of discretization schemes in space and time. The version 17.1 of ANSYS Fluent is employed in this study.

1.4.1 Mesh Generation

The software used to generate the computational domain and the mesh is ANSYS ICEM CFD. It contains geometry acquisition, mesh generation, and mesh diagnostic and repair tools. The general meshing work flow is shown in Figure 1.2.

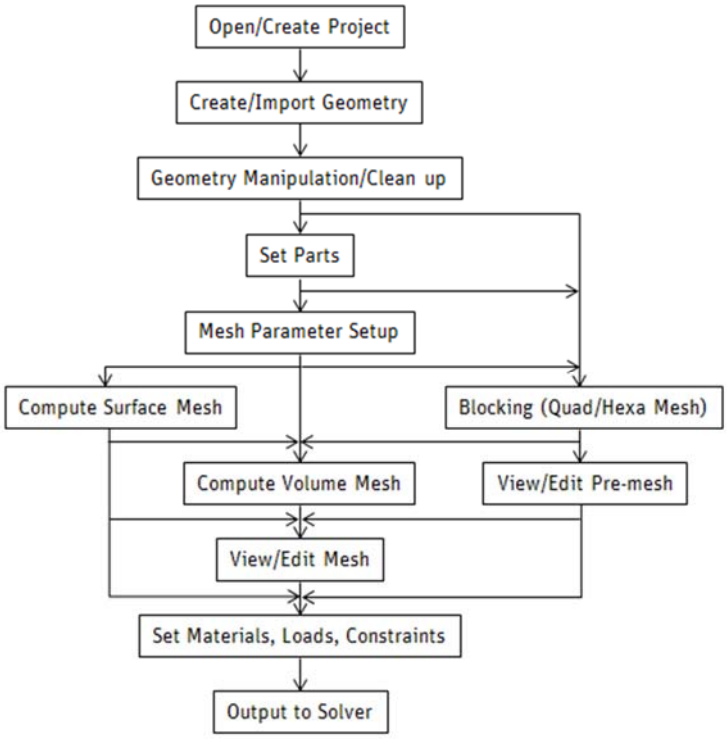

Figure 1.2 ICEM CFD Workflow

1.4.2 Simulation Software and Numerical Methods

The software used for running all the numerical simulations in this thesis is ANSYS Fluent. It is written in C language and supports the dynamic memory allocation, efficient data structures, and flexible solver control. The workflow in Fluent is as follows: read mesh into ANSYS Fluent, set the boundary conditions, define the fluid properties, execute the solution, and perform the post-processing. All simulations run in parallel mode, which means that the ANSYS Fluent splits the mesh and data into multiple partitions, then assigns each mesh partition to a different computing node. The scalability is excellent with the current computer configuration.

ANSYS Fluent solver is based on the finite volume method where the domain is discretized into a finite set of control volumes. The governing equations of conservation of mass, momentum and energy are solved on the set of control volumes. Using the finite volume method, the conservation laws are naturally satisfied, thus the discontinuities in the solution such as shocks etc. are better resolved than in the finite difference based solver. The pressure-based solver is chosen to address the problem of pressure-velocity coupling. The coupled algorithm solves the momentum and continuity equations together in a fully implicit manner by adding a pressure gradient term in the momentum equations.

To solve the large implicit matrix, the coupled AMG solver is used to accelerate the iteration process. The incomplete lower upper (ILU) AMG smoother is chosen over Gauss-Seidel method for its high efficiency.

Chapter 2: Numerical Method and Validation

2.1 Physical Model

A typical supercritical RAE2822 airfoil is employed in this study. The chord length is 1.0m, and the maximum thickness to chord ratio is 12.1%. Angles of attack from 0 to 12 degrees are considered to study both the steady and unsteady transonic flow in ground effect. The ground clearance with h/c = ∞, 1.0, 0.8, 0.6, 0.4, 0.2, and 0.1 are considered.

2.1.1 Mesh Topology and Mesh-Generation

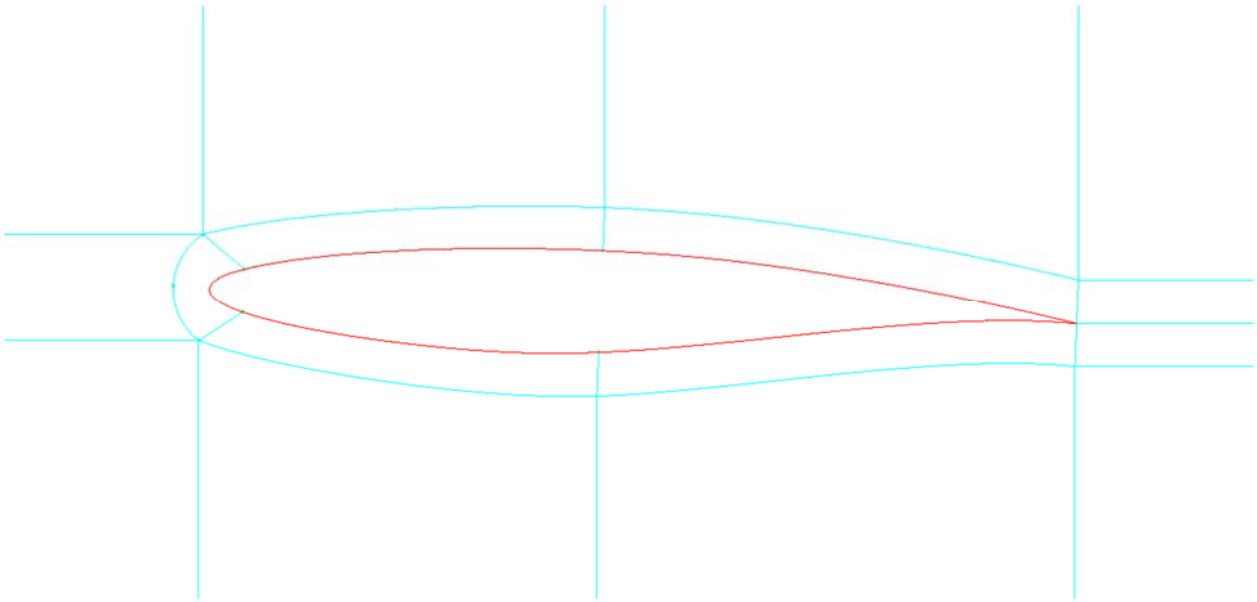

Figure 2.1 Mesh topology for CFD simulation

Due to the ease of converting airfoil mesh in unbounded flow to that in ground effect, an H-mesh topology is used in all simulations. The blocks at the trailing edge are collapsed to obtain a sharp trailing edge. The orthogonality of the mesh is crucial in CFD simulations since poor mesh quality usually causes errors in the simulations. The O-grid around the airfoil is generated to create layers

of orthogonal meshes surrounding the airfoil. The topology of the mesh remains unchanged in all simulations.

The airfoil is split into two parts, the upper surface and the lower surface, to facilitate the analysis of lift and drag on different surfaces.

2.2 Numerical Method

A rectangular computational domain is employed as shown in Fig. 2.2. A structured mesh with refinement in the wake region and between the airfoil and the ground is also shown in Fig. 2.2. The inlet and the top boundaries are located 60c away from the airfoil, the outlet boundary is 80c away, and the bottom boundary is 60c away from the airfoil in the unbounded flow case. For the inlet, outlet, top and bottom boundaries, pressure far-field boundary condition is employed, which specifies the two Riemann invariants for a flow normal to the boundary. For the ground, a no-slip moving wall boundary condition with the translational velocity equal to the freestream velocity is employed.

The equations for the unsteady compressible turbulent flow can be written as:

Mass conservation:

$$\frac{\partial \rho}{\partial t} + \frac{\partial}{\partial x_j}\left(\rho u_j\right) = 0 \tag{1}$$

Momentum conservation:

$$\frac{\partial}{\partial t}\left(\rho u_i\right) + \frac{\partial}{\partial x_j}\left(\rho u_j u_i\right) = -\frac{\partial p}{\partial x_i} + \frac{\partial \hat{\tau}_{ji}}{\partial x_j} \tag{2}$$

Total energy conservation:

$$\frac{\partial}{\partial t}\left(\rho E\right) + \frac{\partial}{\partial x_j}\left(\rho u_j H\right) = \frac{\partial}{\partial x_j}\left[u_i \hat{\tau}_{ji} + \left(\mu + \sigma^* \mu_T\right)\frac{\partial k}{\partial x_j} - q_j\right] \tag{3}$$

The turbulence model used in this thesis is the Spalart-Allmaras turbulence model, μ_t in equation (4) is calculated based on the SA turbulence model.

$$\hat{\tau}_{ji} = (\mu + \mu_t)S_{ij}, \quad where\ S_{ij} = \frac{1}{2}\left(\frac{\partial u_i}{\partial X_j} + \frac{\partial u_j}{\partial X_i}\right) \tag{4}$$

The double precision solver in ANSYS FLUENT 17.1 is used to perform the CFD simulations. Compressible Reynolds-averaged Navier-Stokes equations with Spalart-Allmaras turbulence model are solved. Second-order numerical scheme is used for both the convection and diffusion terms. The pressure-coupled transient solver is used for pressure-velocity coupling. In all simulations, a few displayed an unsteady behavior; without knowing in advance whether the flow is steady or unsteady in a particular simulation, transient solver is employed in the simulations. In case of steady flow, convergence is considered achieved when C_L and C_D changed within 0.01% over 1000 iterations. In case of unsteady flow, the time step used is equal or less than T/200, where T denotes the time period of the unsteady converged solution. The transient solution is considered converged when the aerodynamic coefficients became periodic after several cycles and do not change from one cycle to next.

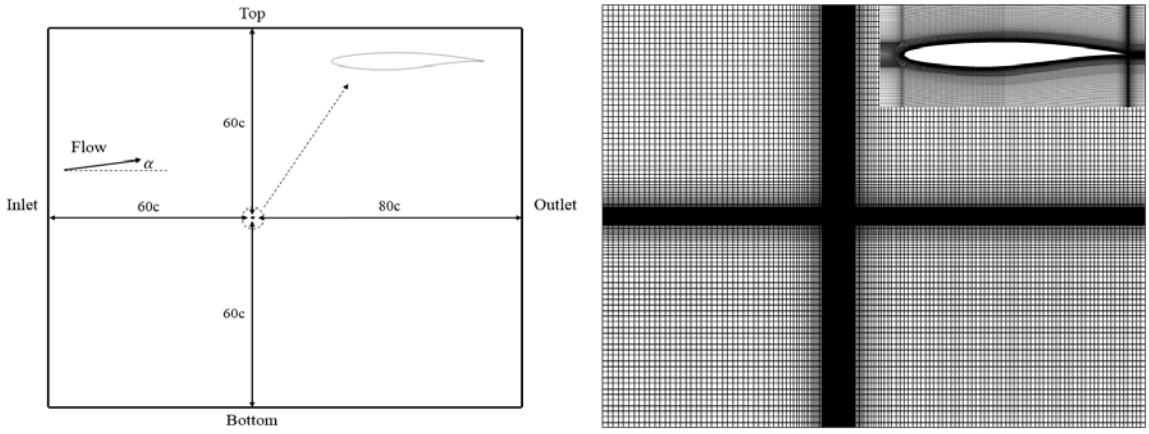

Figure 2.2 (a) Computational domain and mesh layout in unbounded flow.

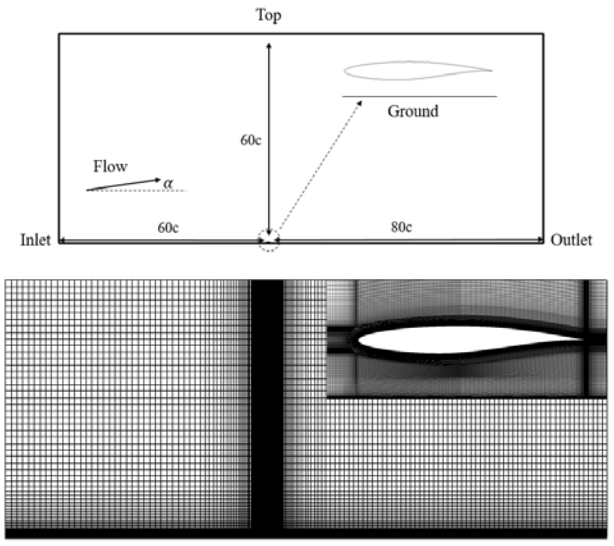

Figure 2.2 (b) Computational domain and mesh layout in ground effect.

Figure 2.2 Computational domain and mesh layout.

2.3 Validation of Numerical Method

2.3.1 Steady State Validation

The mesh independence of the computed solution is ascertained by comparing the present numerical results with those of NASA's benchmark numerical solutions for RAE2822 airfoil in unbounded flow at Mach number 0.729. Coarse, medium and fine meshes are tested in the mesh independence study. The coarse mesh has 315 nodes on the airfoil and a total of 97,775 cells. The medium mesh has 695 nodes on the airfoil with a total of 269,520 cells. The fine mesh has 855 nodes on the airfoil with a total of 527,468 cells.

The dimensionless wall distance (y+) from the surface is estimated using the flat plate analysis. All meshes are graded so that y+ is less than 0.1 for the first mesh point away from the wall. This gives sufficient mesh resolution in near-wall regions to use the law of the wall in viscous sublayer. The results are summarized in Table 2.1 indicating that the medium mesh gives acceptable accuracy for both lift and drag predictions; therefore, the medium mesh is used in all the simulations presented in this thesis.

Table 2.1 Mesh independence study for RAE2822 airfoil in unbounded flow; M = 0.729, α = 2.31 deg.

Mesh	**Cell numbers**	**y+**	**C_L**	**C_D**
Experiment			0.743318	0.012700
NASA-CFD			0.730962	0.012117
Coarse mesh	97775	<0.1	0.719598	0.012679
Medium mesh	269520	<0.1	0.721315	0.012699
Fine mesh	527468	<0.1	0.721788	0.012638

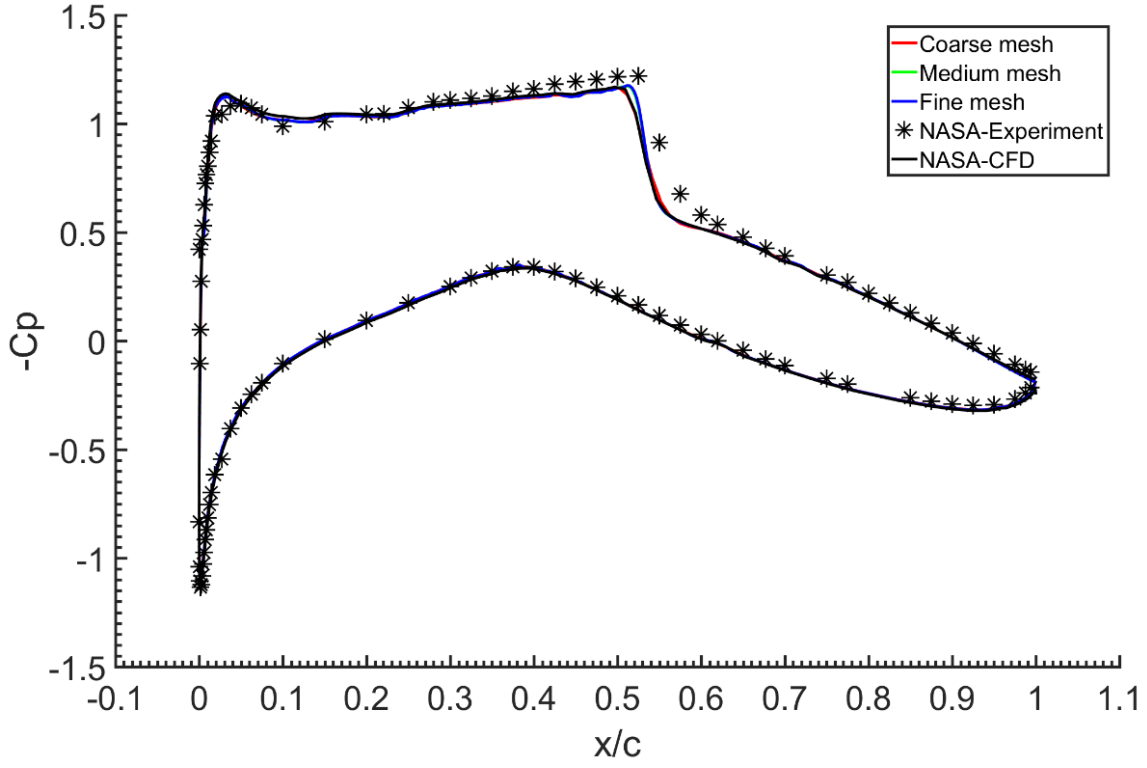

Figure 2.3 Computed C_p comparison with experimental result using coarse, medium and fine mesh.

From Figure 2.3, all CFD results predict the shock location slightly earlier than the experiment. The CFD results agree well with the experimental data; the coarse mesh predicts the shock location slightly forward, but the medium and fine meshes are able to capture the shock location quite well. The pressure contours and sonic line in Figure 2.4 show the pressure of a shock behind the middle of the upper surface of the airfoil. The sonic line where the local Mach number equals unity is marked in red in Figure 2.4. There is no shock on the lower surface.

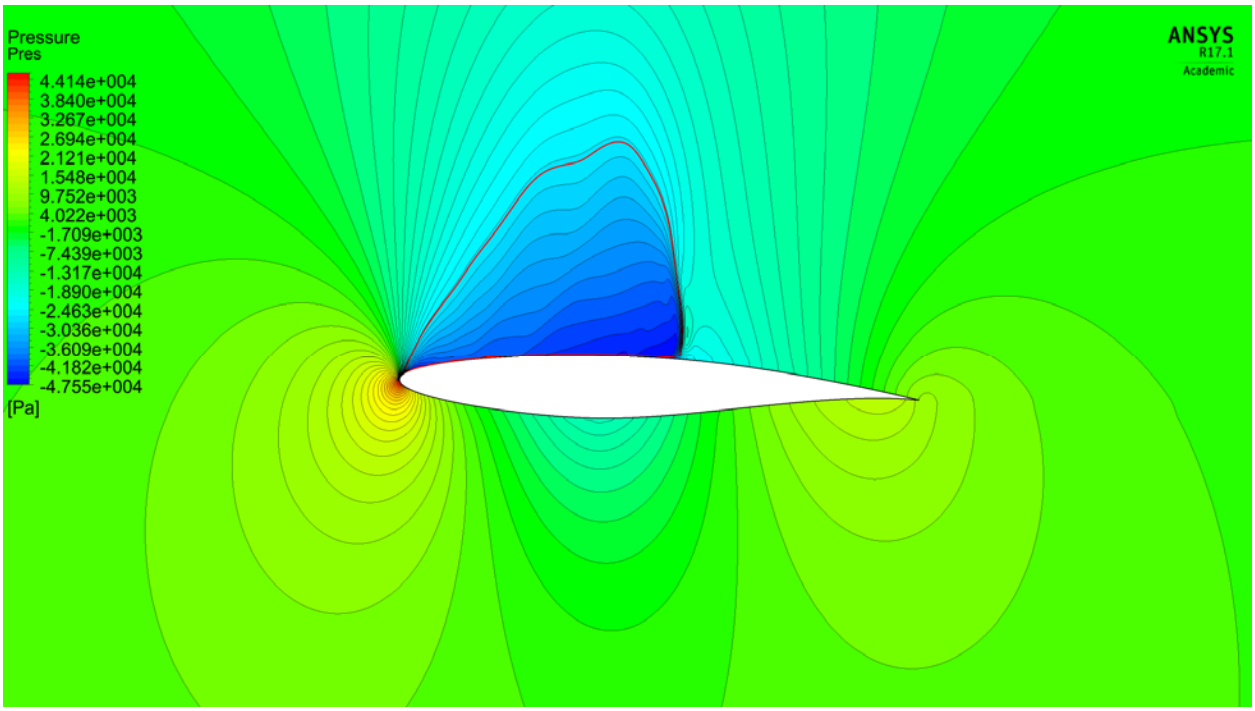

Figure 2.4 Pressure contours and sonic line of an RAE2822 airfoil at M = 0.729 and α = 2.31 deg.

Table 2.2 Comparison of aerodynamic forces on adapted mesh

Mesh	**Cell numbers**	**C_L**	**C_D**
Standard mesh	269520	0.721315	0.012699
Standard mesh with first adaptation	279790	0.721765	0.012615
Standard mesh with second adaptation	293772	0.721925	0.012626

Physically a shock is a discontinuity in pressure, density and temperature in the flow field. It requires sufficient mesh density near the shock to reduce the discretization error. It would be very costly to increase the mesh density in the entire flow field. It is also not always possible to make a wild guess as to where in the flow domain that higher mesh resolution is needed without knowing the position of the shock. Adaptation of the mesh with pressure gradient as a sensor is one of the best feasible ways to refine the mesh.

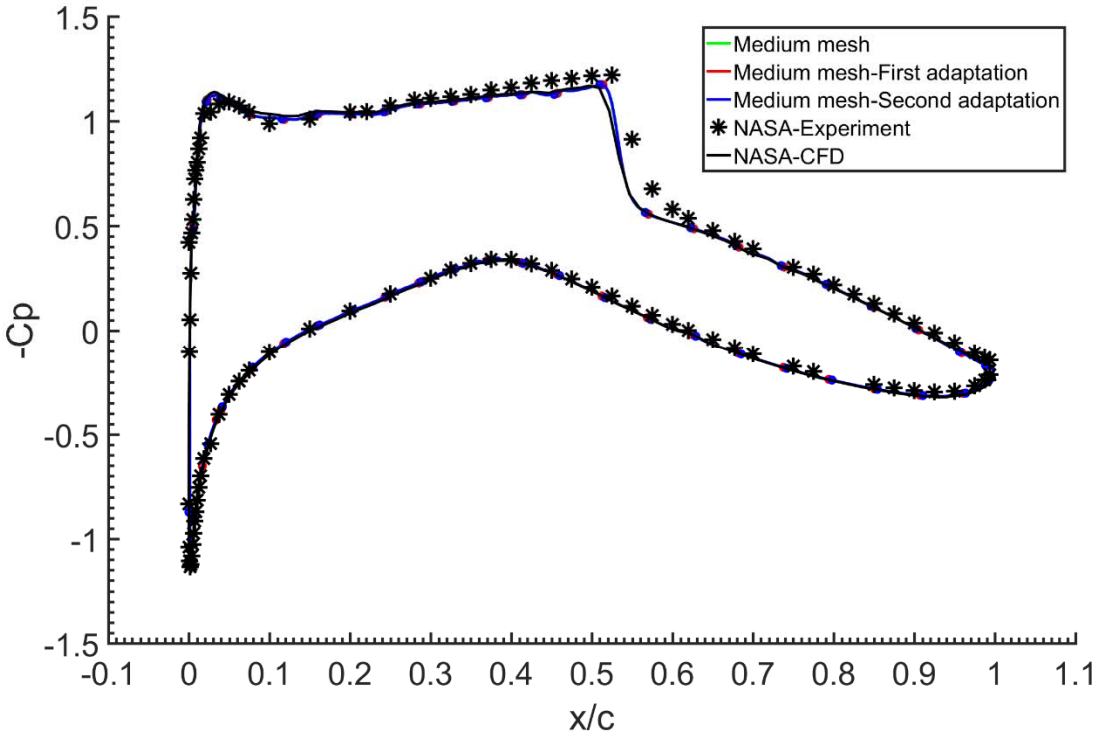

Figure 2.5 Comparison of the computed C_p on standard mesh and adapted mesh with the experimental data.

The first adaptation of mesh predicts the shock location ahead of the experimental location, while the second mesh adaptation also does not show noticeable change in the shock location as shown in Figure 2.5. However, the smearing in pressure contours is much reduced, with only a few thousand additional cells as shown in Figure 2.6. This implies that the gradient based mesh adaptation method is very useful in computing flows with high gradients such as shocks or stagnation points. However, due to insignificant differences in aerodynamic forces between medium mesh and refined mesh results, and the fact that the shock is unsteady at certain Mach numbers, angles of attack, and ground clearances, the adaptation is not used in the thesis study.

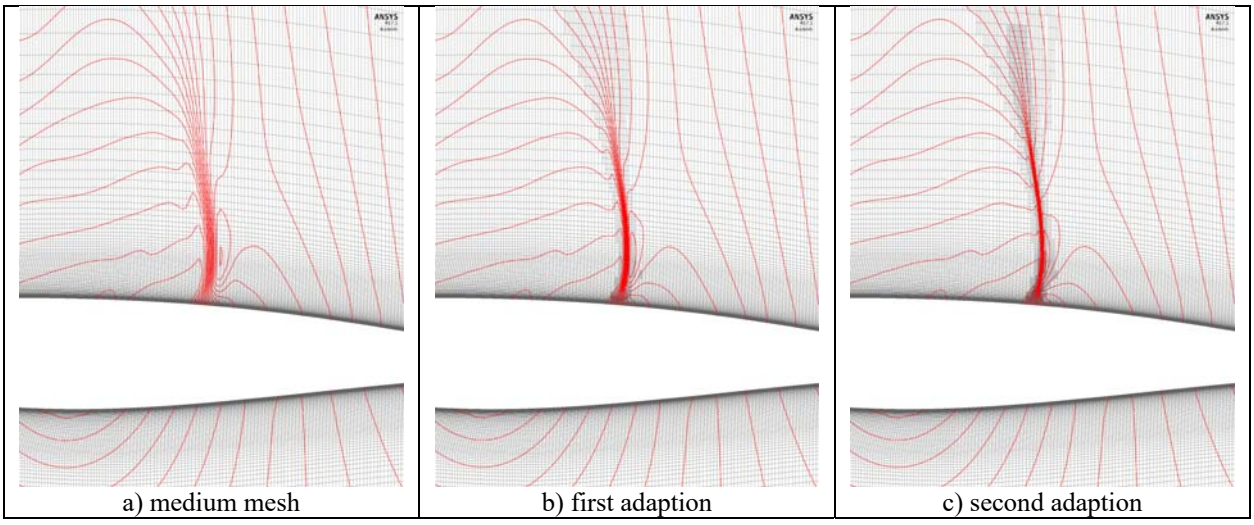

a) medium mesh b) first adaption c) second adaption

Figure 2.6 Resolution of Pressure contours near the shock with increasingly-refined mesh.

2.3.2 Unsteady Shock Buffet Validation

The basic numerical method used to solve the unsteady compressible turbulent flow is the same as described earlier. It is applied to the BGK No.1 supercritical airfoil [19-23]. For this validation test case, the flow field computed for a BGK No.1 supercritical airfoil at Mach number 0.71 at an angle of attack α = 6.97 deg. The flow is unsteady with shock-induced oscillations. The simulation is initialized from a uniform initial condition. The time step used is 0.00025s; the nondimensionalized time step (tU_∞/c) is 0.0604. The solution is monitored by the lift and drag coefficient of the airfoil. The simulation is considered converged when the solutions become periodic.

Different initial conditions for the simulations are used to observe the influence of initial conditions. Three different initial conditions employing the uniform, hybrid and full-multi-grid method are compared. In the flow field of hybrid initialization, Laplace equations for velocity and pressure are solved in the entire flow field, and the other flow variables are patched using the domain averaged value. In the full-multi-grid initialization, the flow domain is computed at different grid levels, and the FMG initialization solves the Euler equations for inviscid flow using

first order-discretization. The results from these different initialization methods are compared in the time for simulations to reach a converged solution. As shown in Figure 2.7, the uniform initialization and the hybrid initialization show very close agreement for the solution to reach periodicity, while the full multi-grid initialization method is able to converge faster than the other two methods. Once the periodic state is reached, the solutions are found to be identical, providing evidence that the final periodic unsteady is insensitive to the initial condition.

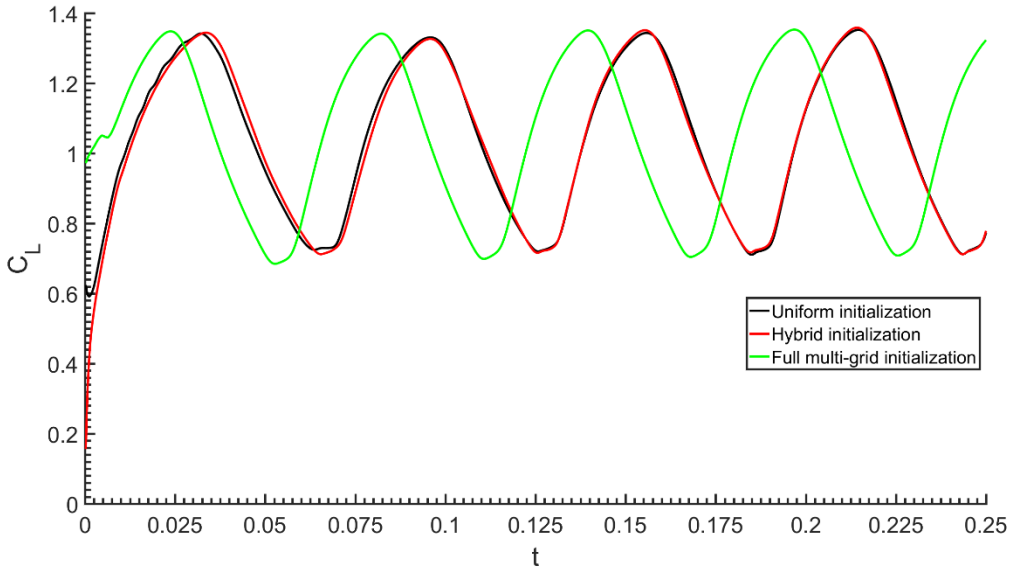

Figure 2.7 Convergence history of different flow field initialization methods.

The lift coefficient history is presented in Figure 2.8. Fourier analysis of the lift coefficient shown in Figure 2.9 reveals a reduced frequency of 0.222, which is about 11.2% lower than that in the experiment of Lee el al. [20] ($k = \pi f c/U_\infty = 0.25$). The average lift coefficient is 1.061, which is 4.5% larger than the experimental value. The pressure on the airfoil is time-averaged; the pressure distribution on the upper surface of the airfoil is presented in Figure 2.10. The pressure coefficient on the front portion of the upper surface of the airfoil is larger than that in the experiment, while the pressure coefficient of the middle to trailing edge portion of the airfoil agrees well with the experimental data.

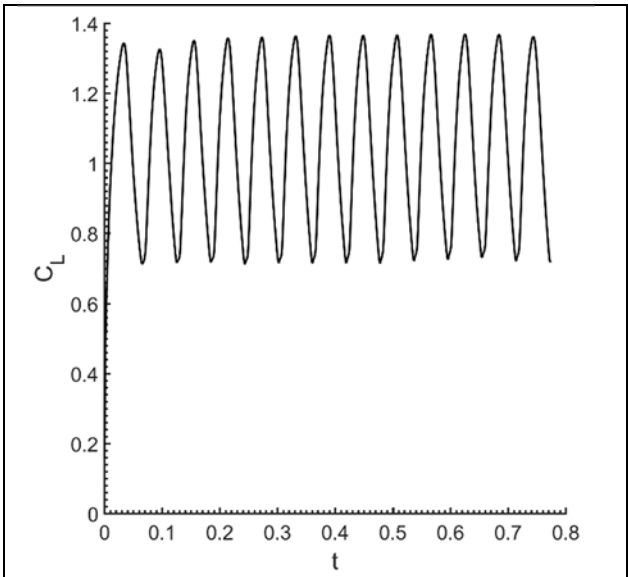

Figure 2.8 C_L history for M = 0.71 and α = 6.97 deg.

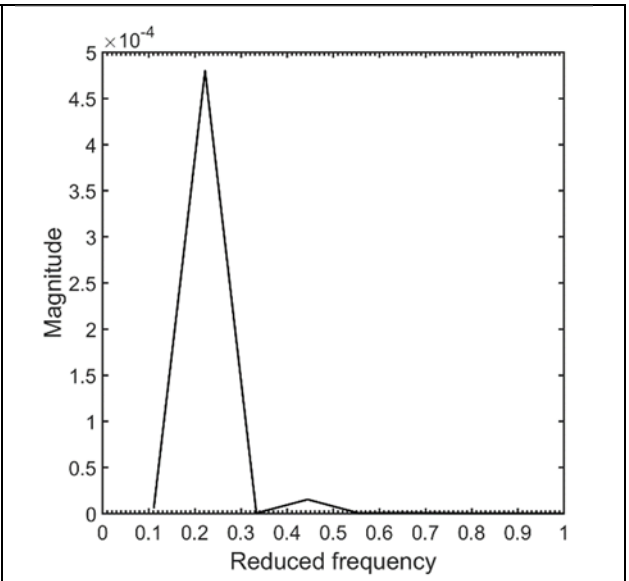

Figure 2.9 Fourier analysis of reduced frequency.

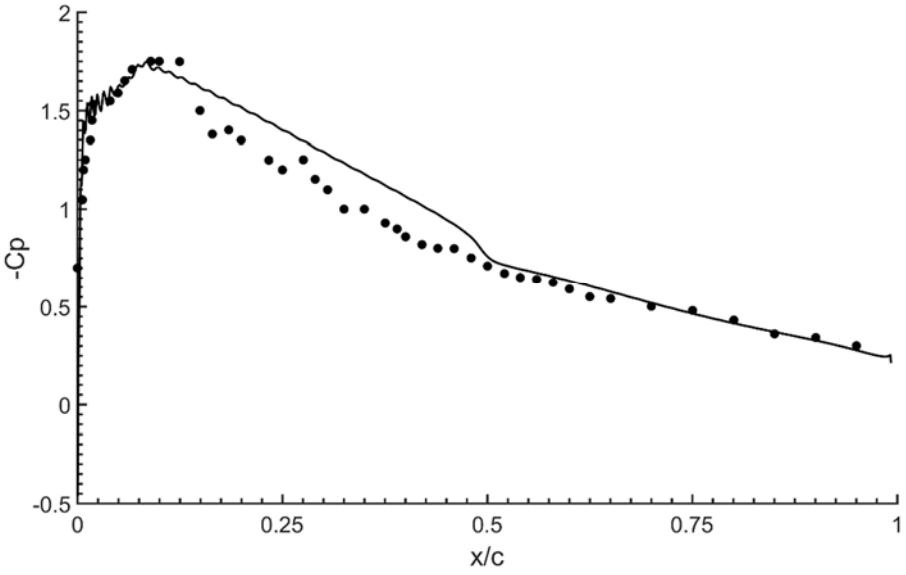

Figure 2.10 Time-averaged pressure distribution on the upper surface of the airfoil.

This validation shows that the mesh quality as well as the numerical method are sufficient to predict the shock buffet phenomenon; the pressure coefficient and the aerodynamic coefficients are within agreeable range compared to the experimental data. The error in the prediction of reduced frequency is much less compared to the numerical simulations of Xiao et al. [23].

Chapter 3: Results and Discussion

3.1 Lift and Drag for Various M, α and h/c

For lift and drag coefficient, the universal definitions and notations are used. The lift and drag coefficients are defined as follows. The total lift coefficient is defined as:

$$C_L = \frac{1}{0.5\rho V_\infty^2 c} \oint_{S_{up}+S_{low}} \left((p - p_\infty)\boldsymbol{n} + \boldsymbol{\tau}\right) \cdot \boldsymbol{j} \mathrm{dS} \tag{5}$$

For the upper and lower surface, the lift coefficients are defined as follows:

$$C_{L,up} = \frac{1}{0.5\rho V_\infty^2 c} \oint_{S_{up}} \left((p - p_\infty)\boldsymbol{n} + \boldsymbol{\tau}\right) \cdot \boldsymbol{j} \mathrm{dS} \tag{6}$$

$$C_{L,low} = \frac{1}{0.5\rho V_\infty^2 c} \oint_{S_{low}} \left((p - p_\infty)\boldsymbol{n} + \boldsymbol{\tau}\right) \cdot \boldsymbol{j} \mathrm{dS} \tag{7}$$

The total drag coefficient is defined as follows:

$$C_D = \frac{1}{0.5\rho V_\infty^2 c} \oint_{S_{up}+S_{low}} \left((p - p_\infty)\boldsymbol{n} + \boldsymbol{\tau}\right) \cdot \boldsymbol{i} \mathrm{dS} \tag{8}$$

For the upper and lower surface, the drag coefficients are defined as follows:

$$C_{D,up} = \frac{1}{0.5\rho V_\infty^2 c} \oint_{S_{up}} \left((p - p_\infty)\boldsymbol{n} + \boldsymbol{\tau}\right) \cdot \boldsymbol{i} \mathrm{dS} \tag{9}$$

$$C_{D,low} = \frac{1}{0.5\rho V_\infty^2 c} \oint_{S_{low}} \left((p - p_\infty)\boldsymbol{n} + \boldsymbol{\tau}\right) \cdot \boldsymbol{i} \mathrm{dS} \tag{10}$$

The total lift and drag coefficient at various angles of attack and Mach numbers for different ground clearances are shown in Figures 3.1 – 3.6.

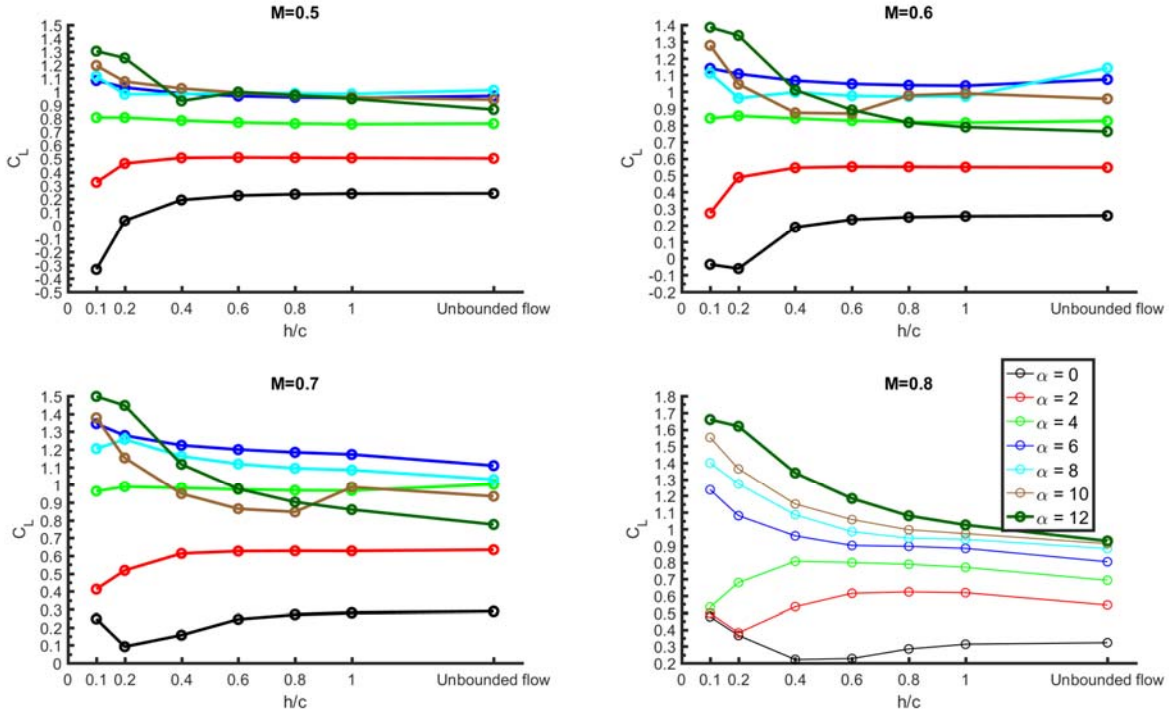

Figure 3.1 Variation of C_L with ground clearance for various α and M.

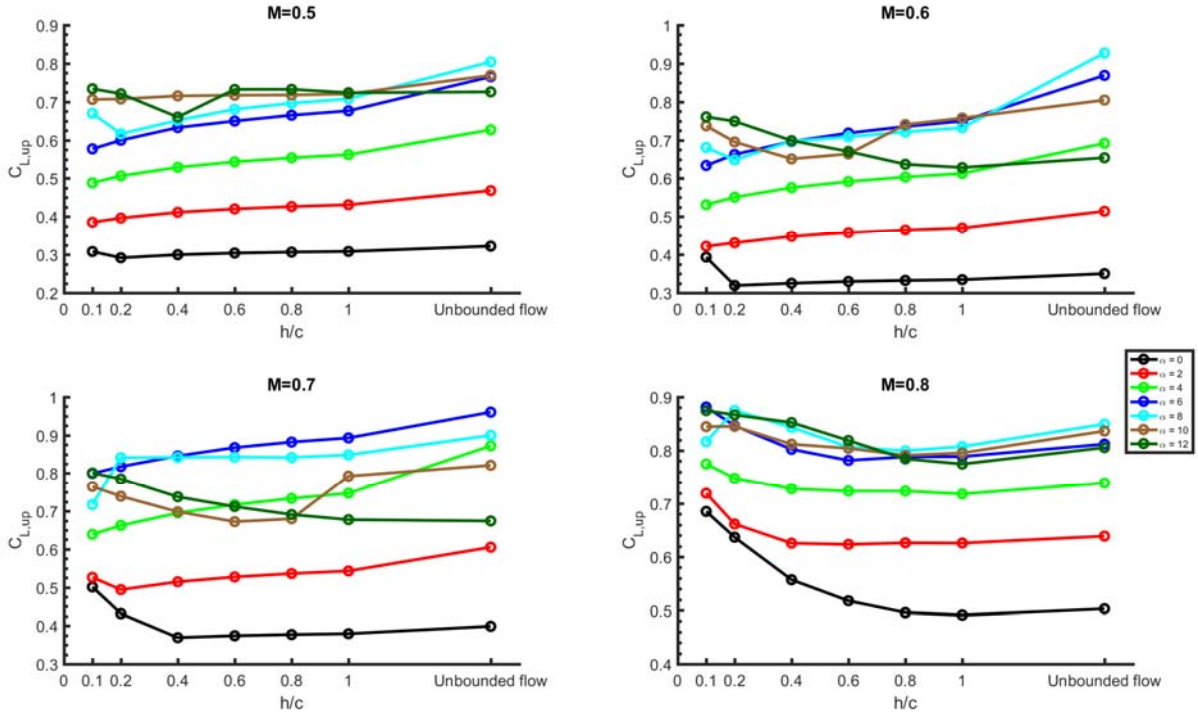

Figure 3.2 Variation of $C_{L,up}$ with ground clearance for various α and M.

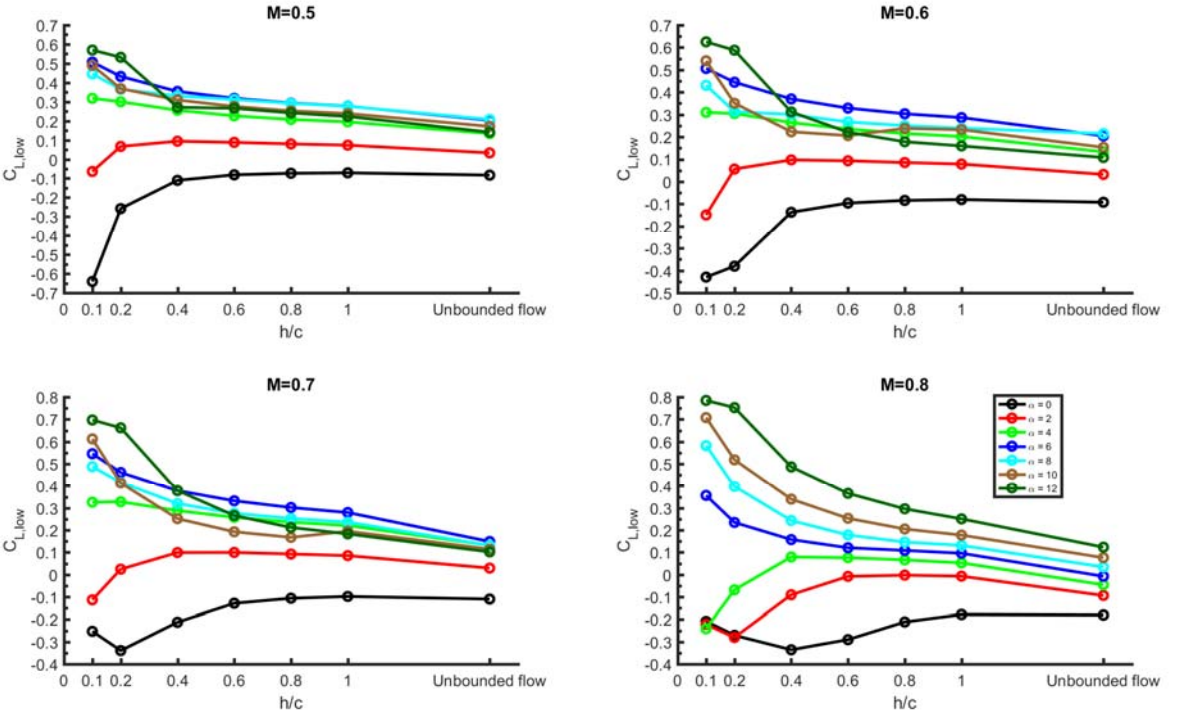

Figure 3.3 Variation of $C_{L,low}$ with ground clearance for various α and M.

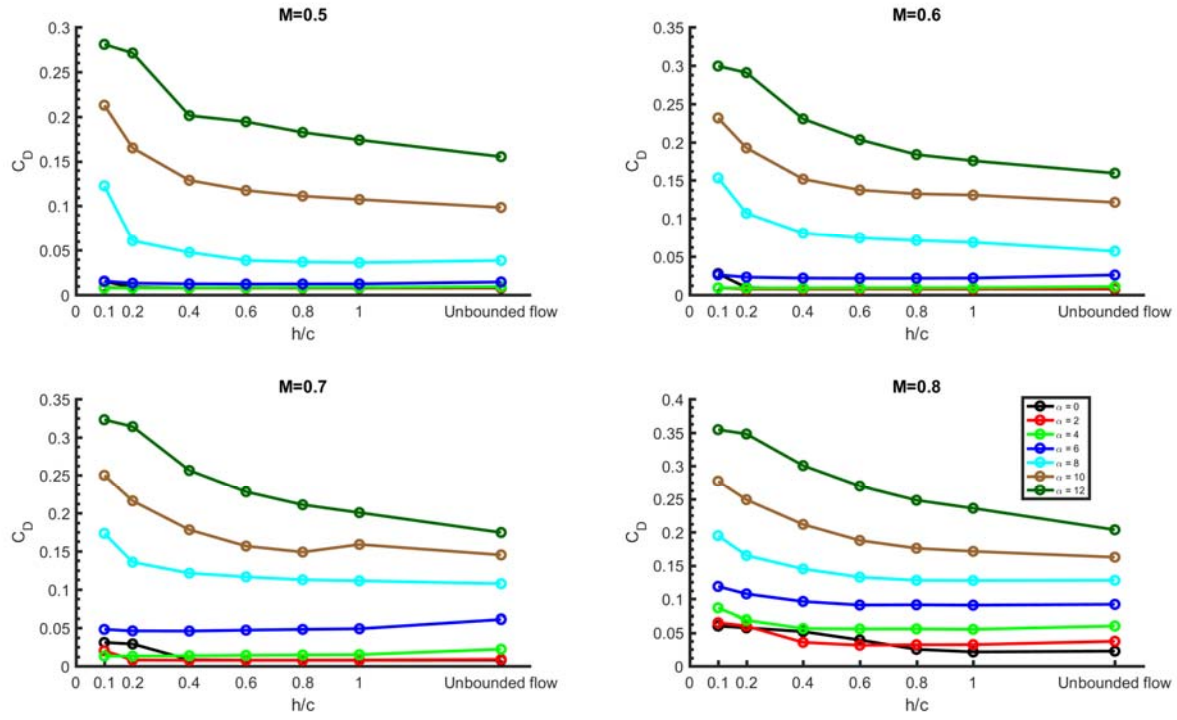

Figure 3.4 Variation of C_D with ground clearance for various α and M.

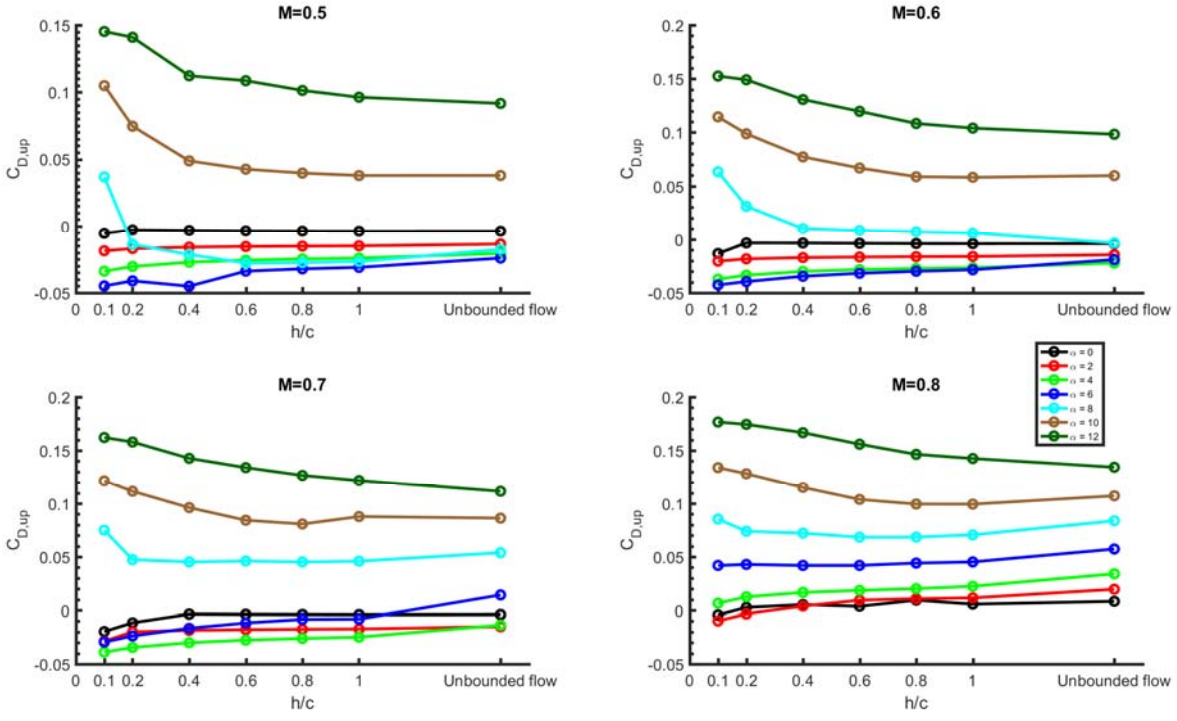

Figure 3.5 Variation of $C_{D,up}$ with ground clearance for various α and M.

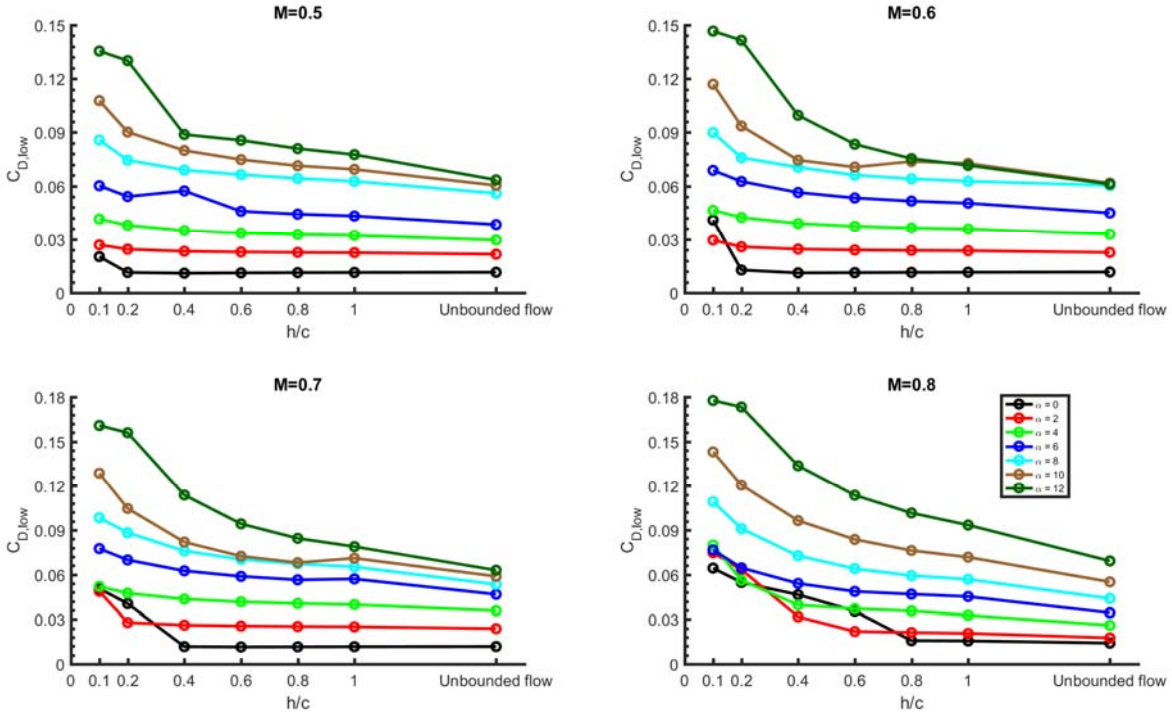

Figure 3.6 Variation of $C_{D,low}$ with ground clearance for various α and M.

The lift coefficient curves in Figure 3.1 shows that the most dramatic change in aerodynamic coefficients occurs at $\alpha = 0$ deg with decrease in ground clearance. At M = 0.6, with decrease in ground clearance, the lift coefficient at $\alpha = 0$ deg changes sign between h/c = 0.2 to 0.4. Instead of producing lift, the airfoil generates downforce in this particular situation. The lift coefficient at $\alpha = 2$ deg is smoother with decrease in ground clearance until h/c < 0.2. Increasing the angle of attack can delay the dramatic change in lift coefficient at high Mach number.

The drag coefficient curves in Figure 3.3 show that at $\alpha < 4$ deg, the drag is very small compared to that at high angles of attack and higher Mach numbers due to unseparated flow and the absence of shock. Increase in the angle of attack causes the flow to separate at the upper surface of the airfoil and causes the drag coefficient to increase dramatically. Increase in the Mach number results in the appearance of a shock, and the wave drag generated by the shock contributes to increase in the drag.

Considering the variation in total lift with ground clearance, the ground effect of a transonic airfoil can be divided into two regions. When the ground clearance decreases from unbounded flow to a value between 0.2 < h/c < 1, the upper surface shock appears; further decreasing the ground clearance causes the lower surface shock to form causing huge loss in lift and increase in drag.

At higher angles of attack from $\alpha = 6$ deg to $\alpha = 12$ deg, there could also be unsteady behavior in the flow field. At lower Mach number, this is due to the periodic separation of the flow on the upper surface of the airfoil. At higher Mach number when there is upper surface shock, the periodic separation is coupled with the movement of the position of the shock. Both the periodic separation and the shock buffet phenomenon are undesirable since they strongly affect the maneuverability and structural integrity of the airplane.

3.1.1 High Ground Clearance

For RAE2822 airfoil in ground effect, at a given freestream Mach number, as the ground clearance decreases, a shock first appears on the upper surface. If the ground clearance decreases further, a shock forms between the lower surface of the airfoil and the ground. In this thesis, the high ground clearance is defined as the height when there is no shock between the lower surface of the airfoil and the ground. Thus, for a different freestream Mach number, there is a different value for high ground clearance. Here we analyze a typical case of M = 0.7 and $\alpha = 4$ deg. Figure 3.7 shows the pressure coefficient distribution on the airfoil at different values of ground clearance. From Figure 3.7, it can be seen that as the ground clearance decreases, the shock moves towards the leading edge causing the pressure to increase on the upper surface, therefore $C_{L,up}$ gradually decreases. Figure 3.8(a) presents variations in lift coefficients with the ground clearance from h/c = ∞ to 0.1. For the lift coefficient in unbounded flow, $C_{L,up}$ is much larger than $C_{L,low}$ which is also the case in subsonic ground effect [8]; this is due to the presence of a low pressure zone prior to the

appearance of upper surface shock thereby decreasing the lift generated by the upper surface. Doig [10] pointed out that the stagnation point moves downward as the ground clearance decreases and as the stagnation point moves downward, a high pressure zone forms near the middle section of the lower surface causing $C_{L,low}$ to gradually increase to compensate for the lift loss. Interestingly, the end result is that the total lift coefficient changes very little.

The drag coefficient in this case also shows a similar behavior. However, the change in drag is much more dramatic than in the lift. The overall C_D decreases by 32% for h/c = 1.0 and by 40% for the lowest ground clearance of h/c = 0.1. Figure 3.8(b) shows that $C_{D,up}$ decreases and $C_{D,low}$ increases as the ground clearance decreases. The drag reduction on the upper surface is due to the reduced shock strength resulting in reduced the and strength of the shock induced separation. The high pressure zone near the leading edge of the lower surface combined with the airfoil curvature causes $C_{D,low}$ to increase.

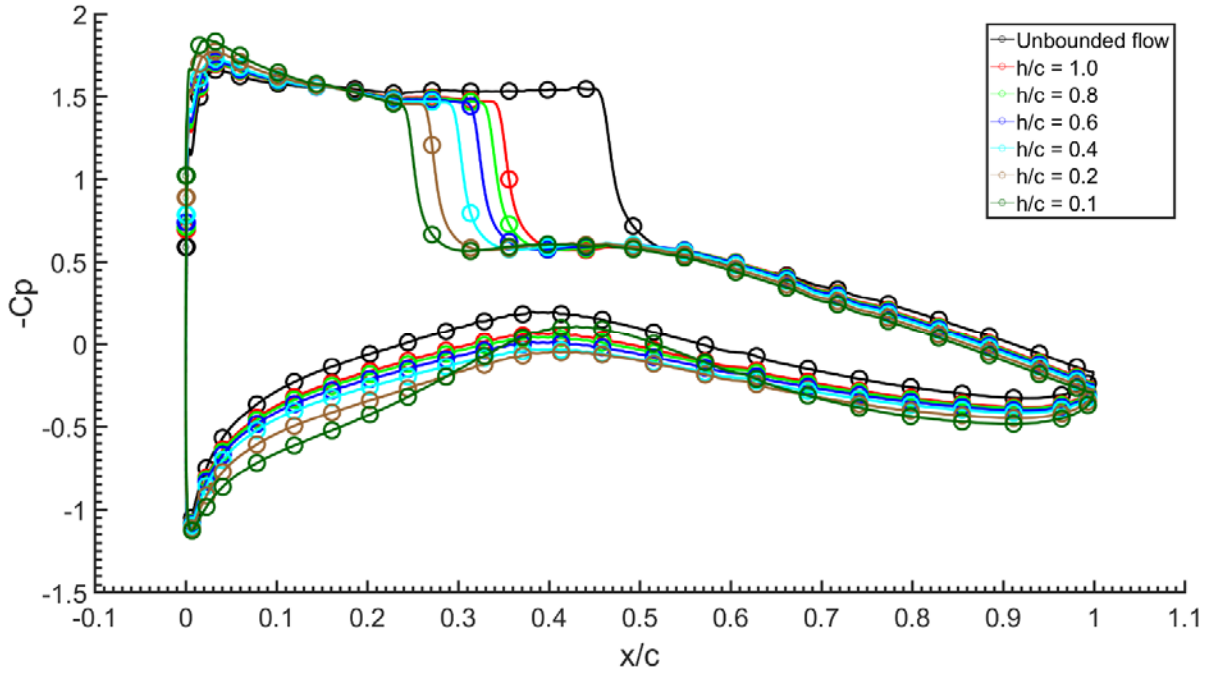

Figure 3.7 Pressure coefficient distribution on the RAE2822 airfoil for various ground clearances at M = 0.7 and α = 4 deg.

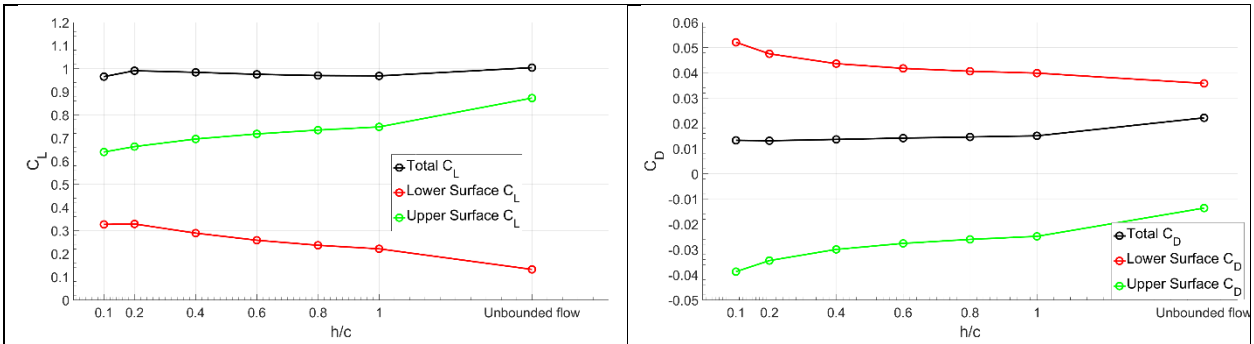

a) C_L with various ground clearance

b) C_D with various ground clearance

Figure 3.8 C_L and C_D variation of the RAE2822 airfoil with ground clearance at M = 0.7 and α = 4 deg.

The pressure contours and sonic line in Figure 3.9 show that the shock moves toward the leading edge as the ground clearance decreases from 1.0 to 0.1 and the sonic region also reduces in size. As the ground clearance decreases from h/c = 1.0 to 0.1, the pressure gradient in flow field before the airfoil increases.

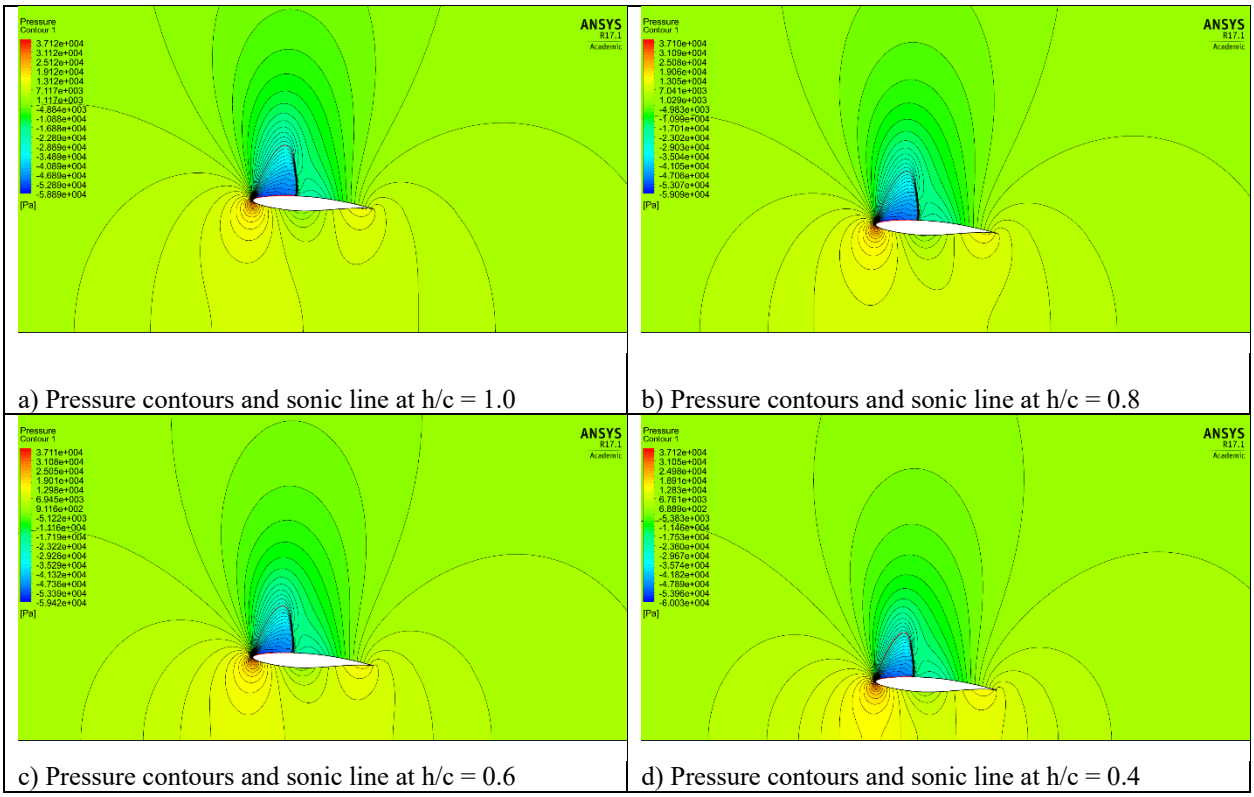

a) Pressure contours and sonic line at h/c = 1.0

b) Pressure contours and sonic line at h/c = 0.8

c) Pressure contours and sonic line at h/c = 0.6

d) Pressure contours and sonic line at h/c = 0.4

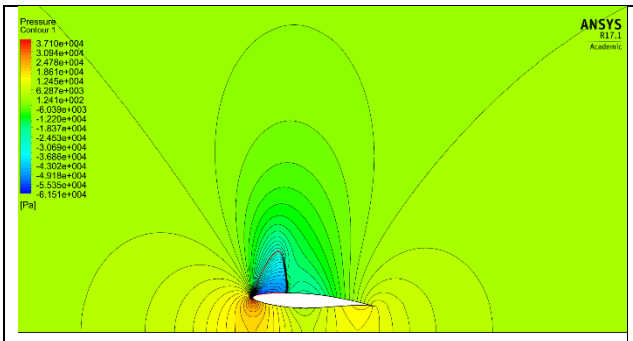

e) Pressure contours and sonic line at h/c = 0.2

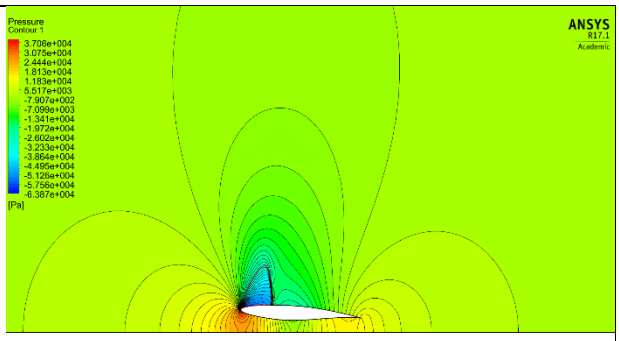

f) Pressure contours and sonic line at h/c = 0.1

Figure 3.9 Pressure contours and sonic line for various ground clearances at M = 0.7 and α = 4 deg.

Figure 3.10 shows the streamlines at the trailing edge of the airfoil for different ground clearances. The flow remains attached to the surface of the airfoil due to the relatively low angle of attack. No separation is observed with the variation in ground clearance.

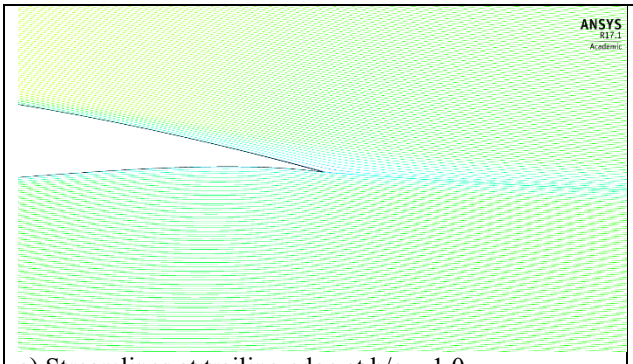

a) Streamlines at trailing edge at h/c = 1.0

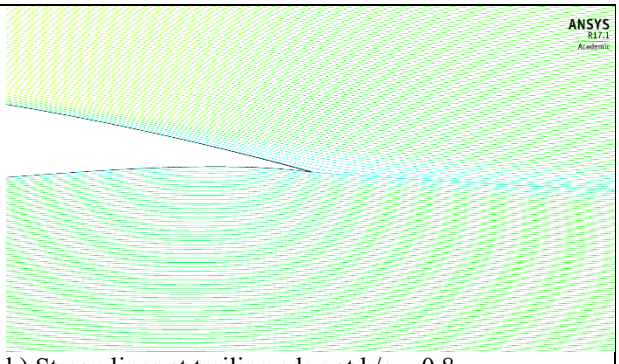

b) Streamlines at trailing edge at h/c = 0.8

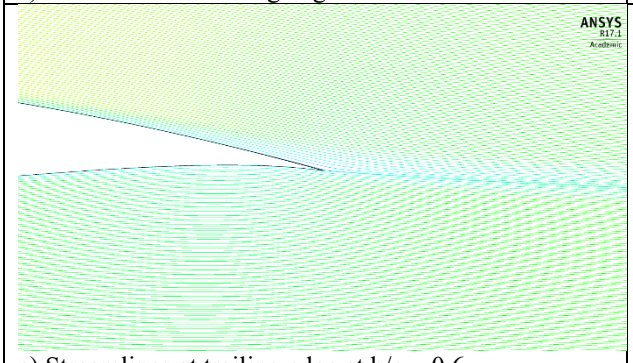

c) Streamlines at trailing edge at h/c = 0.6

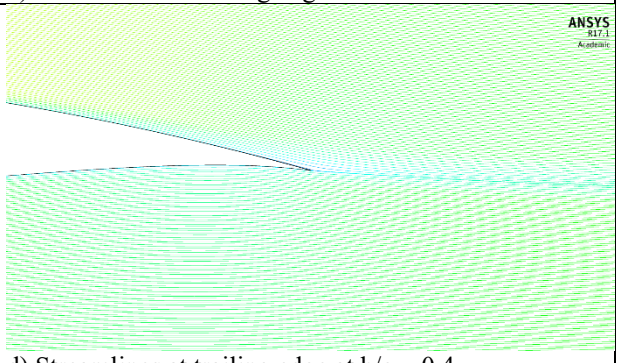

d) Streamlines at trailing edge at h/c = 0.4

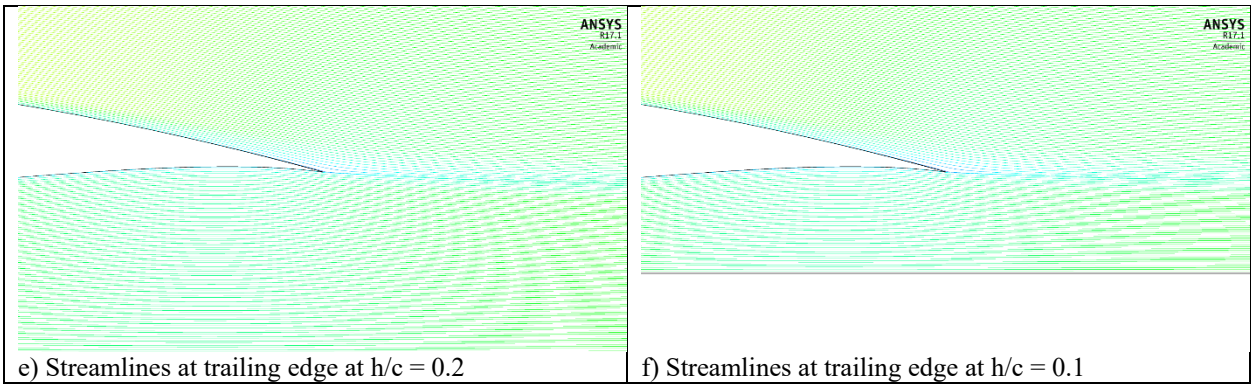

e) Streamlines at trailing edge at h/c = 0.2 f) Streamlines at trailing edge at h/c = 0.1

Figure 3.10 Streamlines at the trailing edge for various ground clearances at M = 0.7 and α = 4 deg.

Effect of Mach number

At higher ground clearance, the increase in Mach number causes only the upper surface shock to appear. Typical cases with $\alpha = 4$ deg and h/c = 0.8 for Mach numbers range 0.5 to 0.8 are analyzed in detail. Figure 3.11 shows the pressure coefficient of the airfoil for each case. At M = 0.5, there is no shock present. At M = 0.6, a very weak shock is present at the leading edge of the upper surface. Increasing the Mach number further, the shock moves further back and becomes stronger. The increase in C_L from M = 0.5 to 0.75 is mainly driven by the upper surface shock location. Figure 3.11 shows that the low pressure zone prior to the shock contributes to large amount lift especially from M = 0.6 to 0.7. At M = 0.6, the shock is very close to the leading edge causing the pressure to increase on the entire upper surface. At M = 0.7, the shock moves further back contributing to more lift. For M = 0.75 to M = 0.8, the shock does not move its position but the lift has a sharp drop. The pressure coefficient plot shows that the lower surface has a decrease in pressure and the upper surface has an increase in pressure ahead of the shock, both contributing to less in lift.

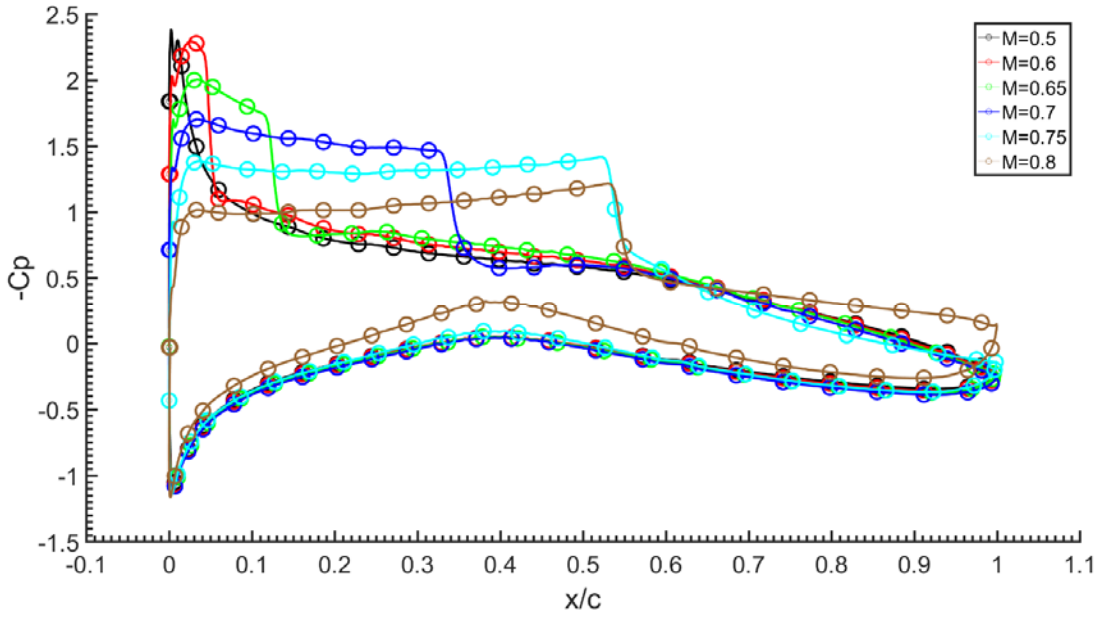

Figure 3.11 Pressure coefficient distribution on the RAE2822 airfoil at α = 4 deg and h/c = 0.8 for various Mach numbers.

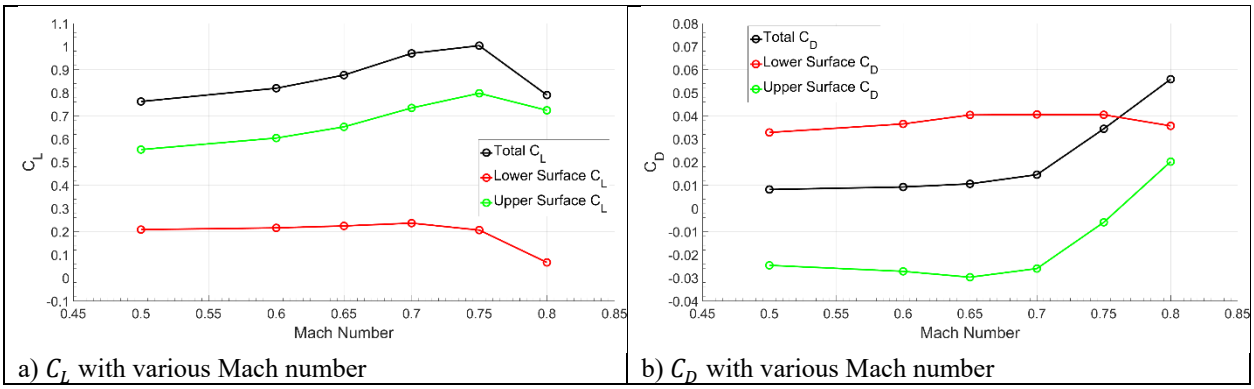

a) C_L with various Mach number

b) C_D with various Mach number

Figure 3.12 C_L and C_D variation with Mach number of the RAE2822 airfoil at α = 4 deg and h/c = 0.8.

Figure 3.13 shows the pressure contours and sonic line plot at different Mach numbers. The red line is the sonic line where the Mach number equals unity. The region inside the red line is locally supersonic flow. As the Mach number increases from 0.5 to 0.65, a very weak shock appears at the leading edge of the airfoil. With further increase in the Mach number, the shock becomes stronger and the sonic region increases in size.

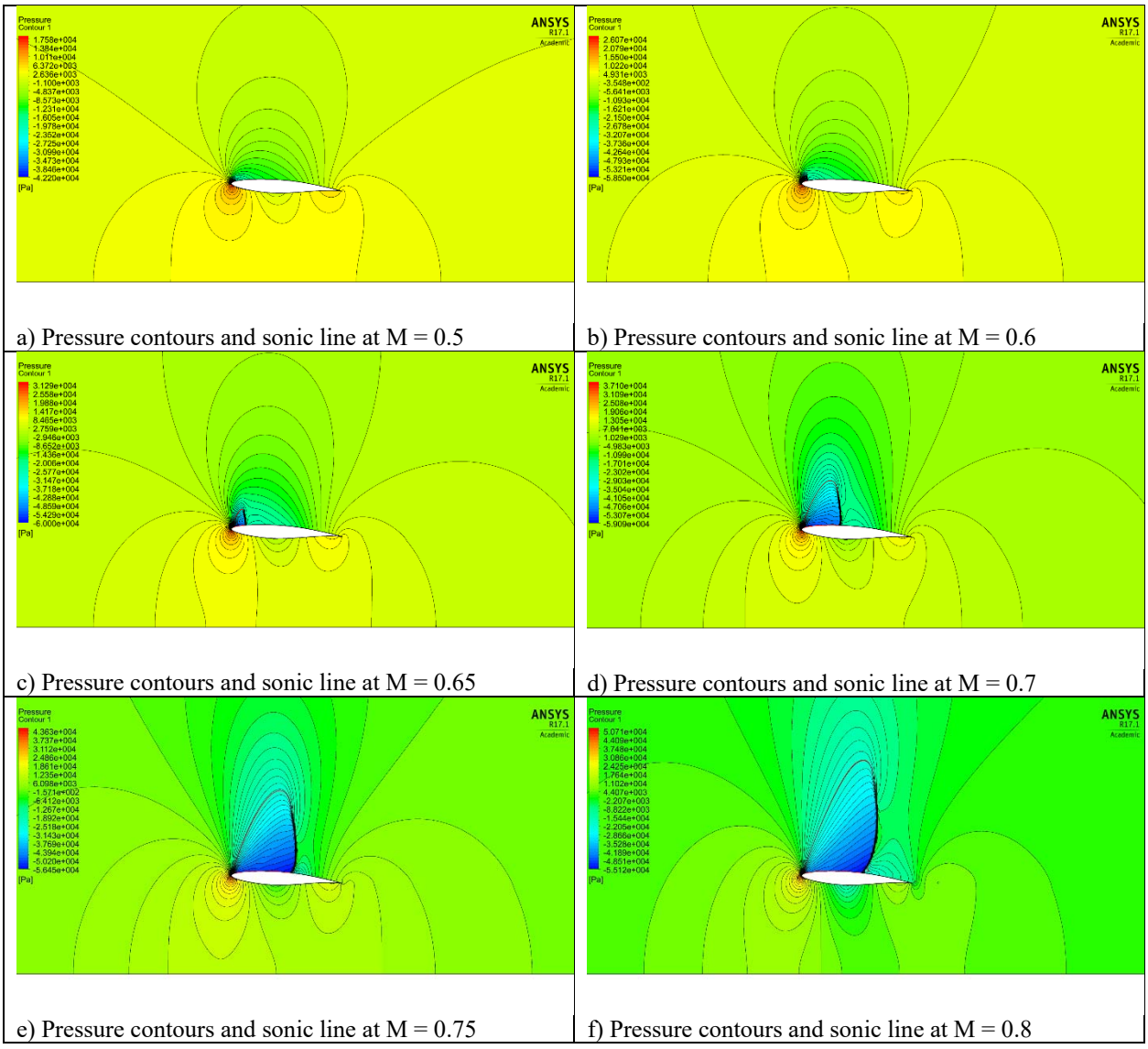

Figure 3.13 Pressure contours and sonic line for various Mach numbers at α = 4 deg and h/c = 0.8.

Further analysis of the flow field reveals that the position of the stagnation point on the airfoil changes dramatically from M = 0.5 to 0.75 as shown in Figure 3.14. The upward movement of the stagnation point corresponds to the upward movement of the stagnation streamline which separates the flow on the upper surface and the lower surface of the airfoil. This means that at the M = 0.8, there is more mass flow through the channel formed by the airfoil and the ground. Since there is no shock in the channel, the pressure decreases with increase in the flow velocity.

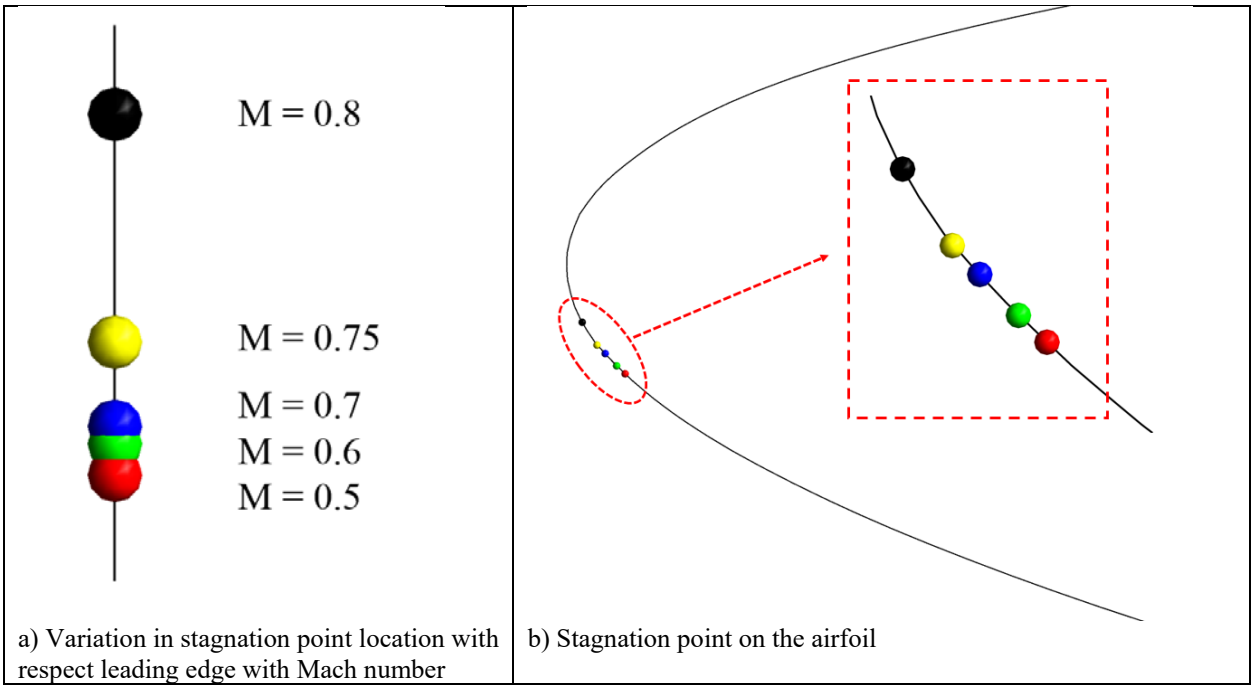

a) Variation in stagnation point location with respect leading edge with Mach number

b) Stagnation point on the airfoil

Figure 3.14 Stagnation point location on the RAE2822 airfoil at various Mach number with α = 4 deg and h/c = 0.8.

3.1.2 Low Ground Clearance

When the ground clearance further decreases from high ground clearance, it is likely that a lower surface shock would form between the airfoil and the ground. This would create a large low pressure zone behind the shock, which can lead to loss of lift. If the shock is strong enough to cause boundary layer separation, the drag would also increase due to the separation bubble. Figure 3.16 shows the pressure coefficient distributions on the airfoil at M = 0.8 and $\alpha = 4$ deg. When ground clearance reduces from h/c = ∞ to h/c = 0.1, the Venturi effect of the channel between the lower surface of the airfoil and the ground first creates a low pressure zone in the middle section of the airfoil which decreases the $C_{D,low}$ before $M_{cr,low}$ is reached which indicates the first appearance of shock on the lower surface. As the ground clearance further decreases, the mass flow between the airfoil and the ground becomes limited due to the lower ground clearance. The extra mass flow that cannot go through the channel is deflected to the upper surface, thereby increasing the suction peak at the leading edge of the airfoil. As a direct consequence of more mass

flow on the upper surface, the upper surface shock increases in strength causing a low pressure zone prior to the shock to further decrease the pressure, resulting in small enhancement in lift of the upper surface of the airfoil. The separation bubble increases in size and causes more drag as h/c decreases to 0.4. The lower surface has large region of low pressure prior to the shock in comparison to the high ground clearance case thereby significantly decreasing the lift. In case of lowest ground clearance, the lower surface has flow separation induced by the shock.

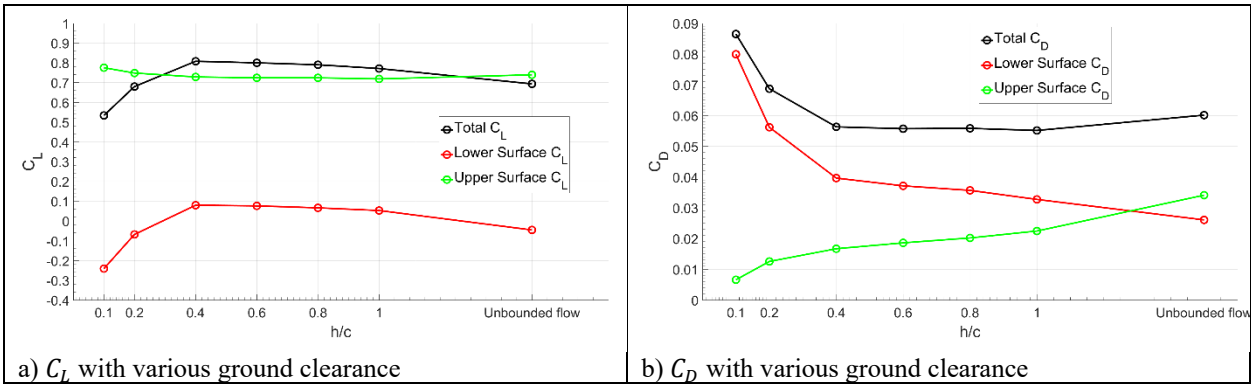

a) C_L with various ground clearance

b) C_D with various ground clearance

Figure 3.15 C_L and C_D variation of the RAE2822 airfoil with ground clearance at M = 0.8 and α = 4 deg.

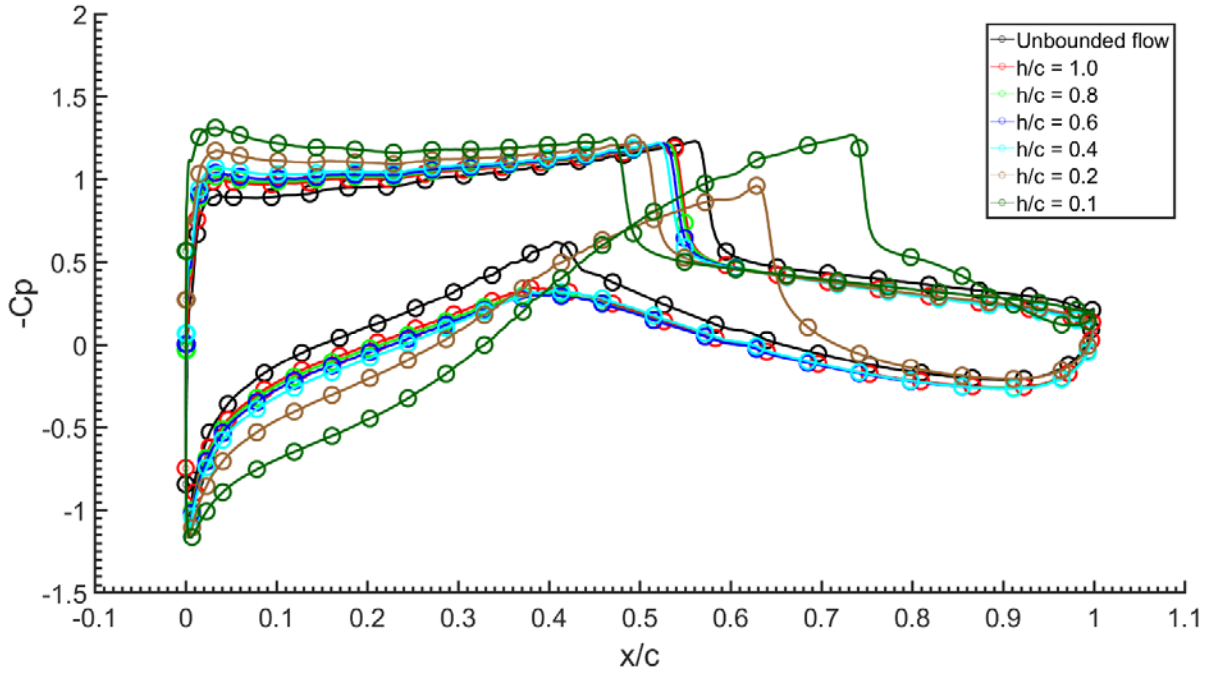

Figure 3.16 Pressure coefficient distribution on the RAE2822 airfoil for various ground clearances at M = 0.8 and α = 4 deg.

Figure 3.17 shows the streamlines around the airfoil for different ground clearances. The separation bubble at the trailing edge of the upper surface of the airfoil increases in size with decrease in ground clearance. For the lowest ground clearance of h/c = 0.1, the lower surface has mild flow separation.

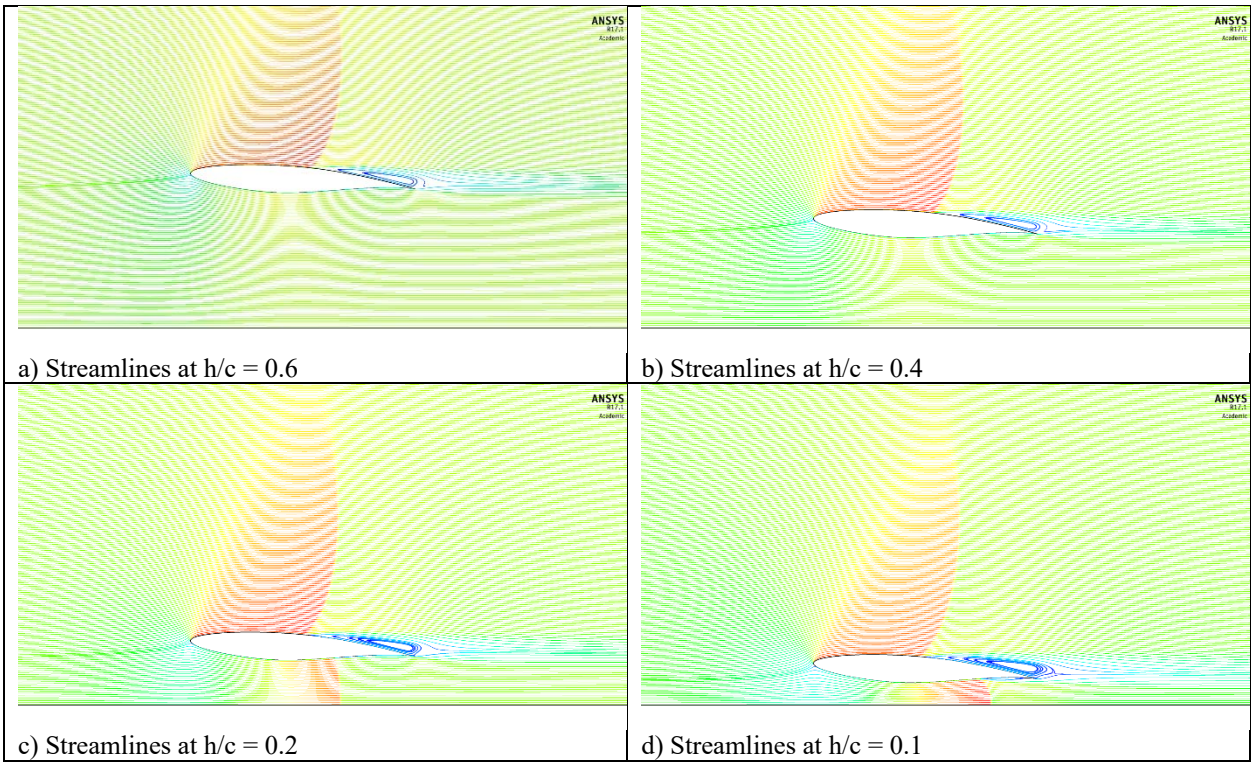

a) Streamlines at h/c = 0.6

b) Streamlines at h/c = 0.4

c) Streamlines at h/c = 0.2

d) Streamlines at h/c = 0.1

Figure 3.17 Streamlines of the RAE2822 airfoil for different ground clearances at M = 0.8 and α = 4 deg.

Effect of Mach number

At low ground clearance, increasing the Mach number would cause more mass flow to through the channel formed by the airfoil and the ground. The flow through the channel would increase in velocity as the Mach number increases eventually becoming supersonic. Once the flow becomes supersonic, it gets choked. The converging-diverging nozzle theory suggests that the mass flow would be at its maximum. Further increase in the Mach number would not add any more mass flow through the channel and the flow field would adjusts itself upstream resulting in change in

the position of the stagnation point. A typical case of $\alpha = 2$ deg and h/c = 0.1 with variations in Mach number is analyzed in detail.

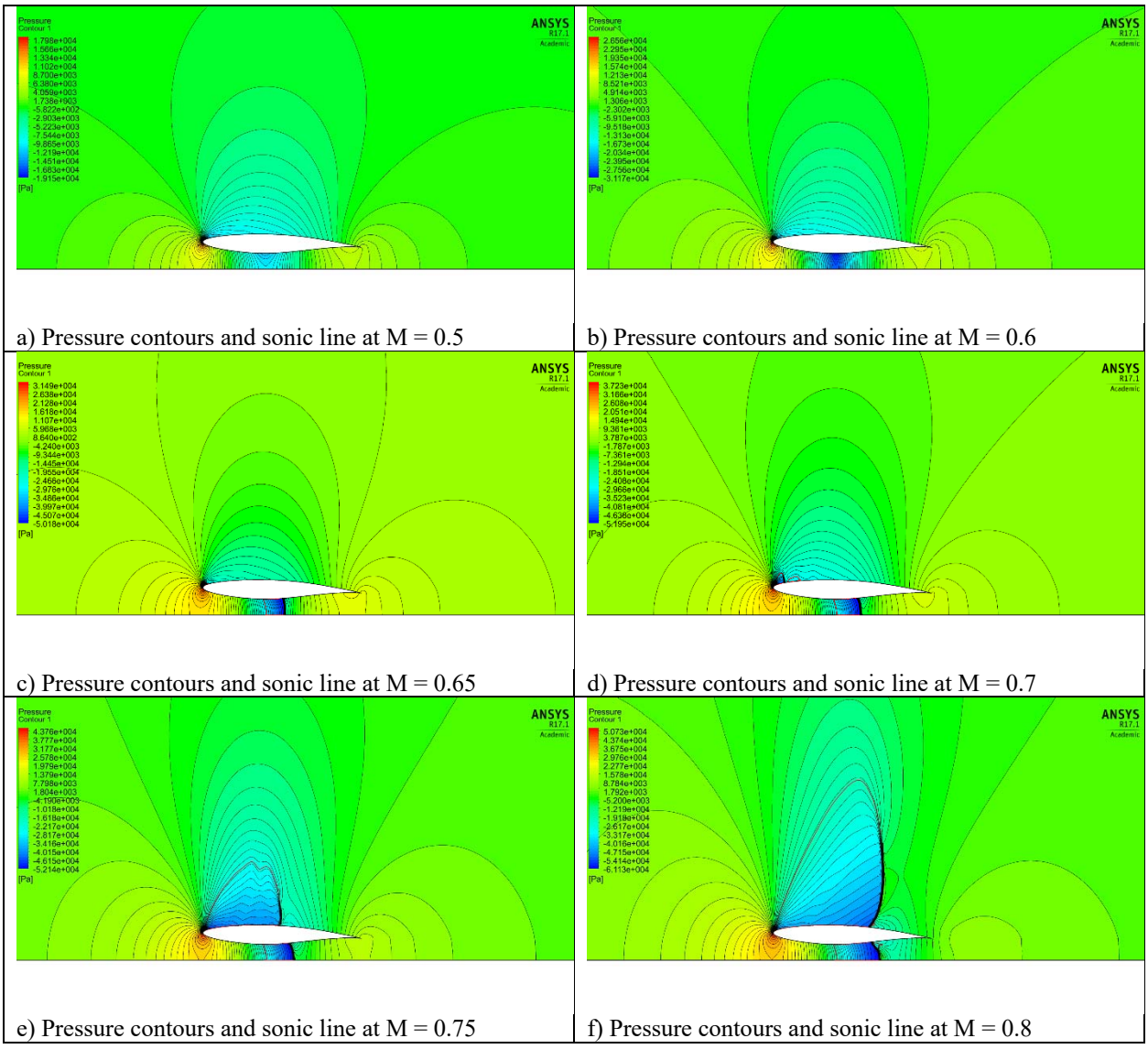

a) Pressure contours and sonic line at M = 0.5

b) Pressure contours and sonic line at M = 0.6

c) Pressure contours and sonic line at M = 0.65

d) Pressure contours and sonic line at M = 0.7

e) Pressure contours and sonic line at M = 0.75

f) Pressure contours and sonic line at M = 0.8

Figure 3.18 Pressure contours and sonic line for various Mach numbers at α = 2 deg and h/c = 0.1.

From M = 0.5 to 0.6, the flow through the channel is subsonic and the Venturi effect becomes stronger when the Mach number increases from 0.5 to 0.6 as shown in Figure 3.19. The lower surface pressure is much lower at M = 0.6 than at M = 0.5. Increasing the Mach number to 0.65, the lower surface shock emerges at x/c = 0.52 and the flow becomes choked. Further increasing the Mach number, the position of the beginning of the lower sonic region remains unchanged while

the shock moves further back, corresponding to the converging-diverging nozzle theory. The upper surface shock begins to appear due to both the increase in freestream velocity and the upward movement of the stagnation point. The aerodynamic forces shown in Figure 3.20 indicate that the lower surface always contributes negative lift in this situation. This is due to the Venturi effect when the flow is subsonic and the occurrence of low pressure region prior to the shock when the flow is transonic. The upper surface pressure decreases in the pressure plateau region from M = 0.5 to 0.65 due to increase in mass flow over the upper surface. From M = 0.7 to 0.8, the shock moves to the trailing edge, enlarges the low pressure region prior to the shock, resulting in a steady lift increase on the upper surface.

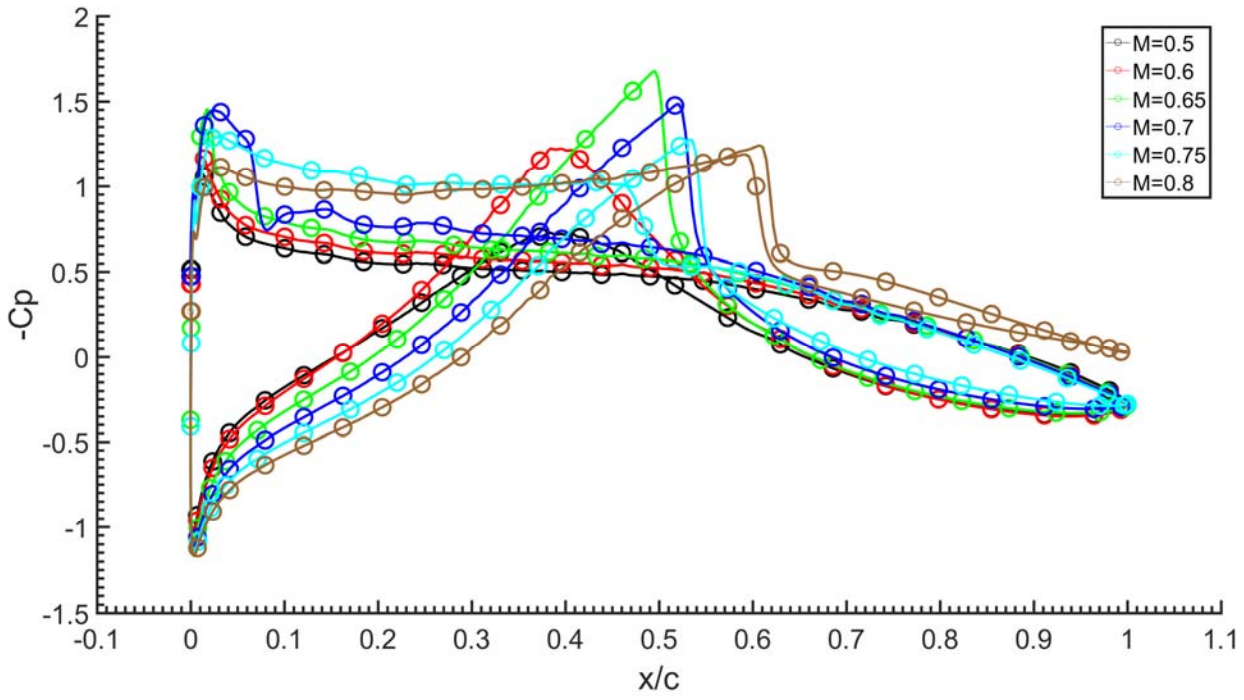

Figure 3.19 Pressure coefficient distribution on the RAE2822 airfoil at α = 2 deg and h/c = 0.1 for various Mach numbers.

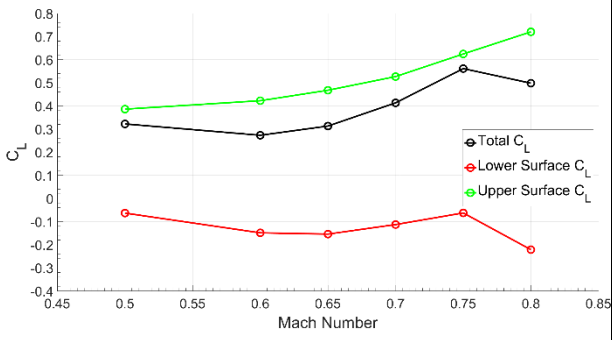

a) C_L with various Mach number

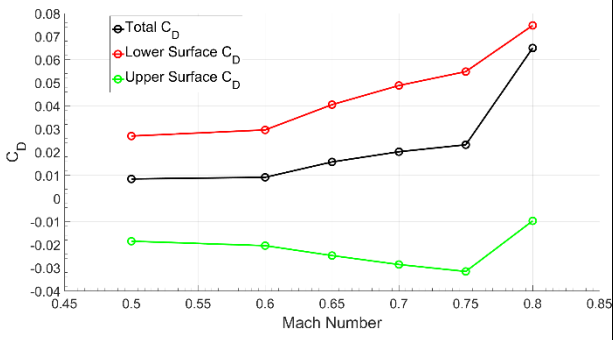

b) C_D with various Mach number

Figure 3.20 C_L and C_D variation of the RAE2822 airfoil with various Mach numbers at α = 2 deg and h/c = 0.1.

3.2 Shock Buffet

In several calculations, unsteady flow behavior was observed. There are two types of unsteady flow cases found in the simulations. The first type has only upper surface shock oscillation associated with shock/boundary-layer interaction. The second type has shock oscillation on both the surfaces; the lower surface shock is associated with the shock/boundary-layer interaction while the upper shock movement is coupled with the pressure divergence at the trailing edge.

3.2.1 Shock Oscillation on the Upper Surface Only

The majority of self-sustained shock movement observed in the simulation is of this type. When the flow moves over the airfoil at medium to high angle of attack, the flow on the upper surface of the airfoil is accelerated to become supersonic creating a shock that separates the boundary layer. A typical case of M = 0.7 and $\alpha = 6$ deg in unbounded flow is analyzed in detail.

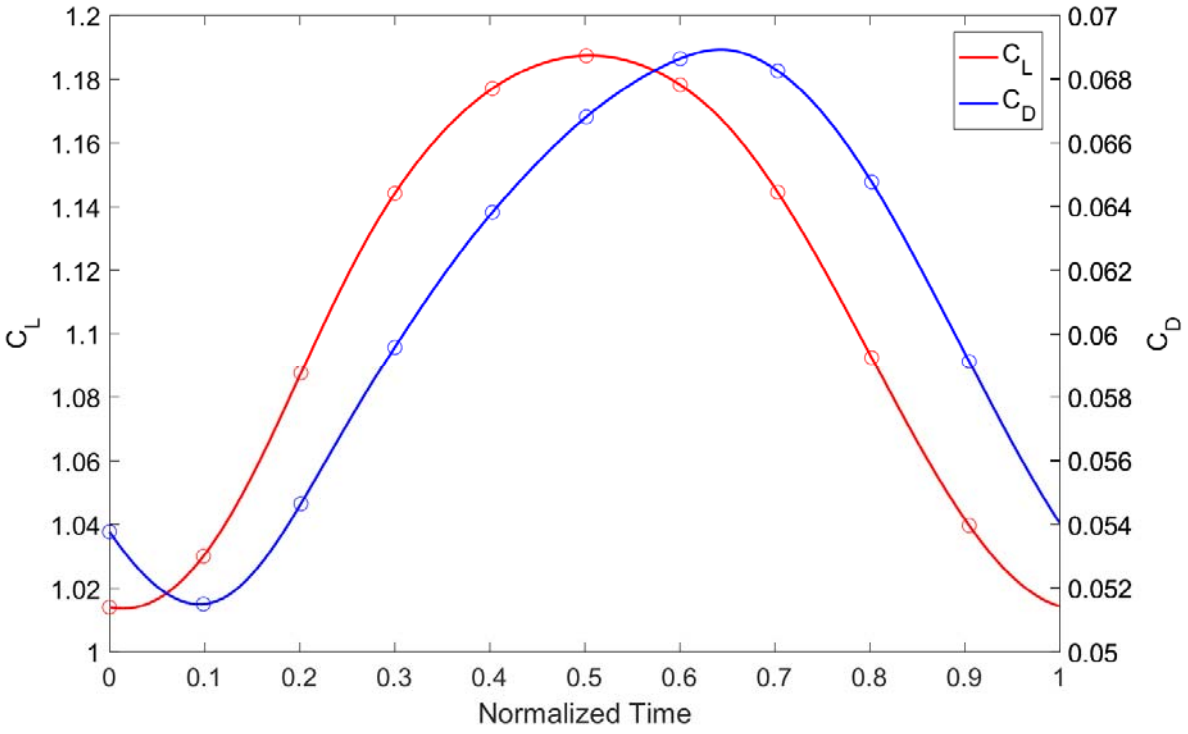

Figure 3.21 C_L and C_D time history of the RAE2822 airfoil at M = 0.7 and α = 6 deg in unbounded flow field.

The self-sustained shock movement has a reduced frequency of $k = \frac{\pi f c}{U_\infty} = 0.197$. The lift and drag coefficient history in one period is shown in figure 3.21. The t* = 0 corresponds to the instant at which lift coefficient is at its minimum and t* = 1 represents a full period of the shock buffet movement. The lift varies 15.6% in one period and the drag varies 28.7% in one period. The Mach-number contours are shown in Figure 3.22. From t* = 0 to 0.5, the upper surface shock moves towards the trailing edge with a small decrease in strength and moves forward to the leading edge from t* = 0.5 to 1.0. The streamlines shown in Figure 3.23 also have periodic behavior from t* = 0.2 to 0.5; as the shock already begin to move toward the trailing edge, the flow past behind the shock has a bulge. At t* = 0.5, as the shock stops moving toward the trailing edge and begins to move toward the leading edge, the flow starts to separate. The separation region enlarges from t*

= 0.5 to 0.9, and reduces its size when the shock stops its forward movement. The cycle of boundary layer separation and shock movement then repeats itself.

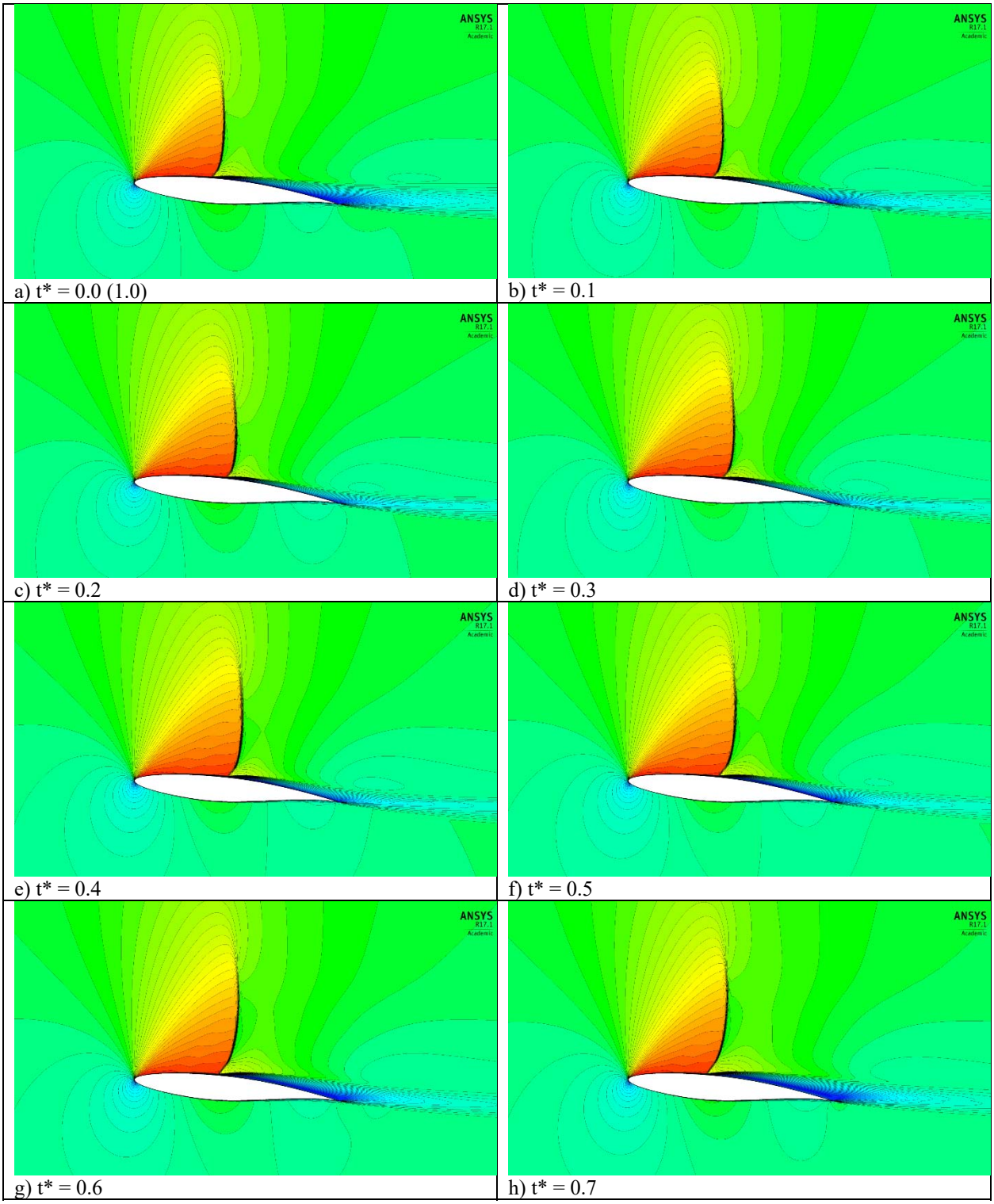

a) t* = 0.0 (1.0) b) t* = 0.1

c) t* = 0.2 d) t* = 0.3

e) t* = 0.4 f) t* = 0.5

g) t* = 0.6 h) t* = 0.7

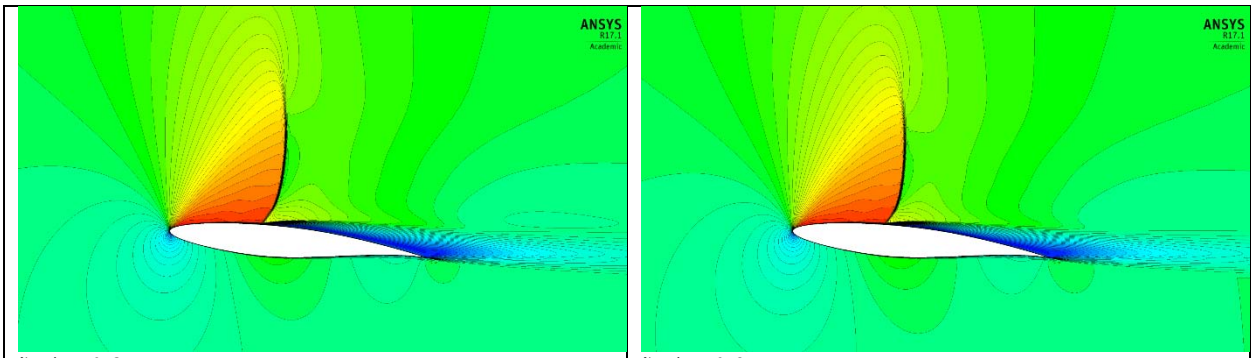

i) t* = 0.8 j) t* = 0.9

Figure 3.22 Mach number contours at M = 0.7 and α = 6 deg in unbounded flow field in one period.

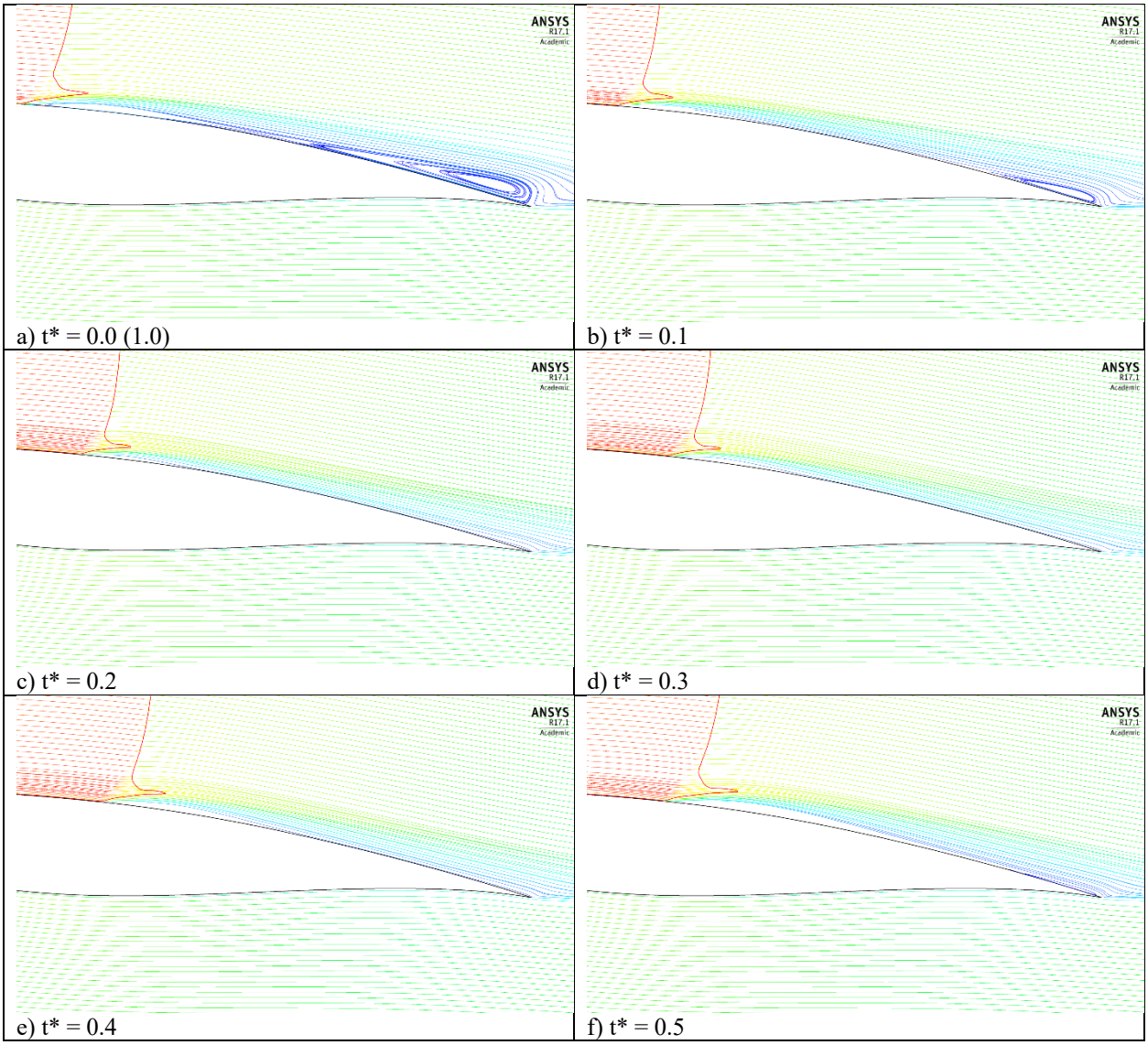

a) t* = 0.0 (1.0) b) t* = 0.1

c) t* = 0.2 d) t* = 0.3

e) t* = 0.4 f) t* = 0.5

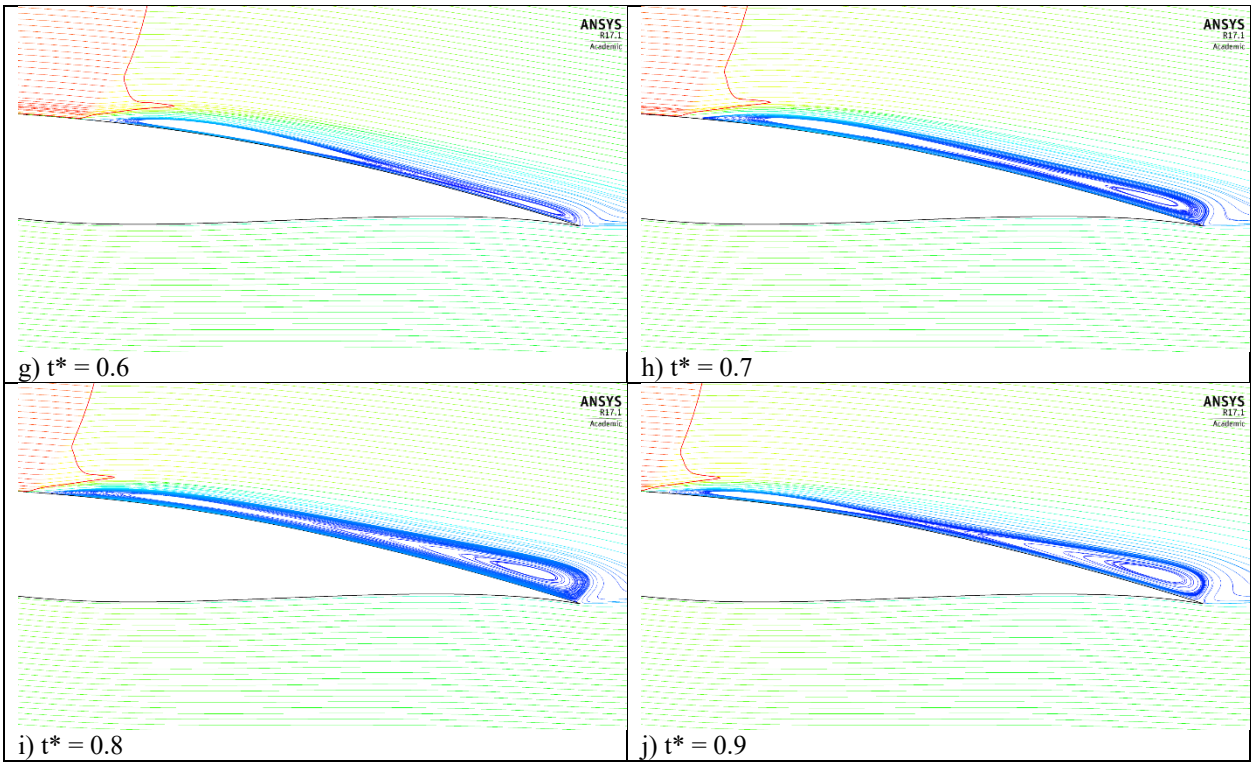

Figure 3.23 Streamlines on the upper surface at M = 0.7 and α = 6 deg in unbounded flow field in one period.

From the pressure coefficient shown below in Figure 3.24, the shock moves from x/c = 0.36 to x/c = 0.45 in the first half of the period and backward during the last half of the period. The pressure on the lower surface of the airfoil and on the upper surface ahead of the shock is not affected much due to the shock buffet. The variation in the flow field downstream of the shock does not propagate upstream. The lift coefficient changes behind the shock and is influenced by the position and strength of the shock.

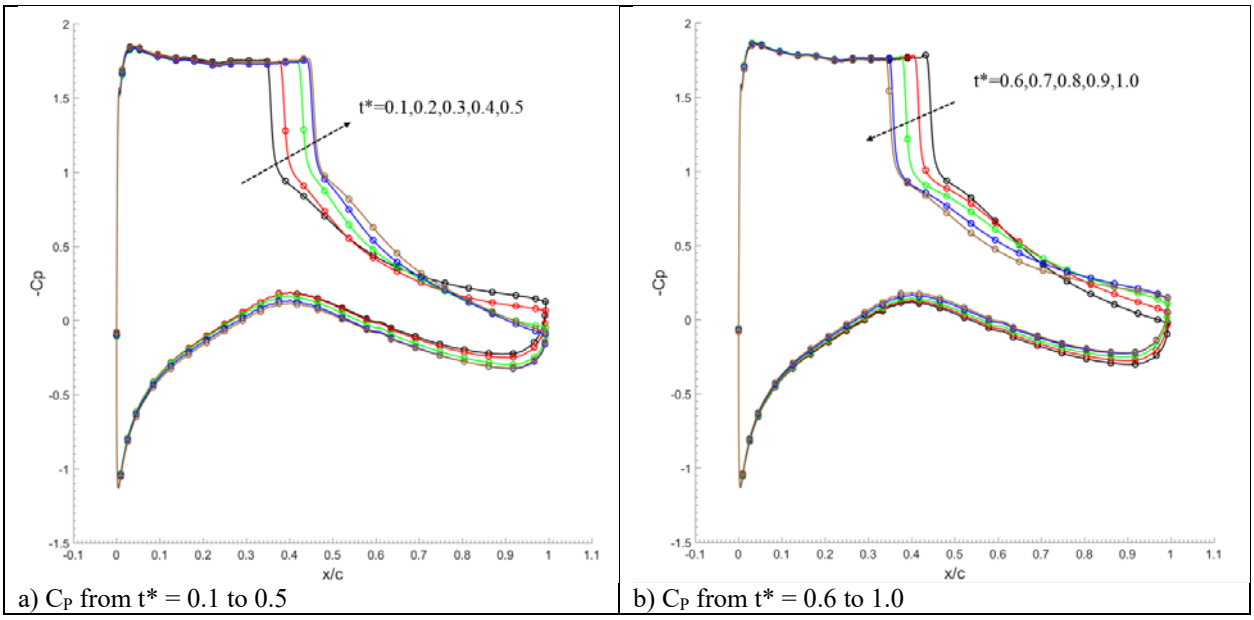

a) C_P from t* = 0.1 to 0.5 b) C_P from t* = 0.6 to 1.0

Figure 3.24 Pressure coefficient distributions at M = 0.7 and α = 6 deg in unbounded flow field during one period.

Effect of ground clearance

While the exact mechanism of the shock buffet is not fully understood, the theory proposed by B.H.K. Lee suggests that the pressure divergence at the trailing edge sends pressure waves upstream which interact with the shock. The ground effect changes the pressure distribution around the airfoil. The pressure on the lower surface is changed by the ground effect while the shock buffet on the upper surface is not much affected. The unsteady cases of $\alpha = 8$ deg and M = 0.7 for various ground clearances are analyzed in detail.

Figure 3.26 shows the time-averaged lift and drag coefficient for these cases. The overall lift coefficient is slightly increased with decrease in ground clearance. The lower surface is the main contributeor to the increase in lift. The drag coefficient shows a similar trend. The upper surface drag coefficient varies from 0.55 for unbounded flow to 0.45 at h/c = 0.2. The time-averaged pressure coefficients are shown in Figure 3.25. They reveal that the pressure differences on the lower surface are much more obvious compare to these on the upper surface of the airfoil for various ground clearances.

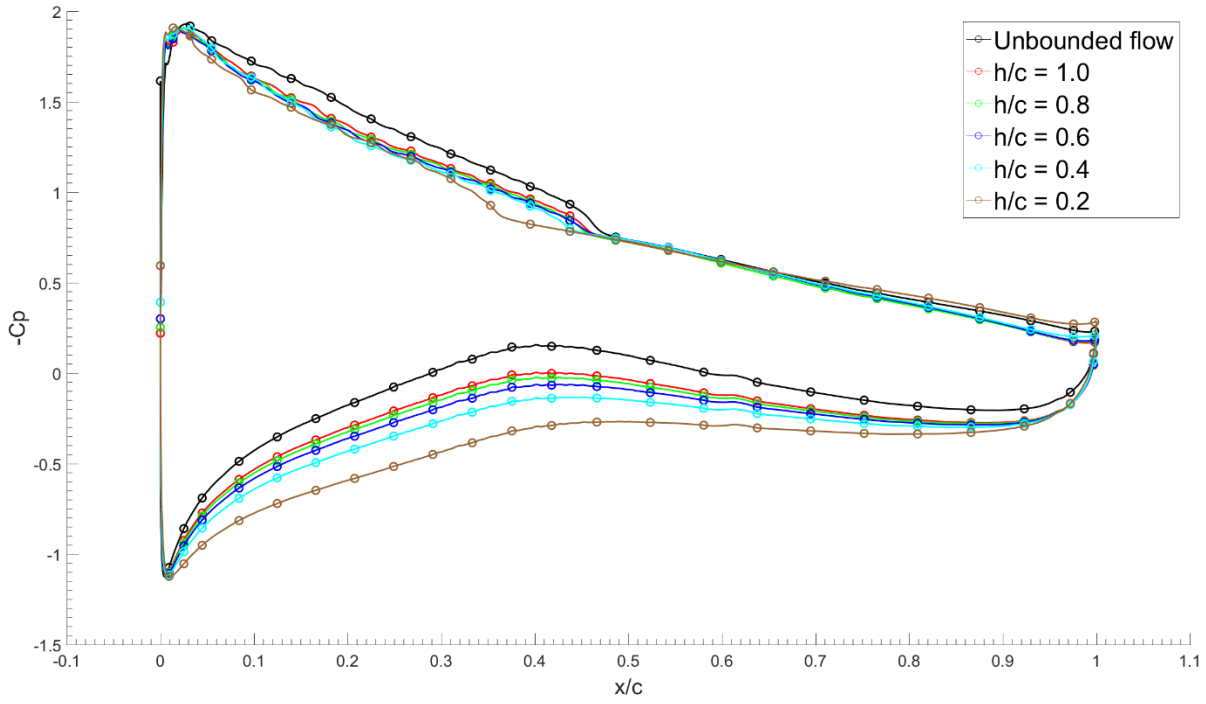

Figure 3.25 Time-averaged C_P distribution for various ground clearances at M = 0.7 and α = 8 deg.

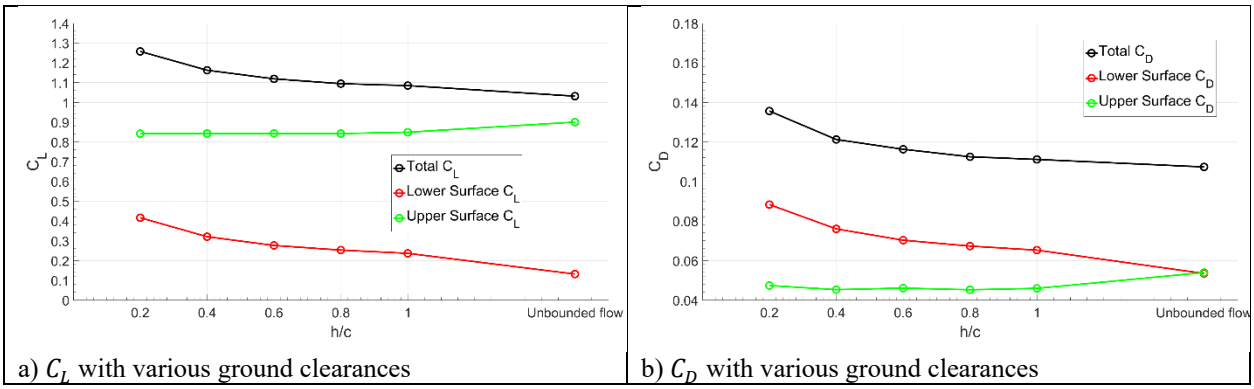

a) C_L with various ground clearances

b) C_D with various ground clearances

Figure 3.26 C_L and C_D variation of the RAE2822 airfoil at M = 0.7 and α = 8 deg.

Figures 3.27 and 3.28 show the lift and drag coefficient history in one period for $\alpha = 8$ deg and M = 0.7 for various ground clearances; note that he time period starts when the lift coefficient is at its minimum. The flow time is normalized for the ease of comparisons. The lift coefficient in unbounded flow oscillates 36.8%; it increases from t* = 0 to 0.5 and decreases from t* = 0.5 to 1. The ground effect of increases the oscillation in lift coefficients to about 40% for h/c = 1.0 to 0.4

while the lift increase from t* = 0 to 0.4, maintains the maximum value from t* = 0.4 to 0.6, and then decreases to the minimum value.

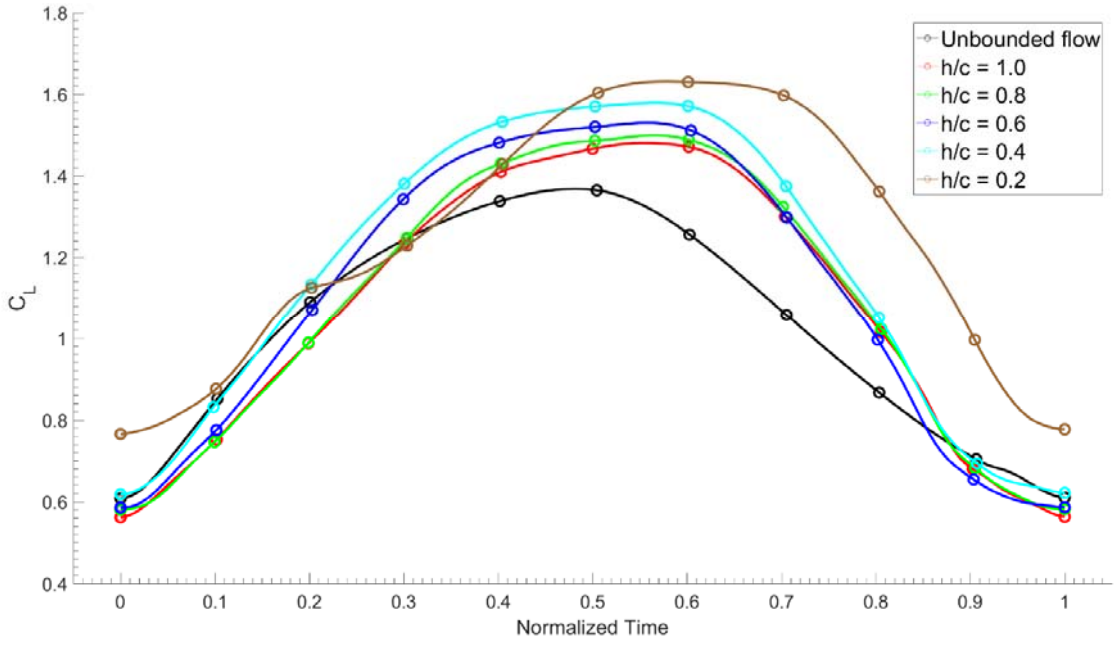

Figure 3.27 C_L history of the RAE2822 airfoil for various ground clearances at M = 0.7 and α = 8 deg.

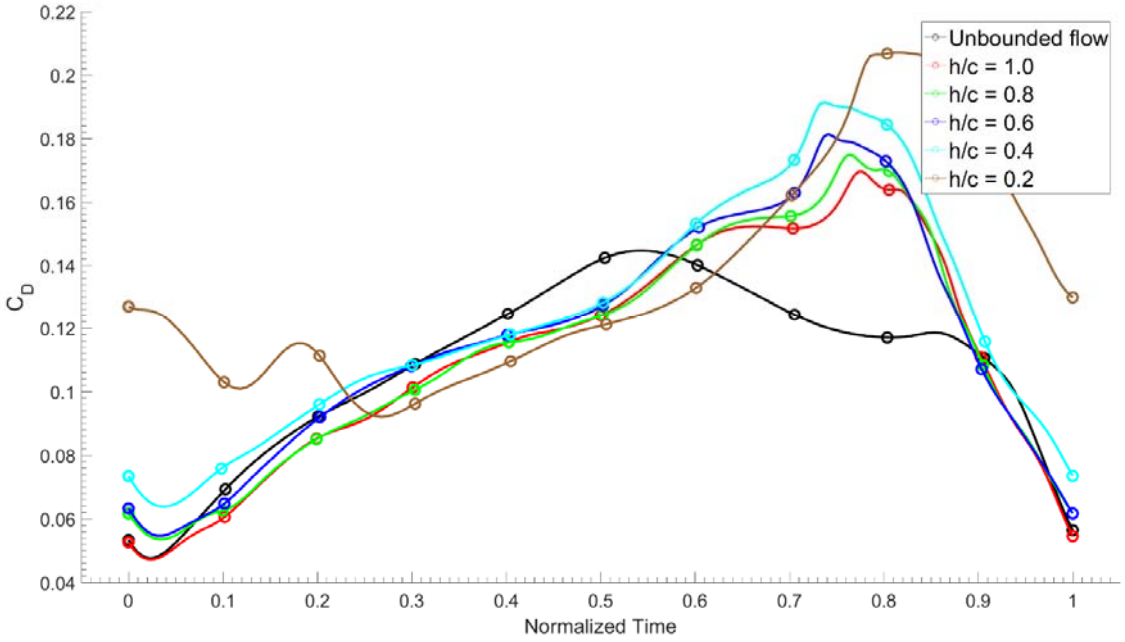

Figure 3.28 C_D history of the RAE2822 airfoil for various ground clearances at M = 0.7 and α = 8 deg.

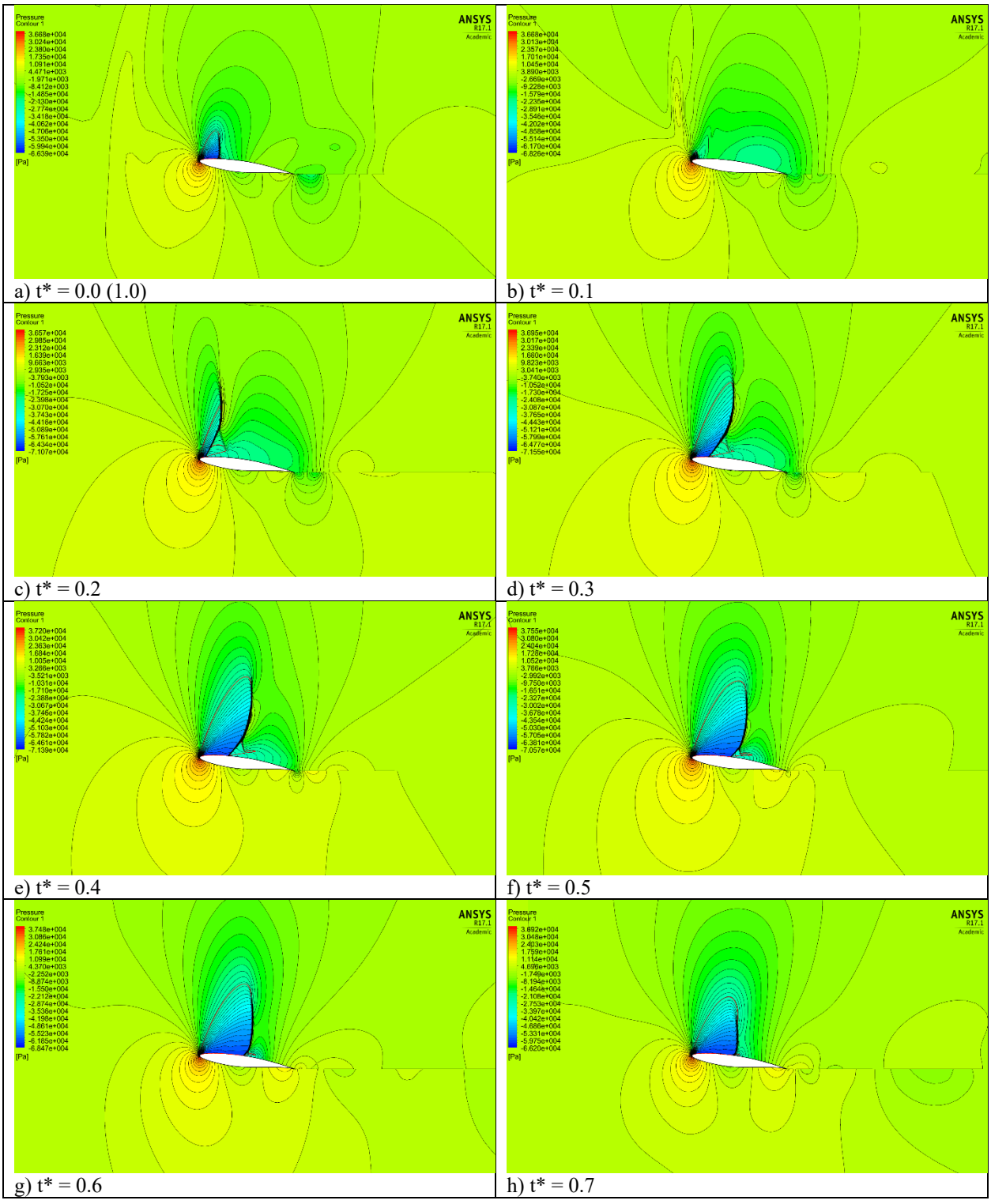
Pressure
Contour 1
3.668e+004
3.024e+004
2.380e+004
1.735e+004
1.091e+004
4.471e+003
-1.971e+003
-8.412e+003
-1.485e+004
-2.130e+004
-2.774e+004
-3.418e+004
-4.062e+004
-4.706e+004
-5.350e+004
-5.994e+004
-6.639e+004
[Pa]
ANSYS
R17.1
Academic
a) t* = 0.0 (1.0)
Pressure
Contour 1
3.668e+004
3.013e+004
2.357e+004
1.701e+004
1.045e+004
3.889e+003
-2.669e+003
-9.228e+003
-1.579e+004
-2.235e+004
-2.891e+004
-3.548e+004
-4.202e+004
-4.858e+004
-5.514e+004
-6.170e+004
-6.826e+004
[Pa]
ANSYS
R17.1
Academic
b) t* = 0.1
Pressure
Contour 1
3.657e+004
2.985e+004
2.312e+004
1.639e+004
9.663e+003
2.935e+003
-3.793e+003
-1.052e+004
-1.725e+004
-2.398e+004
-3.070e+004
-3.743e+004
-4.416e+004
-5.089e+004
-5.761e+004
-6.434e+004
-7.107e+004
[Pa]
ANSYS
R17.1
Academic
c) t* = 0.2
Pressure
Contour 1
3.695e+004
3.017e+004
2.339e+004
1.660e+004
9.823e+003
3.041e+003
-3.740e+003
-1.052e+004
-1.730e+004
-2.408e+004
-3.087e+004
-3.765e+004
-4.443e+004
-5.121e+004
-5.799e+004
-6.477e+004
-7.155e+004
[Pa]
ANSYS
R17.1
Academic
d) t* = 0.3
Pressure
Contour 1
3.720e+004
3.042e+004
2.363e+004
1.684e+004
1.005e+004
3.266e+003
-3.521e+003
-1.031e+004
-1.710e+004
-2.388e+004
-3.067e+004
-3.746e+004
-4.424e+004
-5.103e+004
-5.782e+004
-6.461e+004
-7.139e+004
[Pa]
ANSYS
R17.1
Academic
e) t* = 0.4
Pressure
Contour 1
3.755e+004
3.080e+004
2.404e+004
1.728e+004
1.052e+004
3.768e+003
-2.992e+003
-9.750e+003
-1.651e+004
-2.327e+004
-3.002e+004
-3.678e+004
-4.354e+004
-5.030e+004
-5.705e+004
-6.381e+004
-7.057e+004
[Pa]
ANSYS
R17.1
Academic
f) t* = 0.5
Pressure
Contour 1
3.748e+004
3.086e+004
2.424e+004
1.761e+004
1.099e+004
4.370e+003
-2.252e+003
-8.874e+003
-1.550e+004
-2.212e+004
-2.874e+004
-3.536e+004
-4.198e+004
-4.861e+004
-5.523e+004
-6.185e+004
-6.847e+004
[Pa]
ANSYS
R17.1
Academic
g) t* = 0.6
Pressure
Contour 1
3.892e+004
3.048e+004
2.403e+004
1.759e+004
1.114e+004
4.698e+003
-1.749e+003
-8.194e+003
-1.464e+004
-2.108e+004
-2.753e+004
-3.397e+004
-4.042e+004
-4.686e+004
-5.331e+004
-5.975e+004
-6.620e+004
[Pa]
ANSYS
R17.1
Academic
h) t* = 0.7

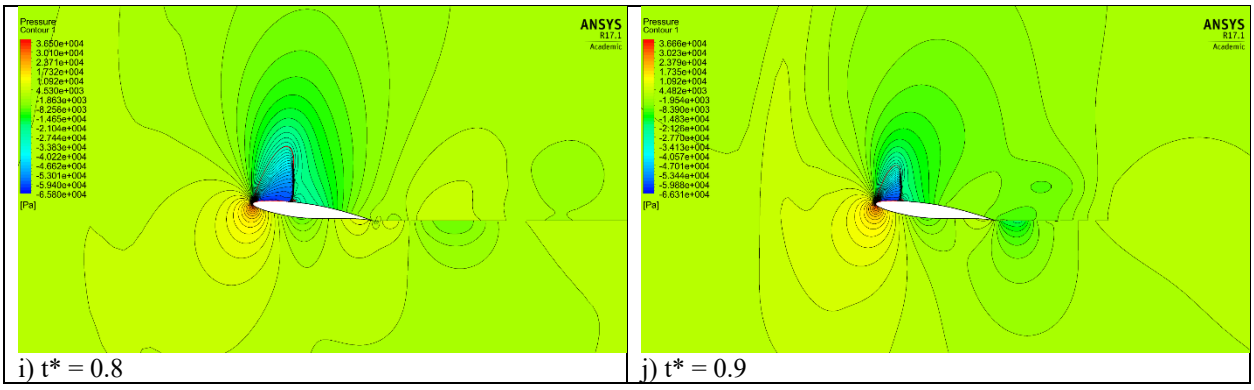

i) t* = 0.8 j) t* = 0.9

Figure 3.29 Pressure contours and sonic line at M = 0.7 and α = 8 deg in unbounded flow in one period.

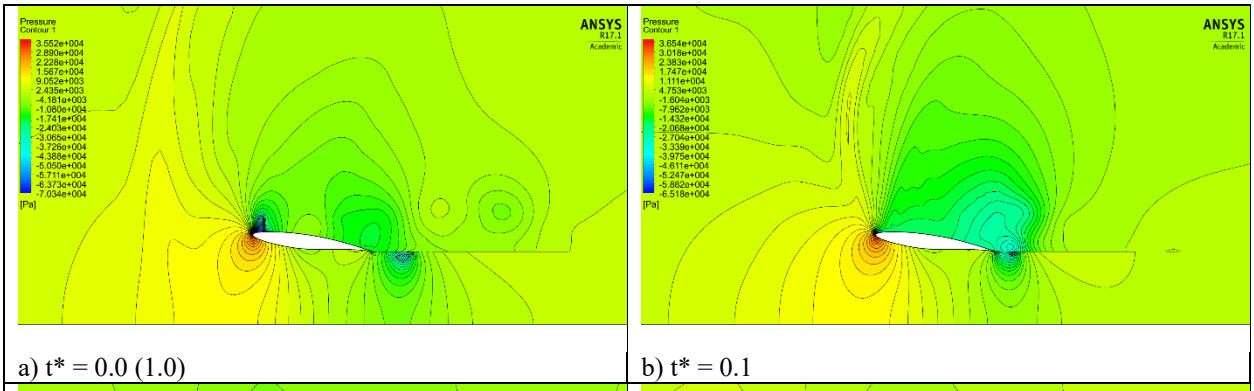

a) t* = 0.0 (1.0) b) t* = 0.1

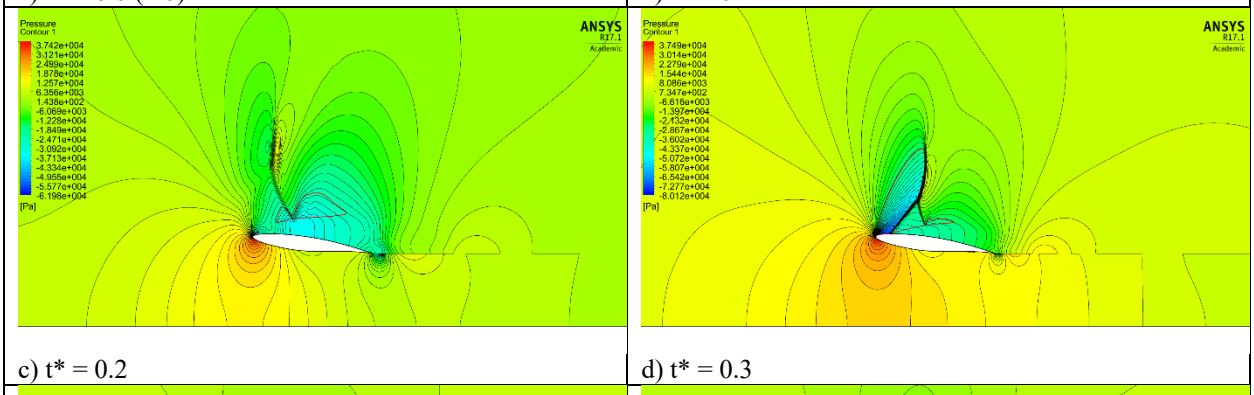

c) t* = 0.2 d) t* = 0.3

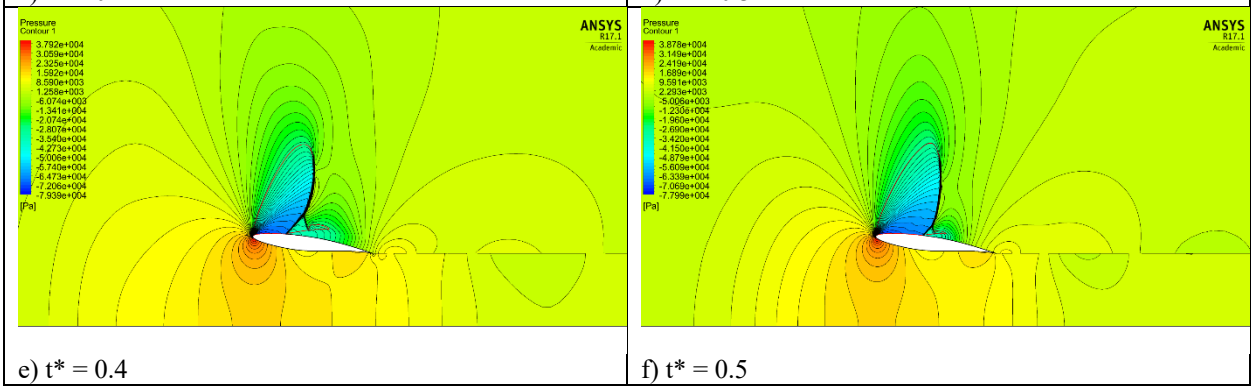

e) t* = 0.4 f) t* = 0.5

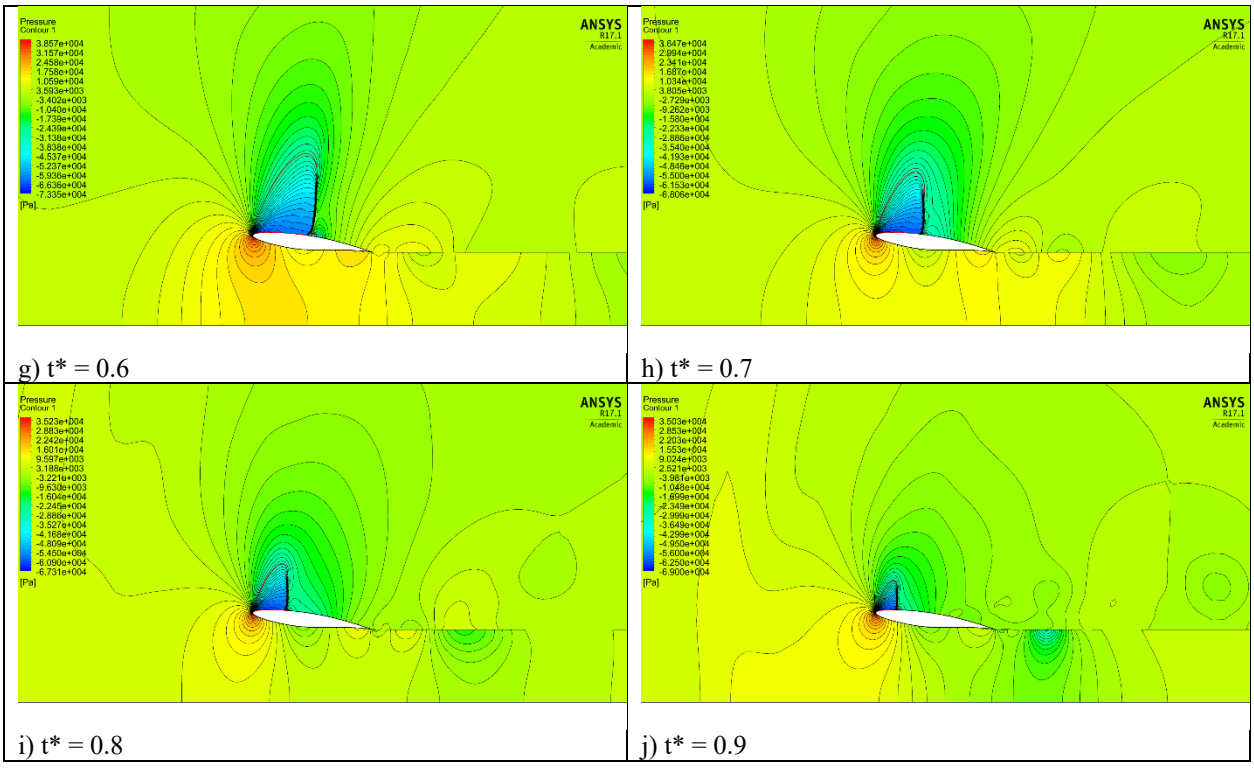

g) t* = 0.6 h) t* = 0.7

i) t* = 0.8 j) t* = 0.9

Figure 3.30 Pressure contours and sonic line at M = 0.7, α = 8 deg and h/c = 0.6 in one period.

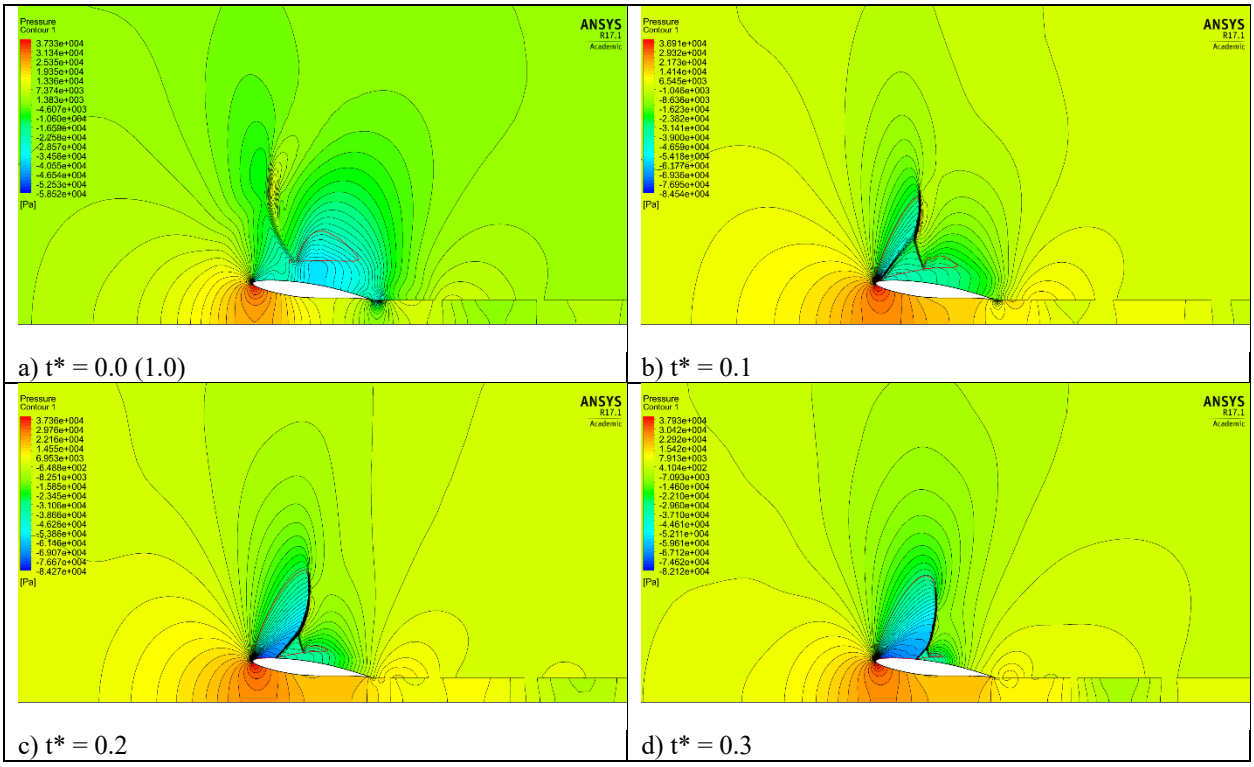

a) t* = 0.0 (1.0) b) t* = 0.1

c) t* = 0.2 d) t* = 0.3

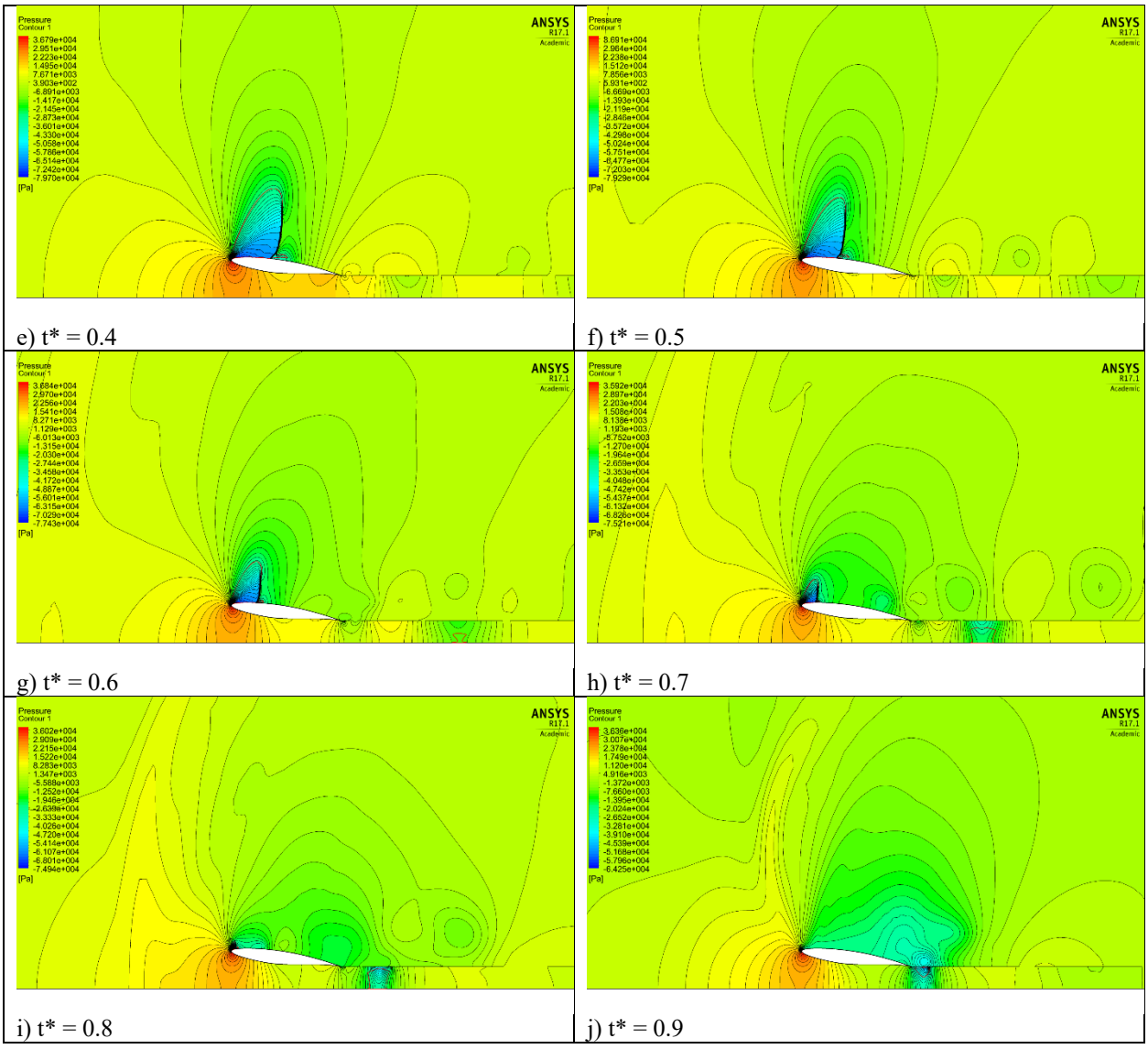

Figure 3.31 Pressure contours and sonic line at M = 0.7, α = 8 deg and h/c = 0.2 in one period.

Figures 3.29 to 3.31 show the pressure contours and sonic line of the shock buffet in unbounded flow and in different ground clearance. For the unbounded flow and h/c = 0.6, the upper surface shock is at its minimum at t* = 0.1 and moves backward at t* = 0.1 to 0.6. While the h/c = 0.2 case shows the minimum shock at t* = 0.9 and the backward movement of the shock from t* = 0.9 to t* = 0.4. All these cases show similar upper surface shock movement while the difference in lift is mainly caused by the lower surface pressure distribution.

3.2.2 Coupled Shock Oscillation on Both Surfaces

At low angle of attack, low ground clearance and relatively high Mach number, a coupled oscillation of lower surface and upper surface shock movement was observed. This type of self-sustained shock oscillation was not observed in the previous research. The lower surface shock oscillation was combined with boundary layer separation. The oscillation of pressure divergence at the trailing edge of the airfoil causes the upper surface shock to have a combined movement. A typical case of M = 0.8, $\alpha = 1$ deg and h/c = 0.2 is analyzed in detail.

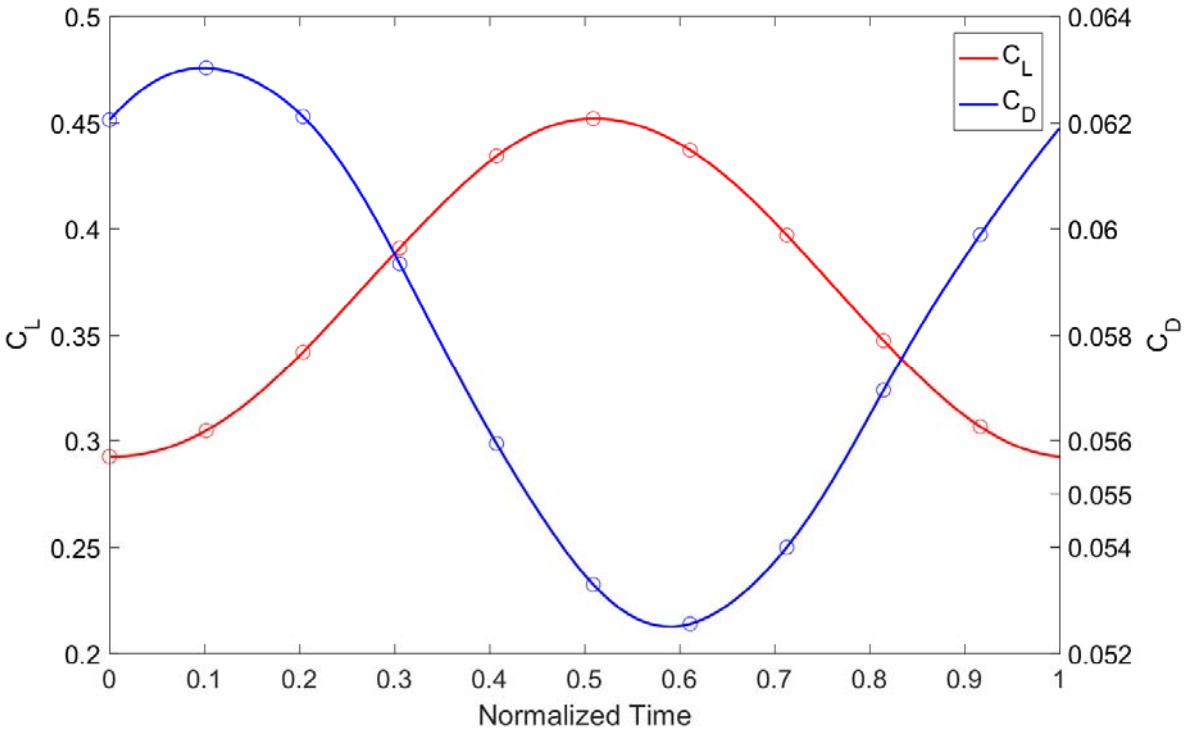

Figure 3.32 C_L and C_D history of the RAE2822 airfoil at M = 0.8, α = 1 deg and h/c = 0.2.

Similar to the case of upper surface shock oscillation, from t* = 0 to 0.5, lift increases. Drag has a 140 degree phase lead with respect to the lift as shown in Figure 3.32. In the pressure coefficient plot in figure 3.33, from t* = 0 to 0.5, the lower surface shock moves from x/c = 0.65 to 0.58 while increasing its strength. The upper surface shock moves from x/c = 0.651 to 0.689. From t* = 0.5 to 1.0, the lower surface shock moves from x/c = 0.58 to 0.644, while the upper surface shock

moves from x/c = 0.689 to 0.648. The upper and lower surface shock are opposite in phase in their combined movement. The increase in the strength of the lower surface shock when moving forward can be explained by the fact that it is being more oblique near the trailing edge compared to a more normal shock near the middle section of the airfoil.

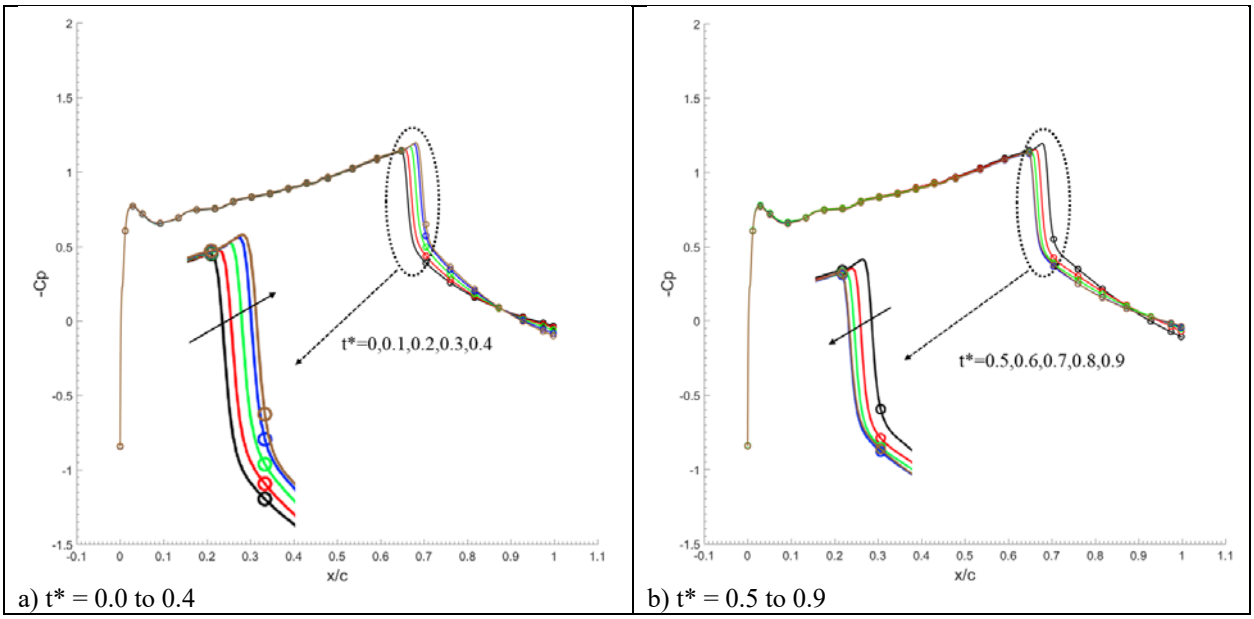

a) t* = 0.0 to 0.4 b) t* = 0.5 to 0.9

Figure 3.33 Pressure coefficient distribution on the upper surface at M = 0.8, α = 1 deg and h/c = 0.2 in one period.

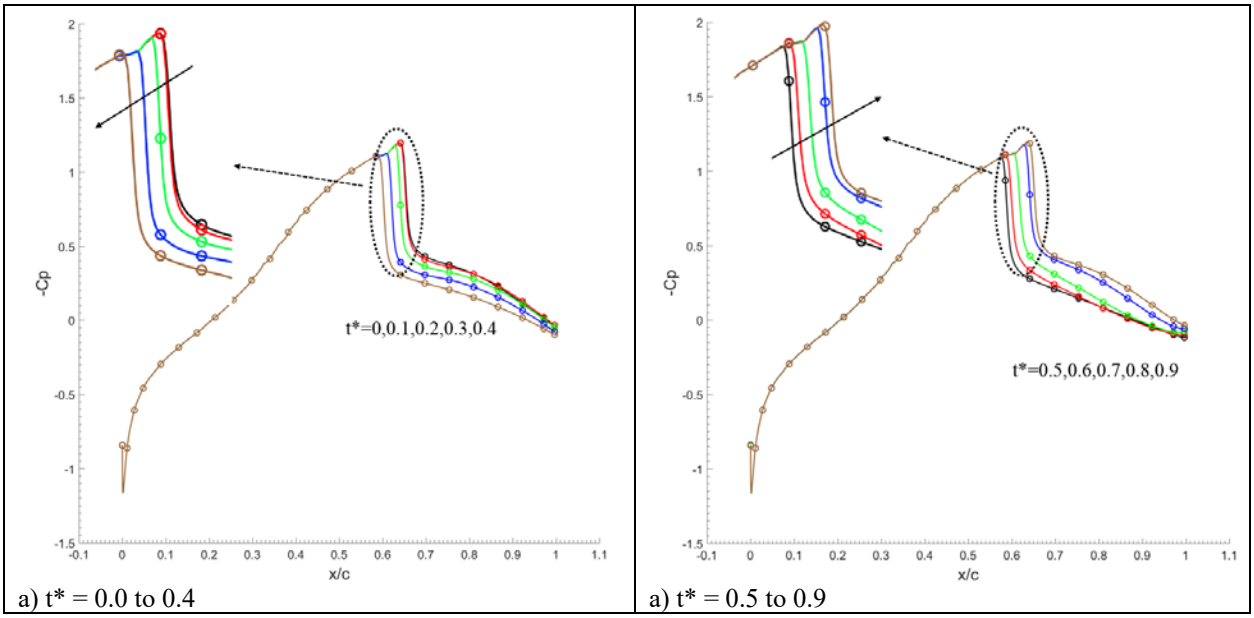

a) t* = 0.0 to 0.4 a) t* = 0.5 to 0.9

Figure 3.34 Pressure coefficient distribution on the lower surface at M = 0.8, α = 1 deg and h/c = 0.2 in one period.

From Figure 3.35 and 3.36, it can be seen that the lower surface shock is associated with boundary layer separation with a phase shift. From t* = 0 to 0.5, with the lower surface shock moving forward, the separation region changes from having the largest separation bubble to gradually shrinking in size. From t* = 0.6 to 1, the lower surface shock moves backward, and the separation region increases size with a lag in phase. The mechanism of the lower surface shock buffet is similar to the mechanism discussed before.

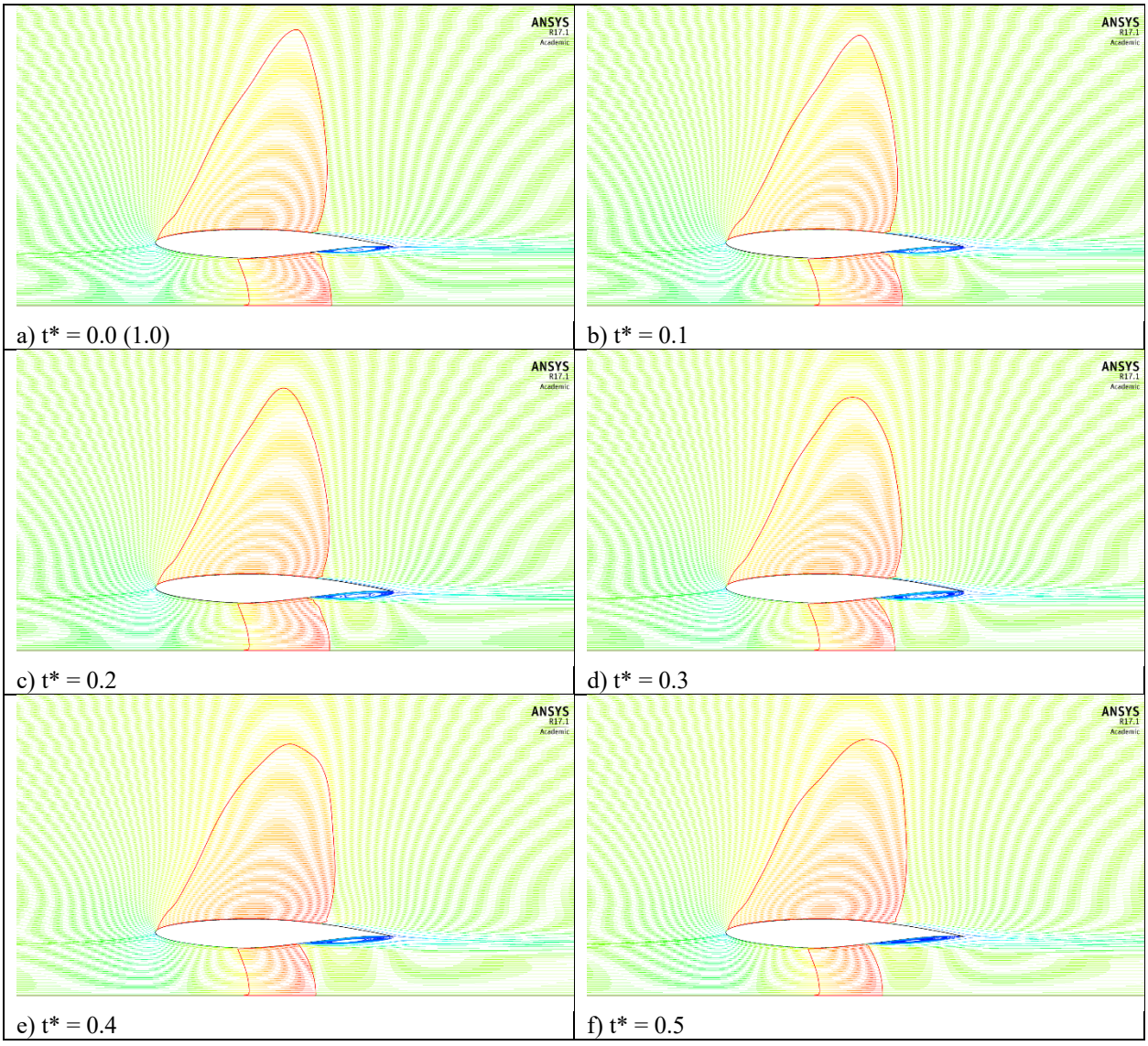

a) t* = 0.0 (1.0)

b) t* = 0.1

c) t* = 0.2

d) t* = 0.3

e) t* = 0.4

f) t* = 0.5

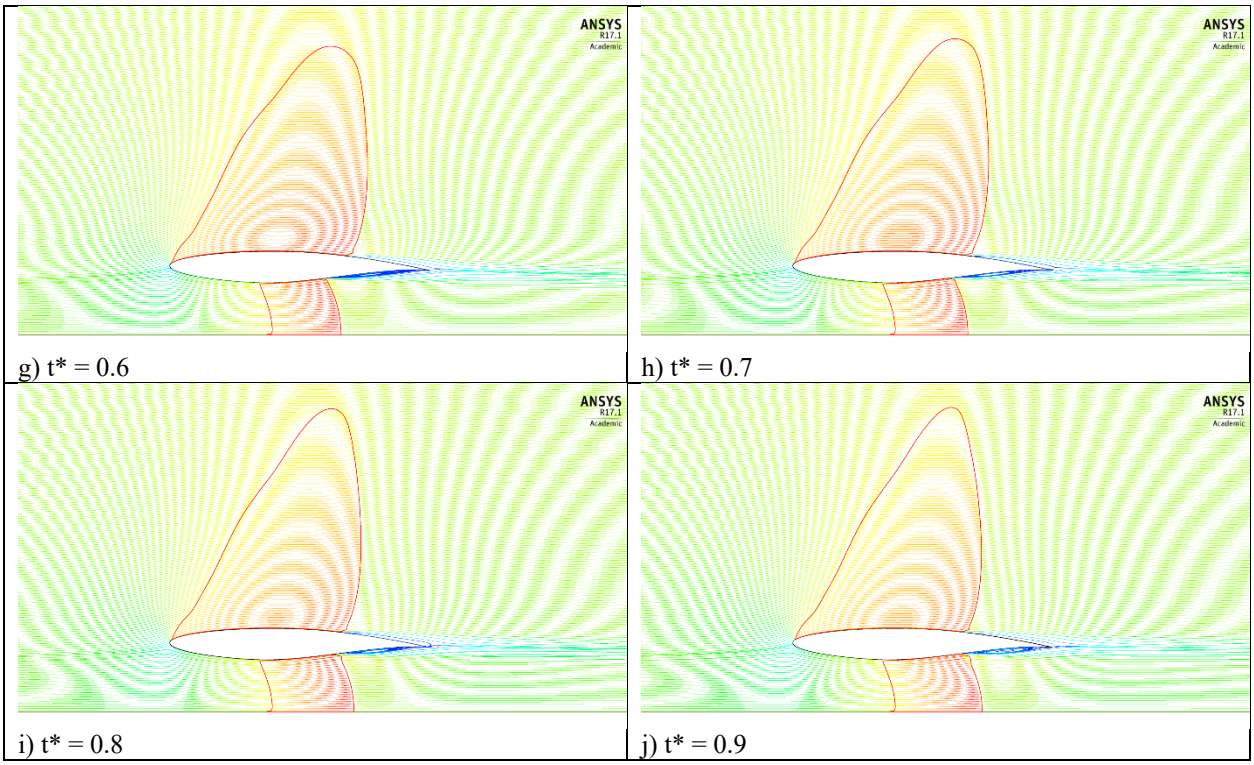

g) t* = 0.6 h) t* = 0.7

i) t* = 0.8 j) t* = 0.9

Figure 3.35 Streamlines and sonic line at M = 0.8, α = 1 deg and h/c = 0.2 in one period.

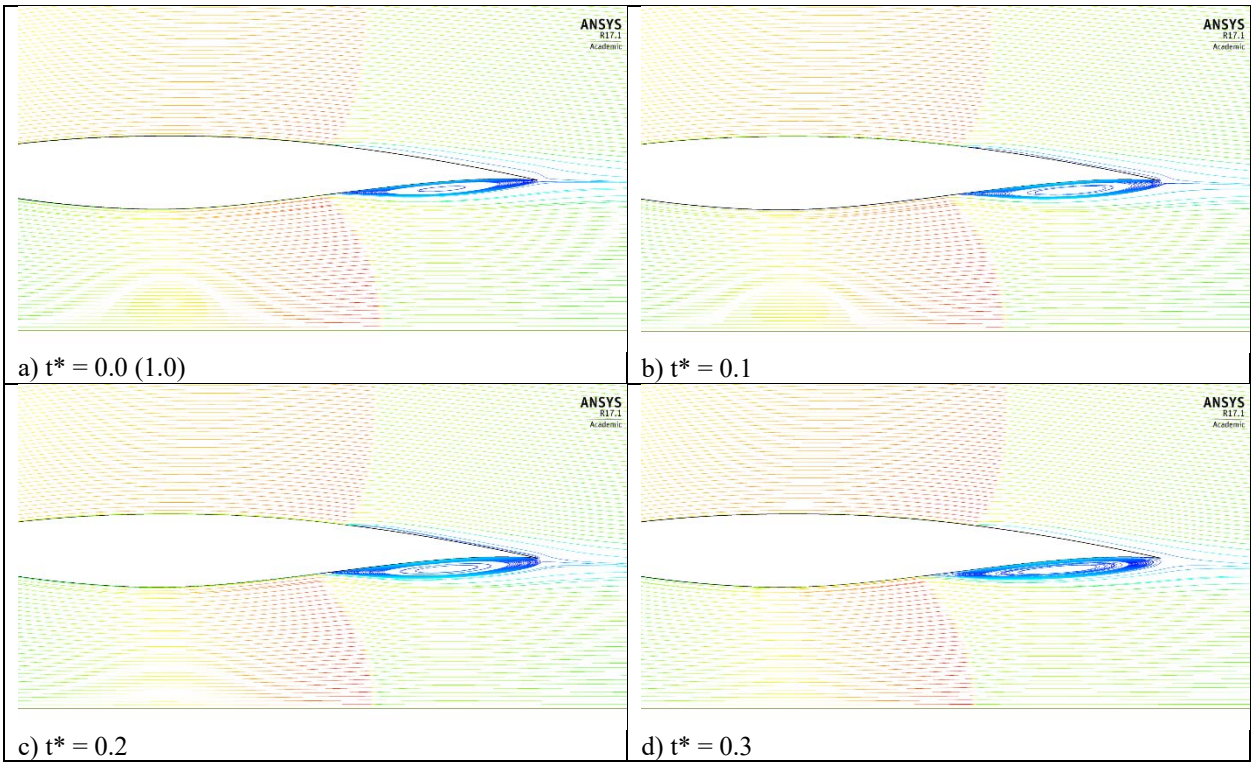

a) t* = 0.0 (1.0) b) t* = 0.1

c) t* = 0.2 d) t* = 0.3

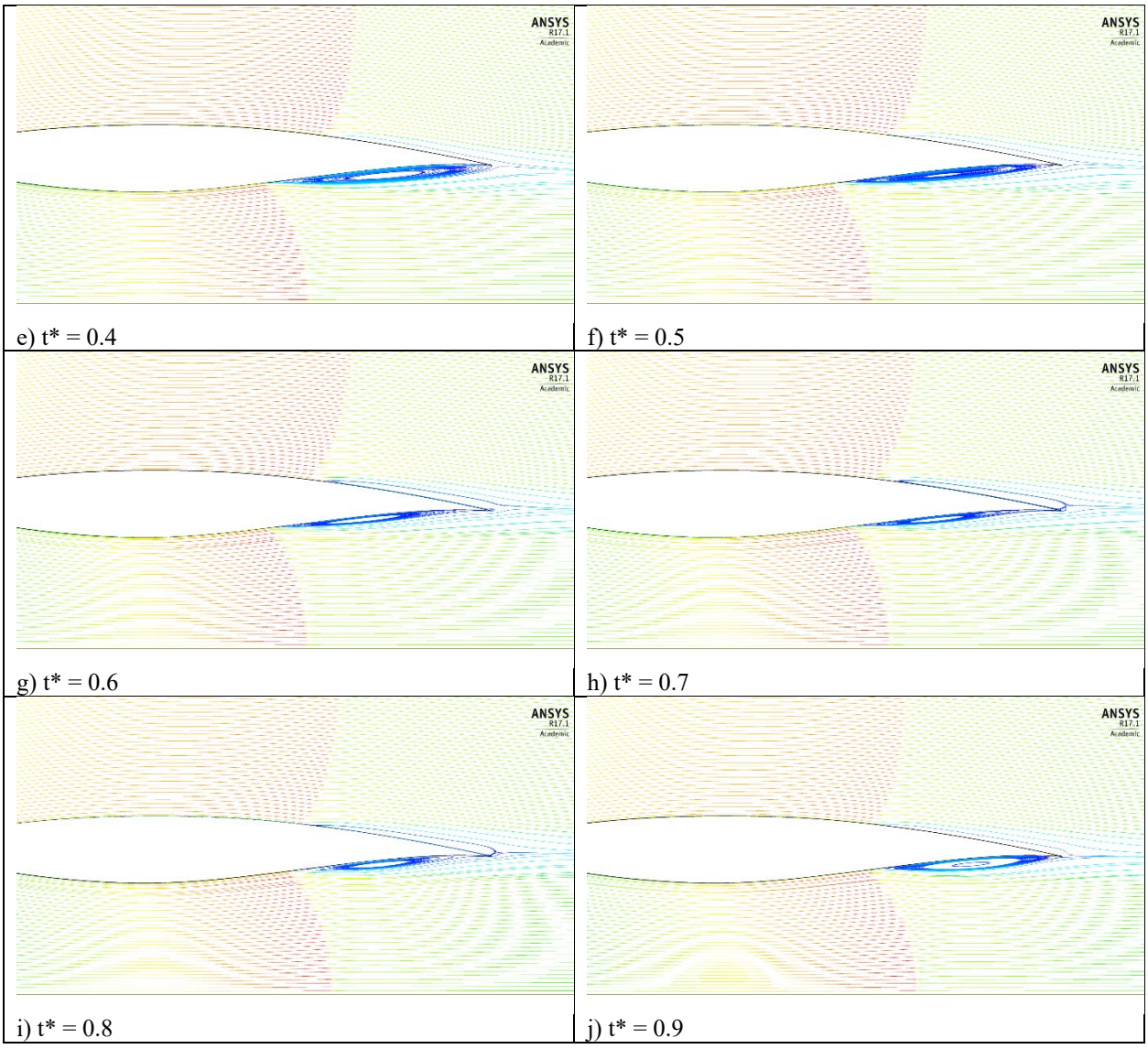

e) t* = 0.4 f) t* = 0.5

g) t* = 0.6 h) t* = 0.7

i) t* = 0.8 j) t* = 0.9

Figure 3.36 Enlarged streamlines near the trailing edge at M = 0.8, α = 1 deg and h/c = 0.2 in one period.

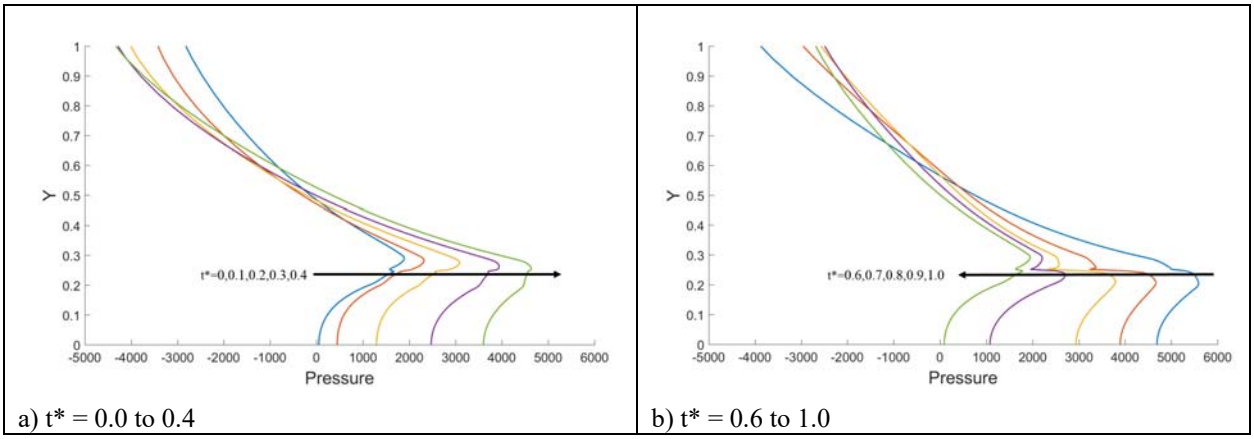

a) t* = 0.0 to 0.4 b) t* = 0.6 to 1.0

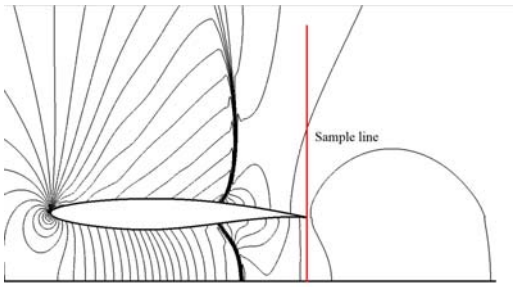

c) Sample line of the pressure divergence at the trailing edge

Figure 3.37 Pressure divergence at the trailing edge at M = 0.8, α = 1 deg and h/c = 0.2 in one period.

The pressure at the trailing edge is shown in Figure 3.37. The movement of the lower surface shock creates a large pressure oscillation at the exit of the channel formed by the ground and the airfoil. From t* = 0 to 0.5, with the lower surface shock moving forward, the pressure at the exit of the channel increases, corresponding to the converging-diverging nozzle theory. To satisfy the Unsteady-Kutta condition, the pressure above the trailing edge changes accordingly. The pressure waves transmitted upstream cause the upper surface shock to move resulting in a mild boundary layer separation.

Chapter 4: Wavy Ground

In most flight conditions, a WIG aircraft usually flies above water in order to avoid obstacles. The water surface in general is wavy with waves of different amplitudes. When the WIG aircraft is very close to the ground, any variation in its lift coefficient can affect its performance and maneuverability. In the transonic regime, the decrease in ground clearance causes a shock to occur on the lower surface. The variation in the ground clearance due to the wavy surface can cause the flow beneath the aircraft to have a periodic behavior.

4.1 Mesh Topology and Mesh Generation

For the wavy ground, shown in Figure 4.1, the entire domain is separated into two domains; while the upper domain contains the airfoil and remains stationary in the simulation, while the lower domain contains the wavy ground and moves with the same velocity as the incoming freestream. Two domains are separated by a straight line which allows the sliding mesh technique to be employed. The topology of the mesh is similar to the mesh in case of flat ground described before. As shown in Figure 4.2, an H-type block mesh is used in the upper domain and an orthogonal mesh is used in the lower domain.

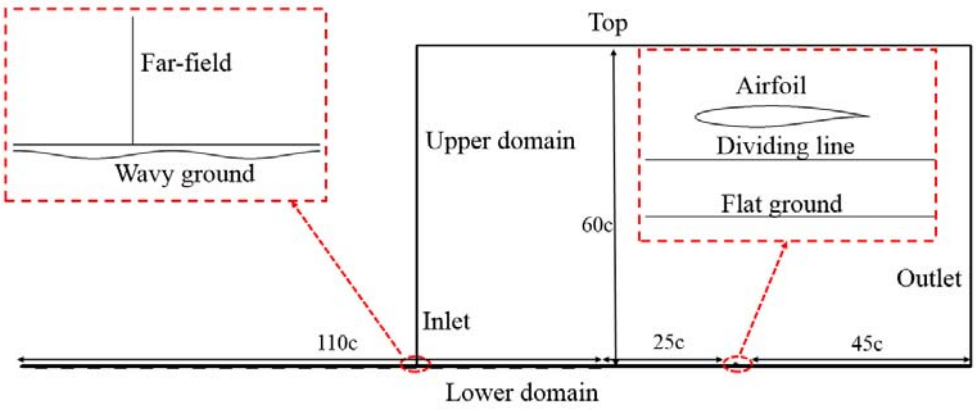

Figure 4.1 Computational domain for simulations with wavy ground.

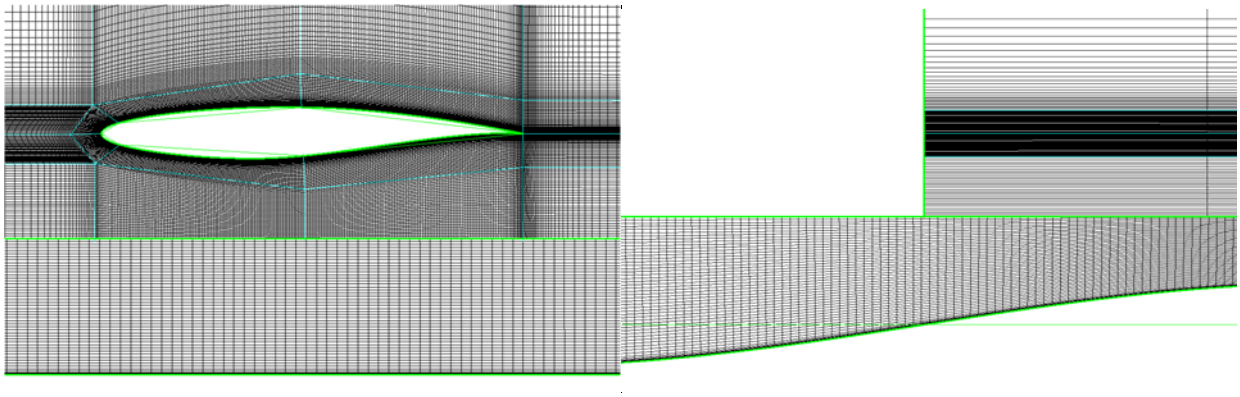

Figure 4.2 Mesh layout above the wavy ground.

4.2 Numerical Method

The upper domain in Figure 4.2 resembles the mesh for the flat ground case. A rectangular computational domain is employed as shown in Figure 4.2. A structured mesh with refinement in the wake region, and between the airfoil and the ground is also shown in Figure 4.2. The inlet and the top boundaries of the upper domain are located 60c away from the airfoil, the outlet boundary is 45c away, and the dividing line boundary is determined by the ground clearance. For the inlet, outlet and top boundaries, pressure far-field boundary condition is employed which specifies the two Riemann invariants for a flow normal to the boundary. For the dividing line, an interface boundary condition is employed which allows the solver to treat it as an interior boundary.

For the lower domain, the wavy ground is located 25c ahead of the airfoil, the wavy ground itself has a length of 110c. The wavy ground can be expressed by the formula given below.

$$y = h + a\cos\left(\frac{2\pi}{\lambda}(x - x_0)\right)$$

The wavy ground used in this simulation has an oscillation amplitude of $a = 0.125m$ and a period $\lambda = 5m$. Two ground clearances of h/c = 0.5 and 1.0 are considered. Unlike the case of airfoil in flat ground effect where the ground has a translational velocity equal to the incoming freestream.

In case of wavy ground effect, the entire lower domain moves at the same speed as the freestream while the ground is stationary with respect to the lower domain.

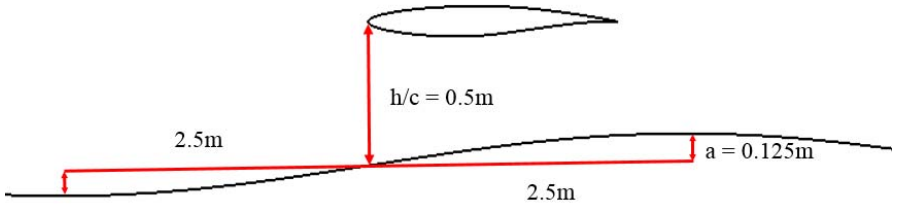

Figure 4.3 Schematic of the wavy ground during one period.

The double precision solver in ANSYS FLUENT 17.1 is used to perform the CFD simulations. Compressible Reynolds-averaged Navier-Stokes equations with Spalart-Allmaras turbulence model are solved. Second-order numerical scheme is used for both the convection and diffusion terms. The pressure-coupled transient solver is used for pressure-velocity coupling. Transient solver is employed in the simulations. The time step used is T/200, where T denotes the time period of the wavy ground which varies with the free stream Mach number. The transient solution is considered converged when the aerodynamic coefficients become periodic after several cycles and do not change from one cycle to next.

Chapter 5: Results and Discussion

5.1 Lift and Drag for Various M, α and h/c

The simulations begin with a uniform velocity field to initialize the flow field. The flat ground of 25c ahead of the airfoil is used to achieve a more steady initial condition before the wavy ground. A typical convergence history of the simulation is shown in Figure 5.1, the lift coefficient shows a periodic behavior after a few seconds of flow time.

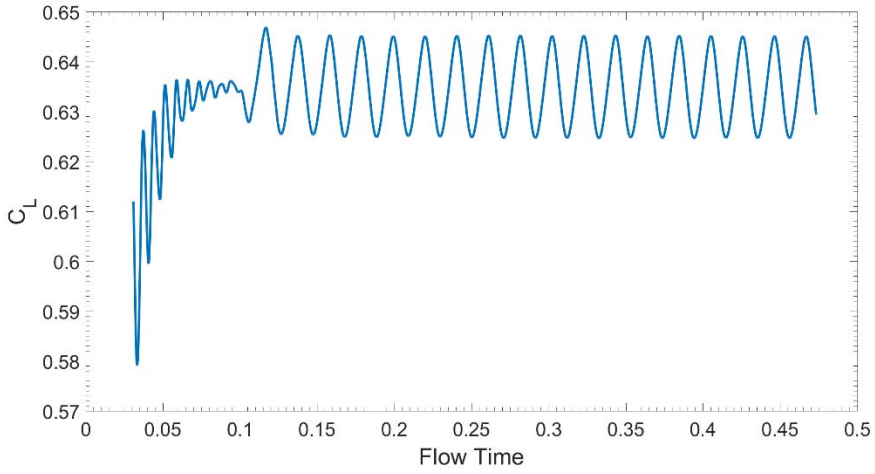

Figure 5.1 C_L history for the case at M = 0.7, α = 2 deg and h/c = 1.0.

Figures 5.2 - 5.7 show the time-averaged results for all the wavy ground cases. From M = 0.5 to 0.7, the lift coefficient increases with the Mach number except at M = 0.8 and at $\alpha = 4$ deg, the lift has a sharp drop which will be discussed later. As the ground clearance decreases from h/c = 1.0 to 0.5, the lift increases slightly at $\alpha = 2$ and 4 deg. The drag coefficient of the airfoil increases dramatically when Mach number increases to 0.8, the wave drag associated with shock is the main reason for the drag crisis.

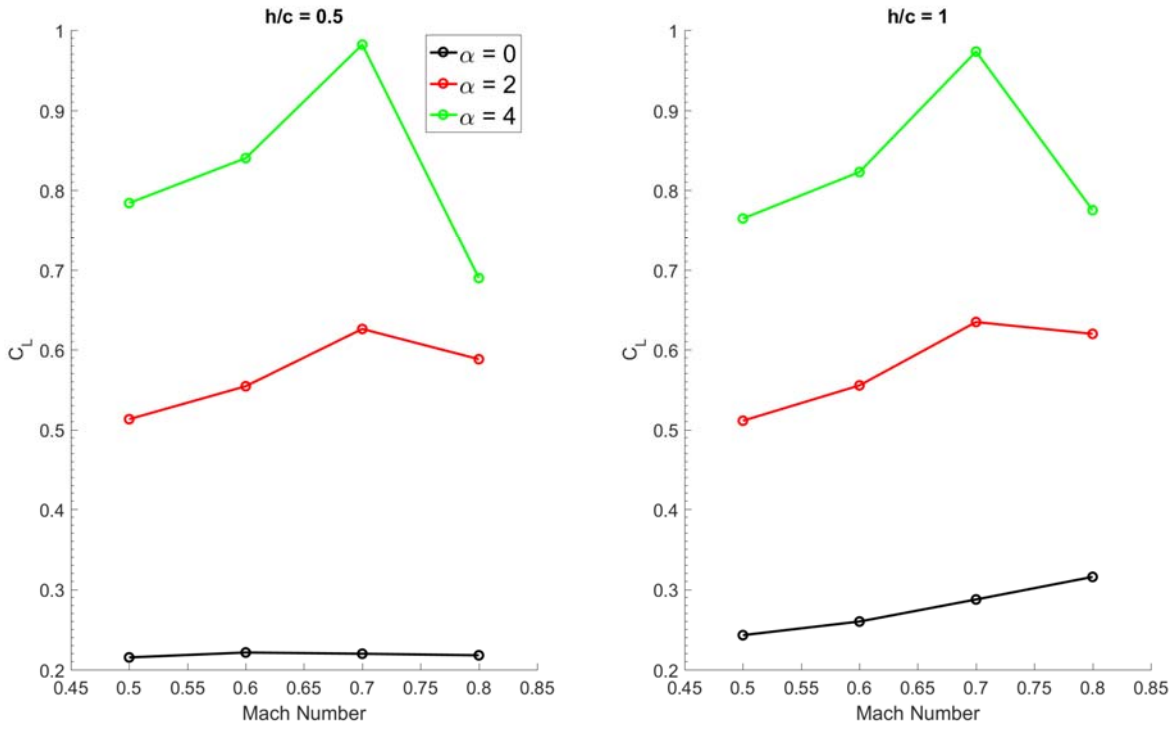

Figure 5.2 Variation in C_L with ground clearance at various α and M.

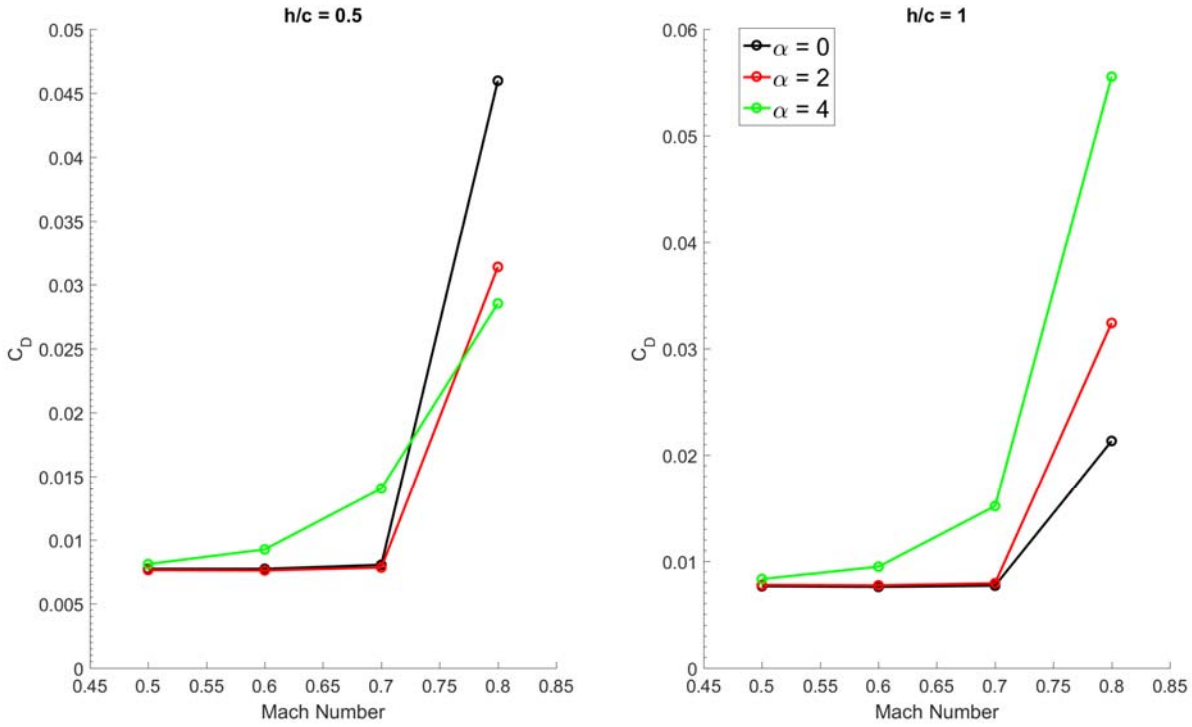

Figure 5.3 Variation in C_D with ground clearance at various α and M.

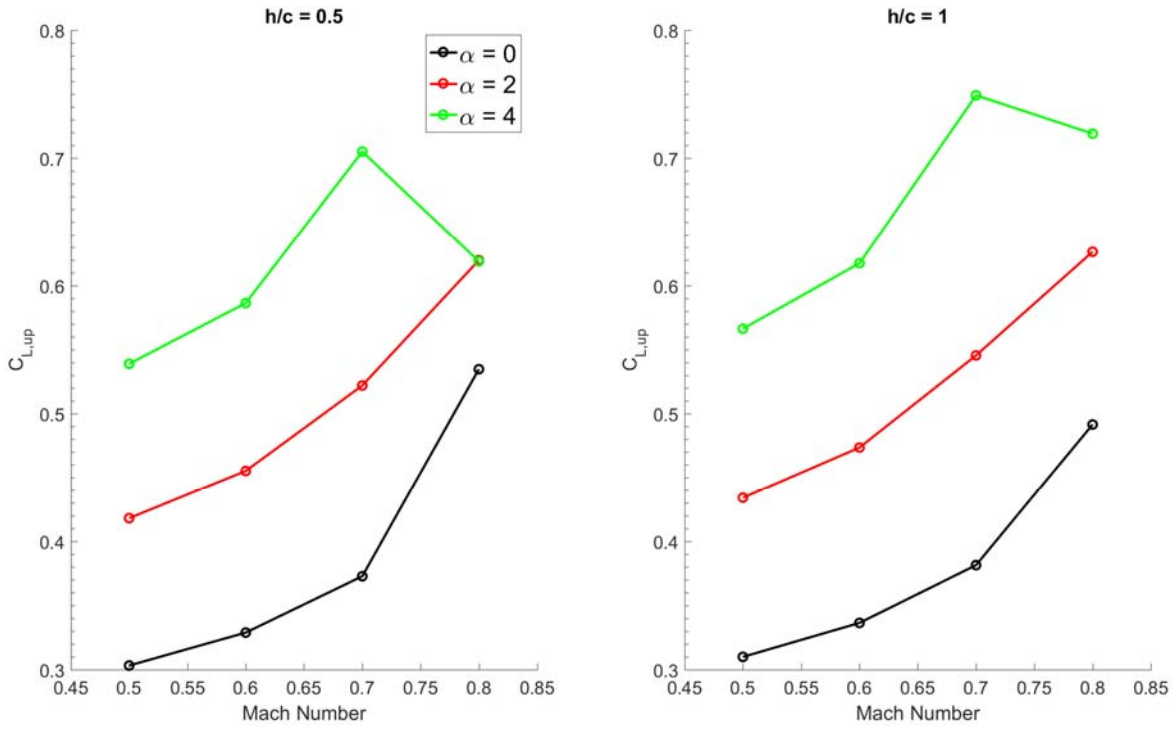

Figure 5.4 Variation in $C_{L,up}$ with ground clearance at various α and M.

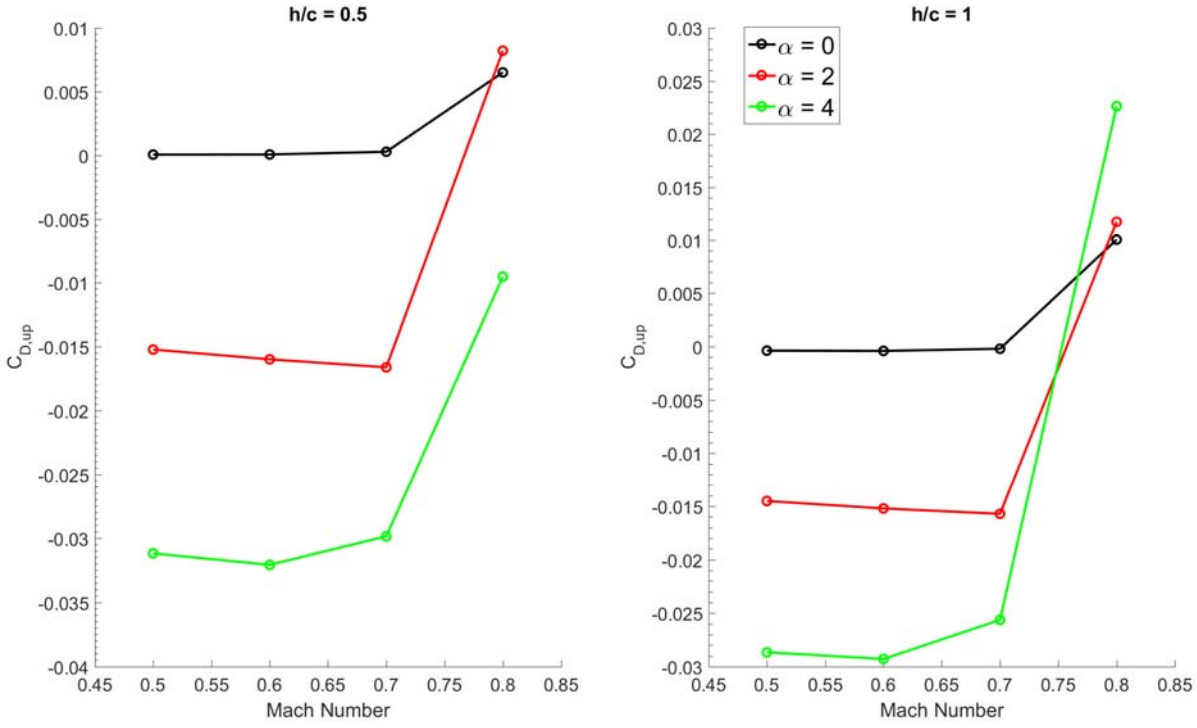

Figure 5.5 Variation in $C_{D,up}$ with ground clearance at various α and M.

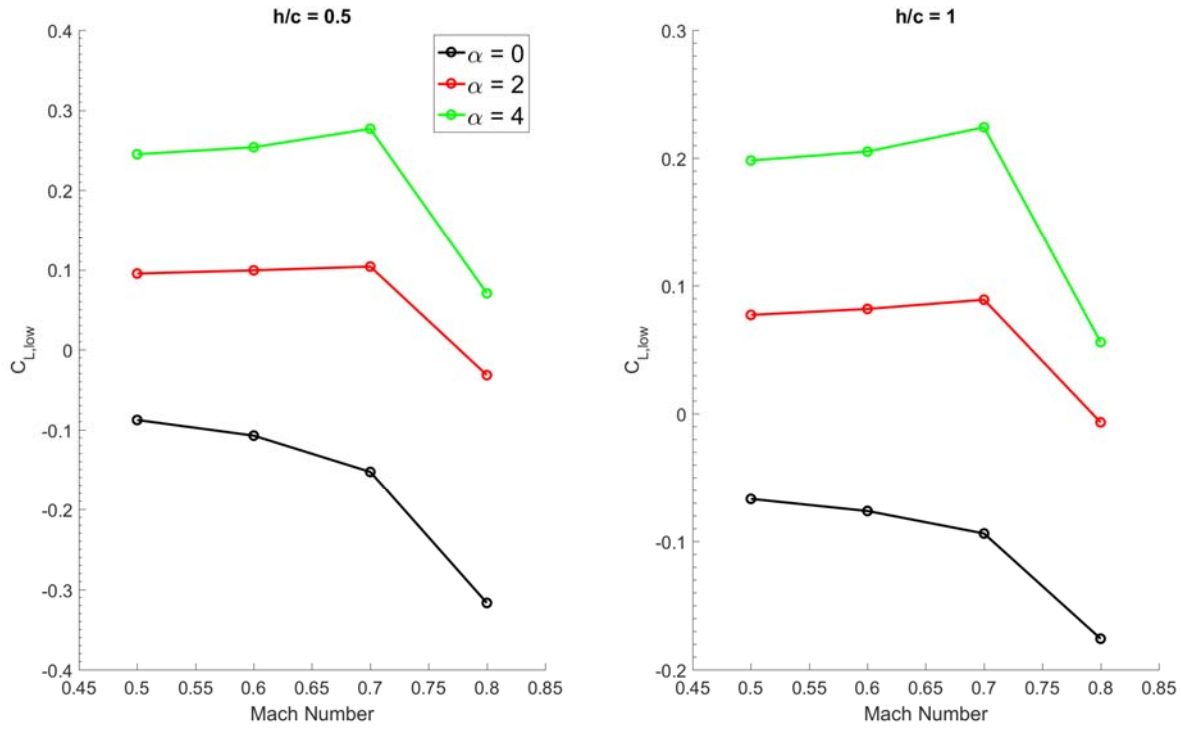

Figure 5.6 Variation in $C_{L,down}$ with ground clearance at various α and M.

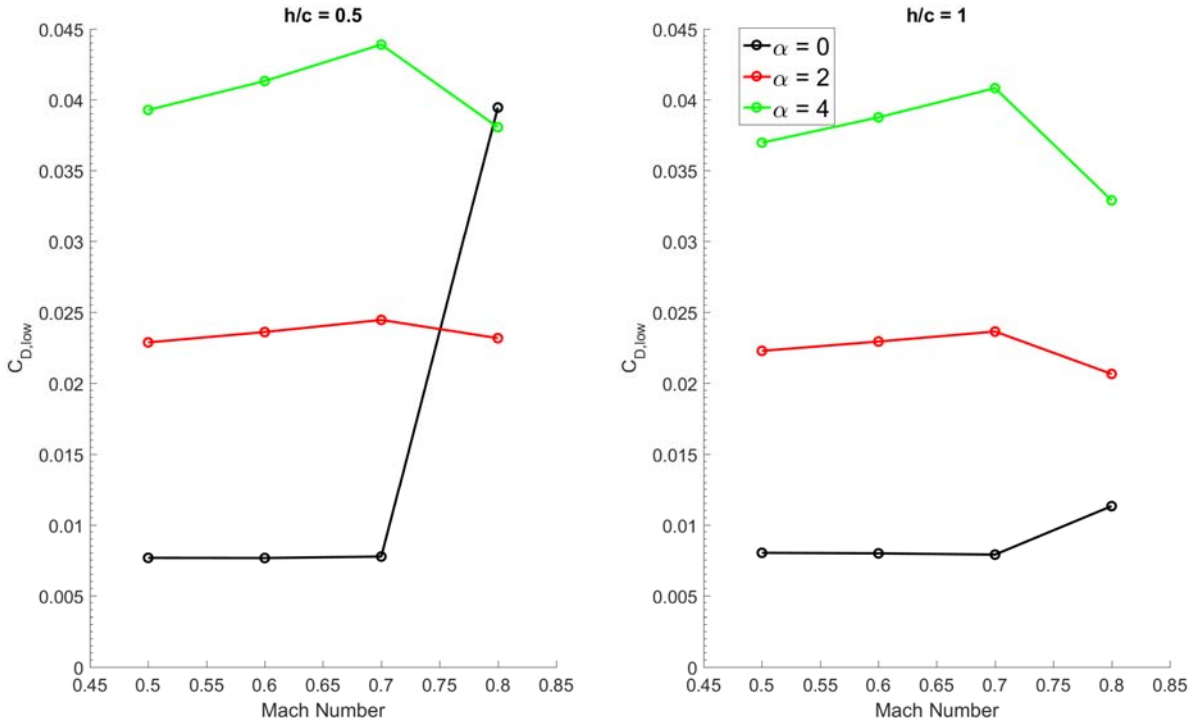

Figure 5.7 Variation in $C_{D,down}$ with ground clearance at various α and M.

5.1.1 High Ground Clearance

The definition of high ground clearance is the same as in the flat ground case described before, when there is only an upper surface shock or no shock at all. Two typical cases of $\alpha = 0$ deg, M = 0.7 and h/c = 0.5 and 1.0 are analyzed. These cases do not have shock on either surface. The period start from the position shown in Figure 4.3. The leading edge of the airfoil is vertically aligned with the middle section of one period of the wavy ground, and the ground clearance begins to increase at the beginning of the period.

The lift and drag coefficient history in one period for two ground clearances is shown in Figure 5.8. The ground is shown in dotted line. The lift and drag coefficient clearly have phase difference with the variation in ground clearance. The lift coefficient for h/c = 1.0 case has a 35 degree phase lead and the h/c = 0.5 case has a 61 degree phase lead.

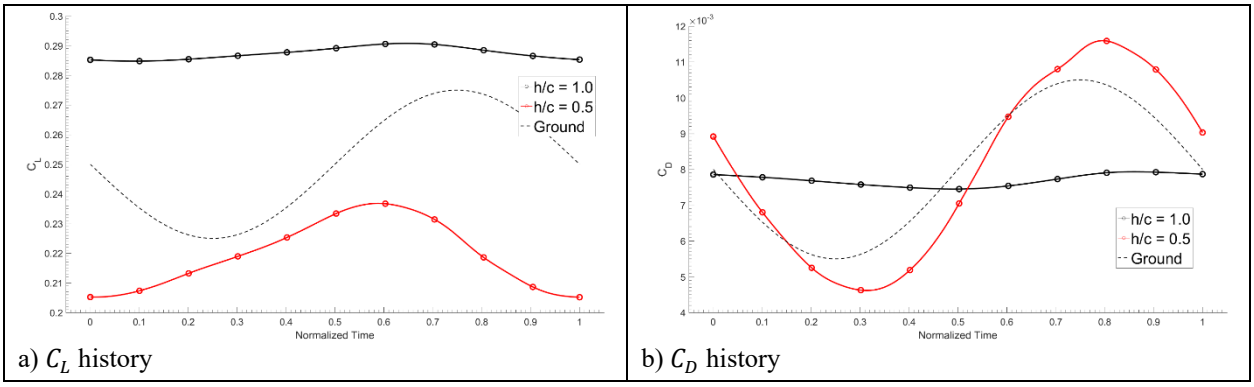

a) C_L history b) C_D history

Figure 5.8 C_L and C_D variation for the RAE2822 airfoil at M = 0.7 and α = 0 deg in the presence of wavy ground.

The wave amplitude is a constant which suggests that the lower the ground clearance, the relative oscillation amplitude is larger. The lift and drag coefficient in one period show that the h/c = 0.5 case has more oscillations. The lift variation at h/c = 1.0 is only 1.04% while at h/c = 0.5 it is 7.2%.

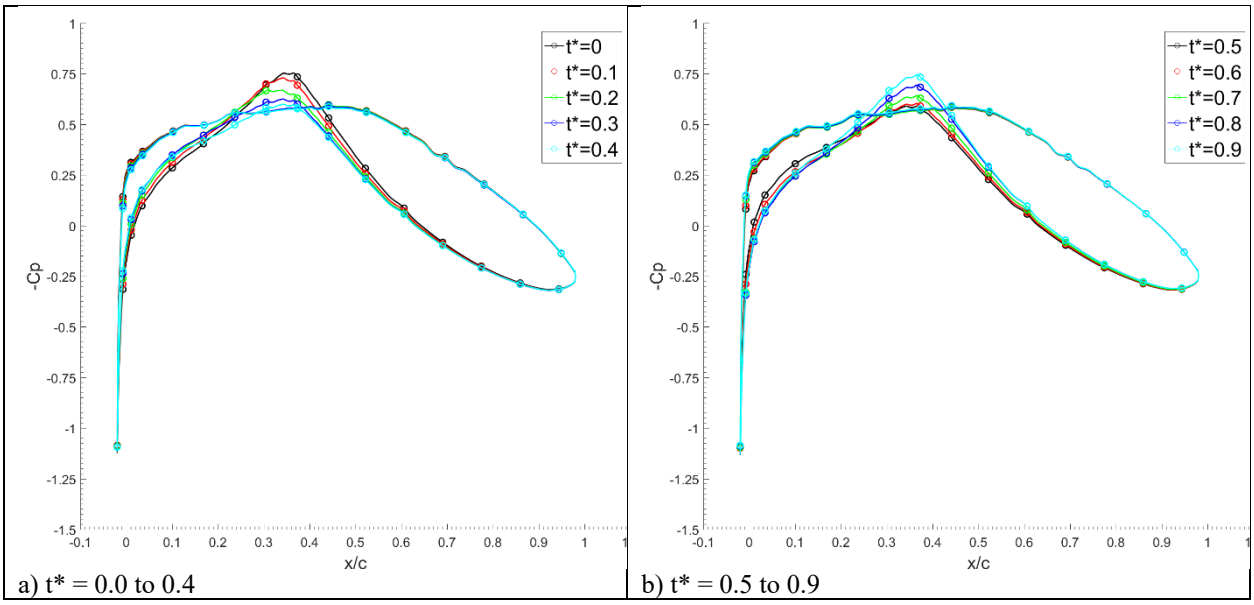

a) t* = 0.0 to 0.4 b) t* = 0.5 to 0.9

Figure 5.9 Pressure coefficient distribution on the RAE2822 airfoil at M = 0.7, α = 0 deg and h/c = 0.5.

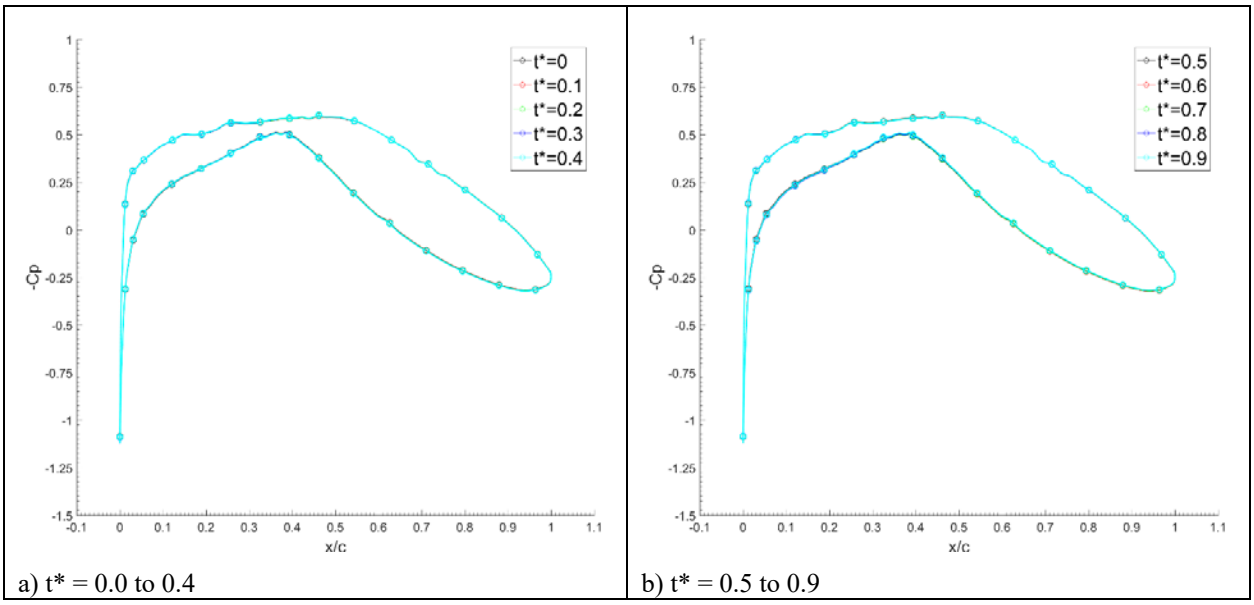

a) t* = 0.0 to 0.4 b) t* = 0.5 to 0.9

Figure 5.10 Pressure coefficient distribution on the RAE2822 airfoil at M = 0.7, α = 0 deg and h/c = 1.0.

The pressure coefficient plot in Figure 5.9 shows that the difference in lift is mainly caused by the lower surface in h/c = 0.5 case; while from t* = 0 to 0.4, the lower surface pressure increases, causing the lower surface lift coefficient to increase slightly. The pressure coefficient for the h/c = 1.0 case in Figure 5.10 shows almost no change in one period, which is consistent with the very small variation in lift in Figure 5.8. The flow fields for the two cases show corresponding behavior

where the pressure contours for h/c = 1.0 case change less dramatically compared to that for h/c = 0.5 case.

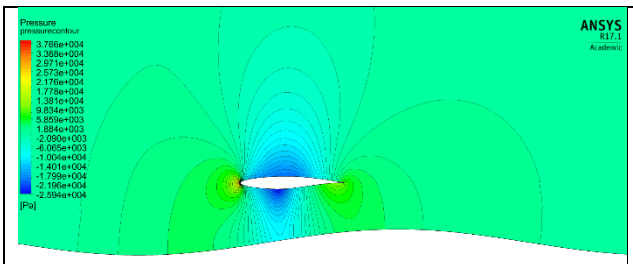

a) t* = 0.0 (1.0)

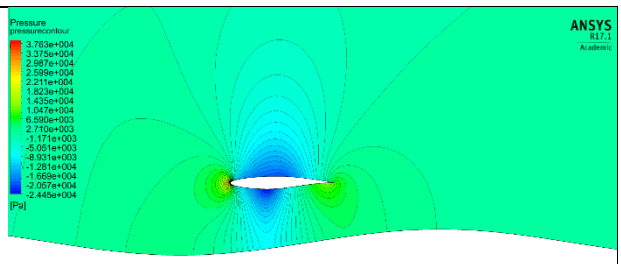

b) t* = 0.1

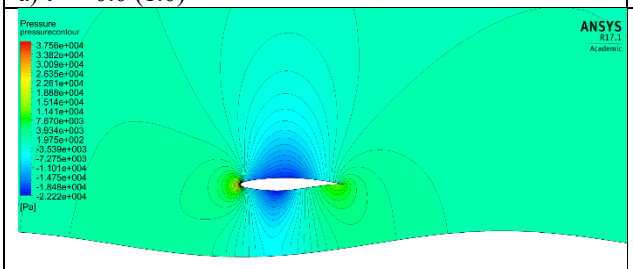

c) t* = 0.2

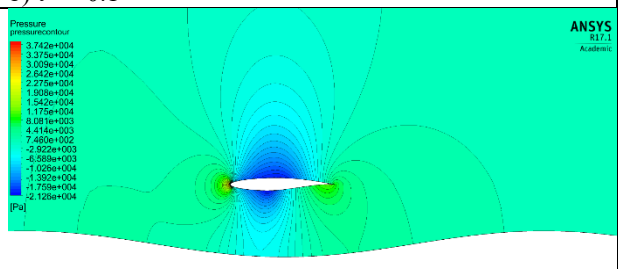

d) t* = 0.3

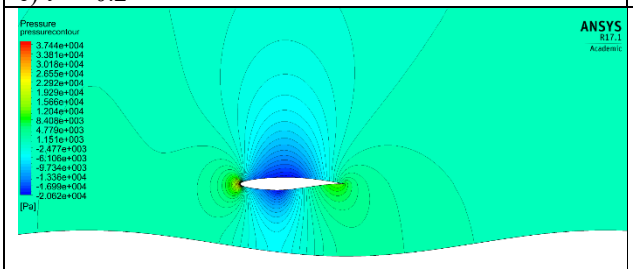

e) t* = 0.4

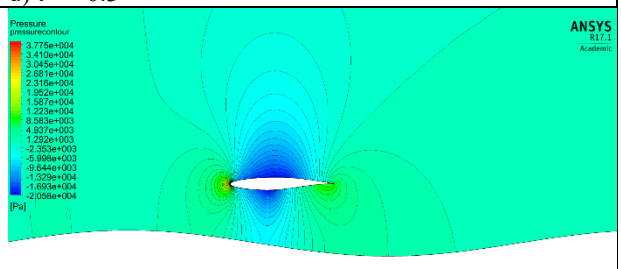

f) t* = 0.5

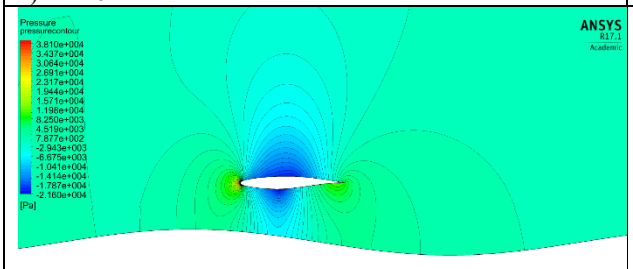

g) t* = 0.6

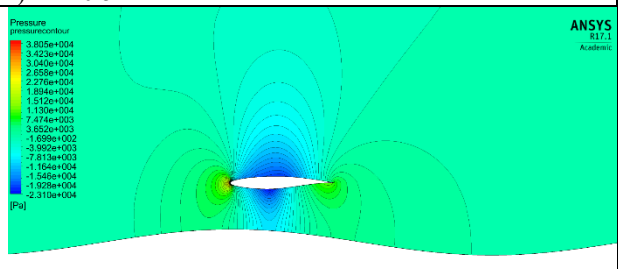

h) t* = 0.7

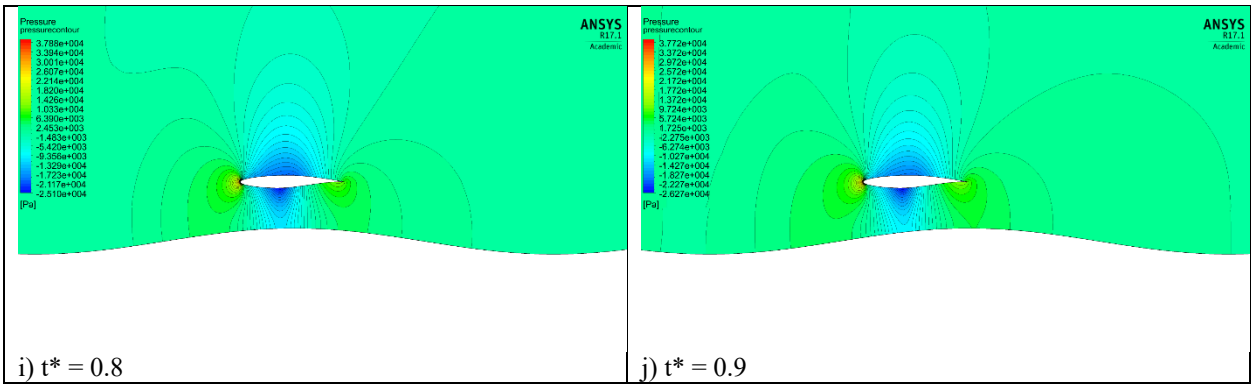

i) t* = 0.8 j) t* = 0.9

Figure 5.11 Pressure contours of the RAE2822 airfoil at M = 0.7, α = 0 deg and h/c = 0.5 above the wavy ground.

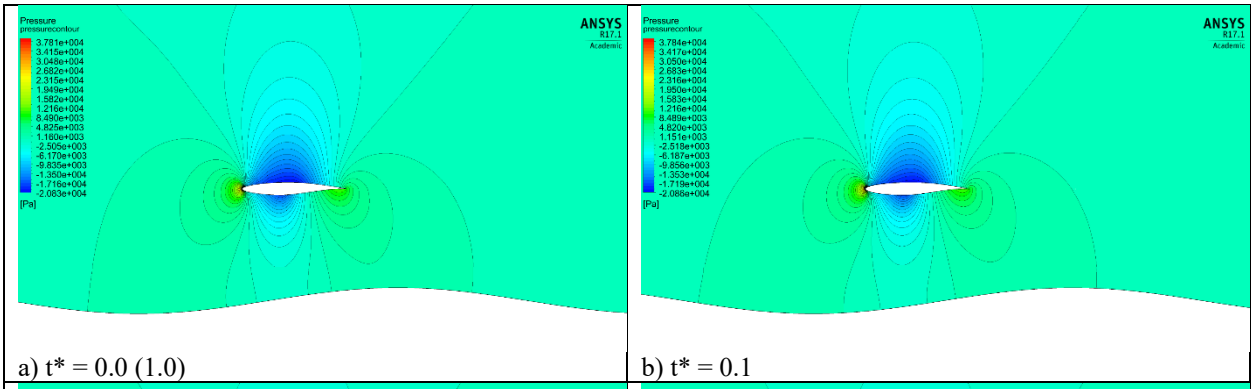

a) t* = 0.0 (1.0) b) t* = 0.1

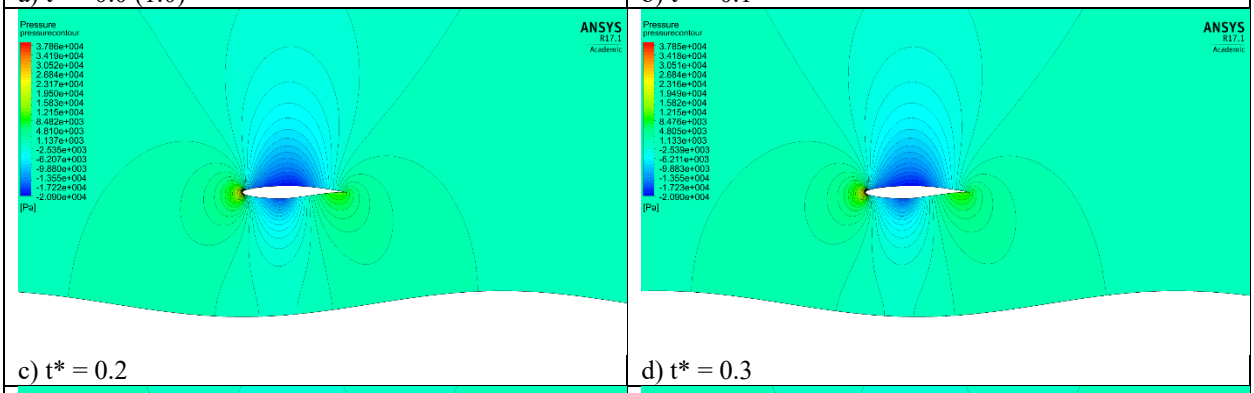

c) t* = 0.2 d) t* = 0.3

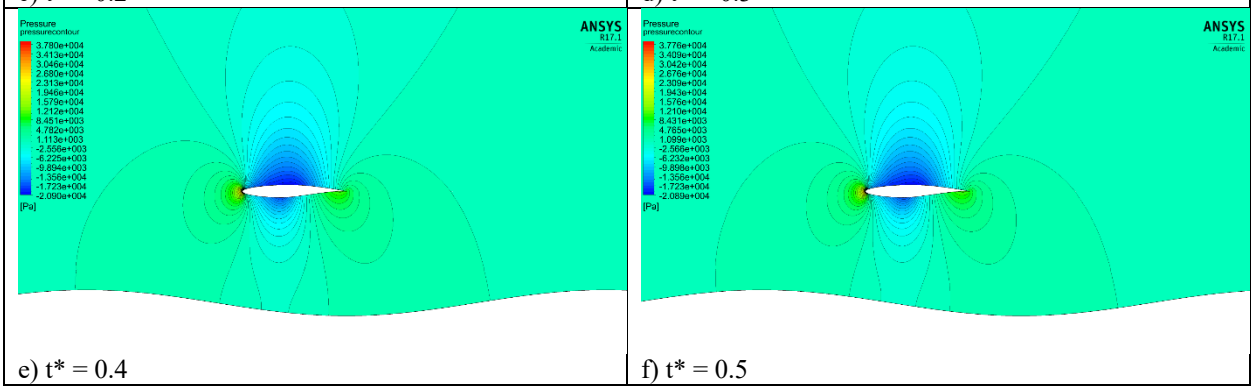

e) t* = 0.4 f) t* = 0.5

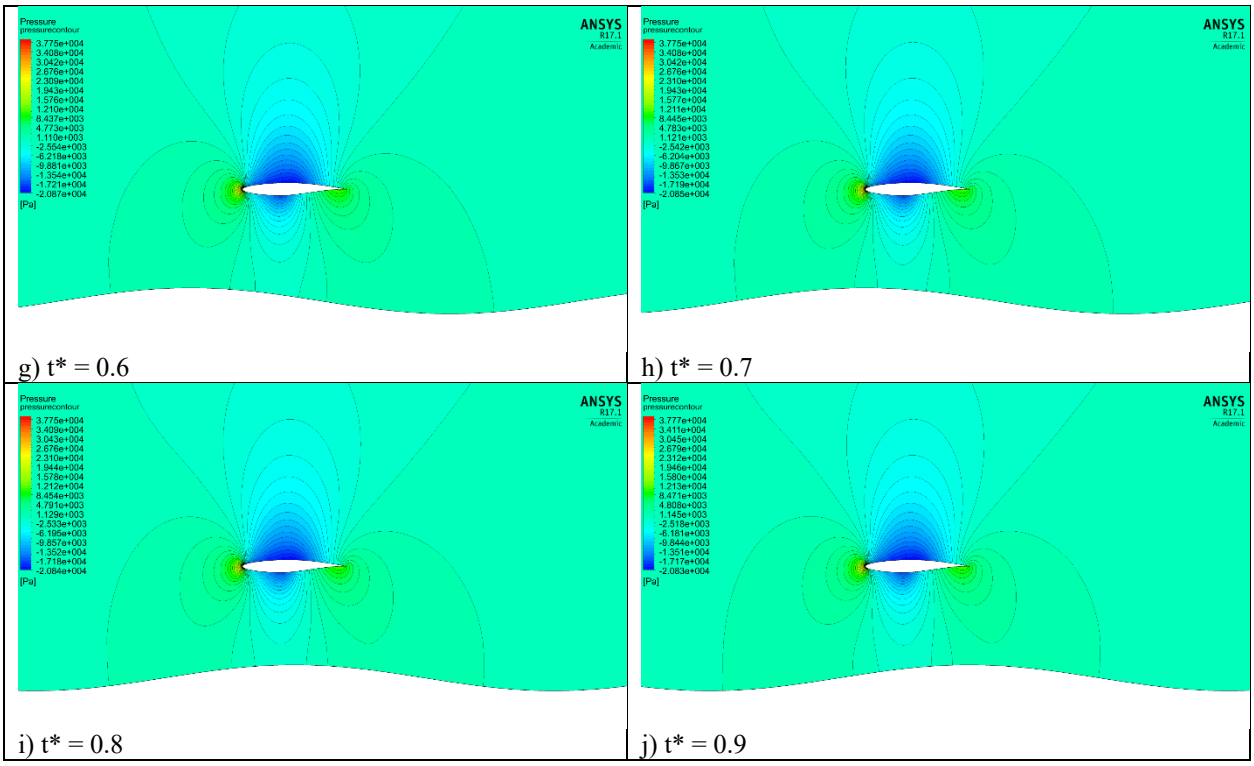

Figure 5.12 Pressure contours of the RAE2822 airfoil at M = 0.7, α = 0 deg and h/c = 1.0 above the wavy ground.

5.1.2 Low Ground Clearance

When the Mach number become sufficiently high or the ground clearance become low enough, a lower surface shock appears. When the lower surface shock appears, it significantly increases the wave drag while the lower surface shock changes its strength in one period. Two cases of $\alpha = 2$ deg, M = 0.8 and h/c = 0.5 and 1.0 are compared and analyzed. Another special case of $\alpha = 0$ deg, M = 0.8 and h/c = 0.5 is also discussed since the lower surface shock reaches the wavy ground in this case.

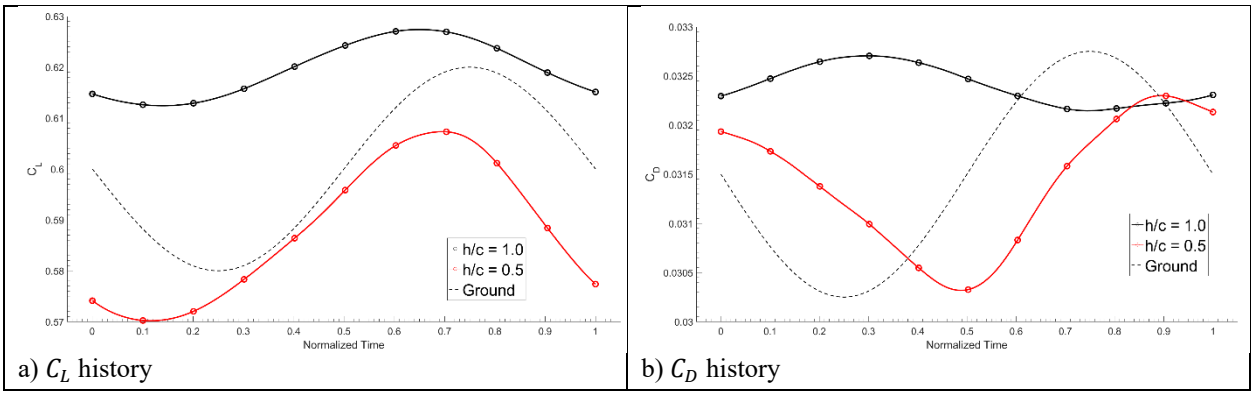

a) C_L history b) C_D history

Figure 5.13 C_L and C_D variation of the RAE2822 airfoil at M = 0.8 and α = 2 deg.

Similar to the high ground clearance case, h/c = 0.5 case shows more oscillations in lift compared to the h/c = 1.0 case as shown in Figure 5.13. The phase lead of the lift and drag compared to the wavy ground case also show the same trend. The pressure coefficient plot shown in Figure 5.14 shows that both cases have shock on the lower surface shock. The lift difference is caused mostly by the lower surface; in h/c = 0.5 case, the position of the lower surface shock does not change while the strength of the shock oscillates in one period causing the pressure behind the shock to vary.

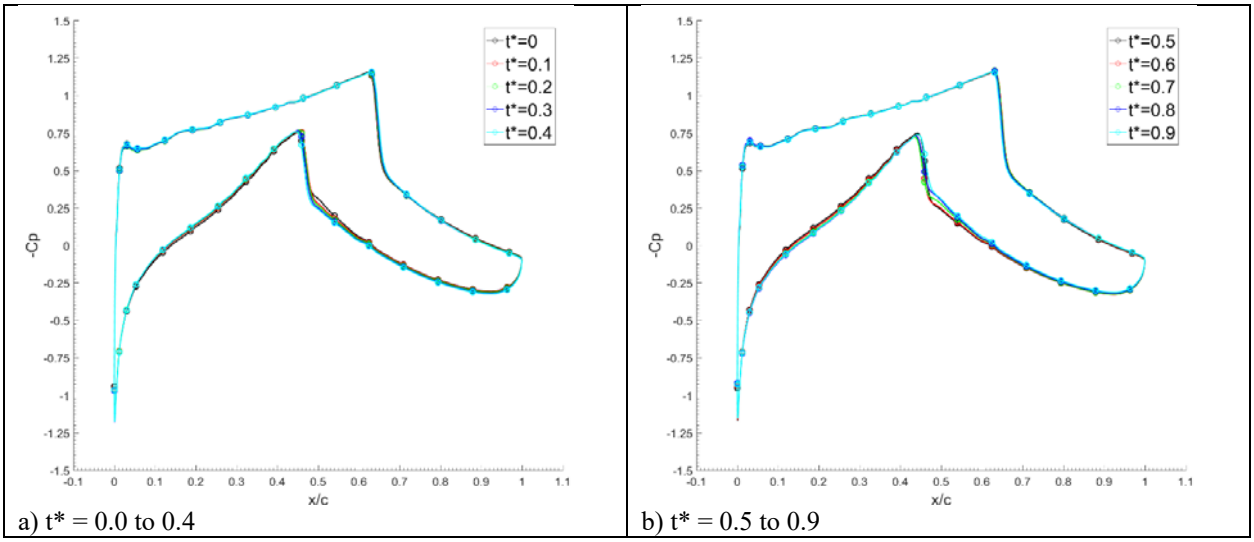

a) t* = 0.0 to 0.4 b) t* = 0.5 to 0.9

Figure 5.14 Pressure coefficient distribution on the RAE2822 airfoil at M = 0.8, α = 2 deg and h/c = 0.5.

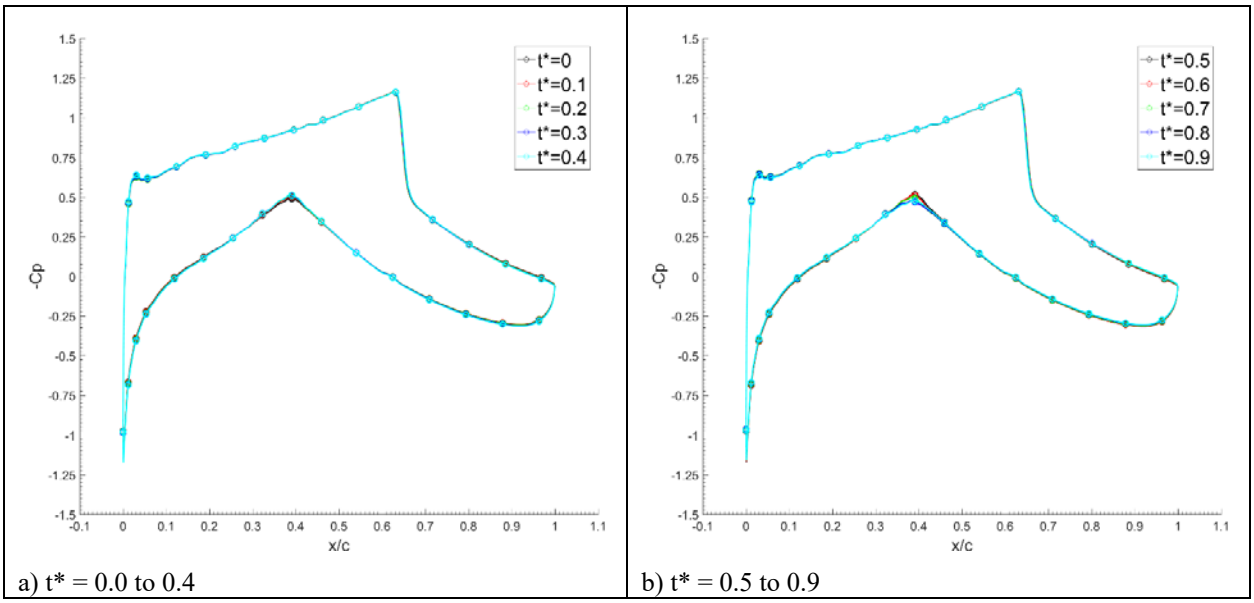

a) t* = 0.0 to 0.4 b) t* = 0.5 to 0.9

Figure 5.15 Pressure coefficient distribution on the RAE2822 airfoil at M = 0.8, α = 2 deg and h/c = 1.0.

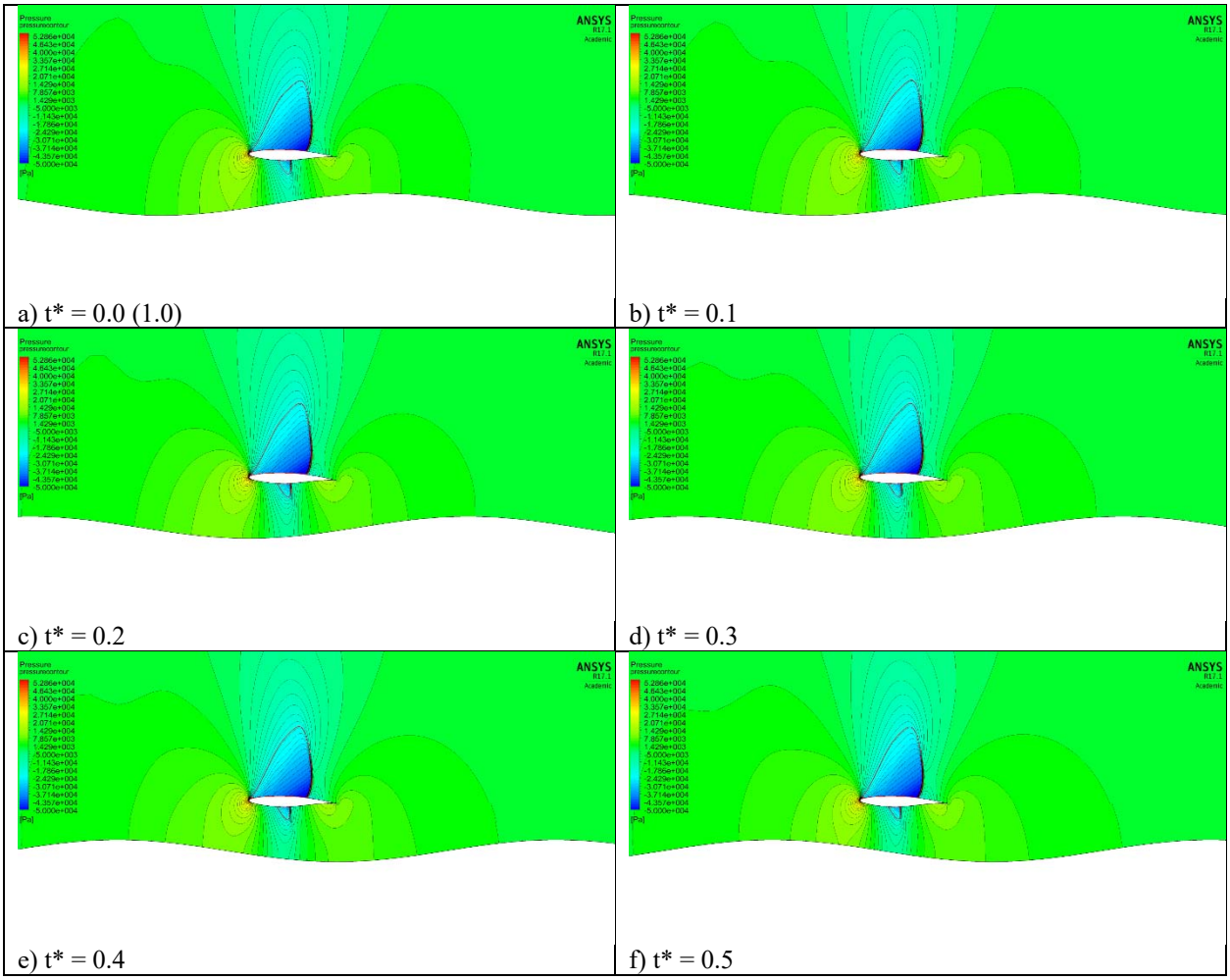

a) t* = 0.0 (1.0) b) t* = 0.1

c) t* = 0.2 d) t* = 0.3

e) t* = 0.4 f) t* = 0.5

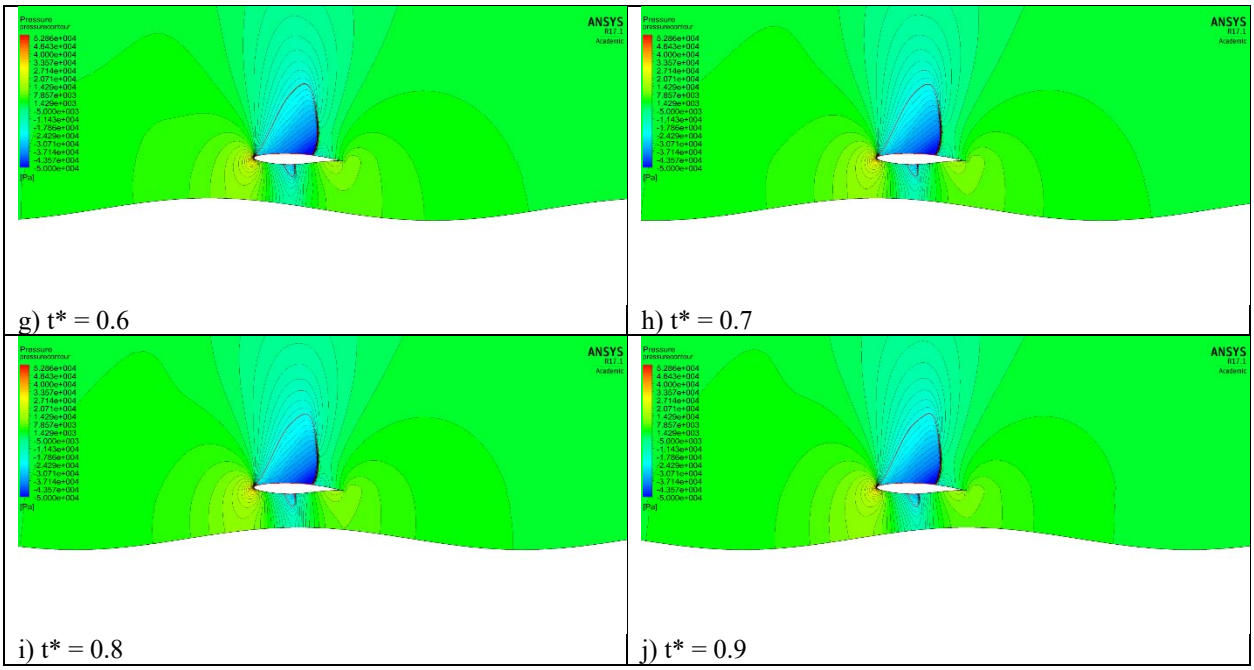

g) t* = 0.6 h) t* = 0.7

i) t* = 0.8 j) t* = 0.9

Figure 5.16 Pressure contours of the RAE2822 airfoil at M = 0.8, α = 2 deg and h/c = 0.5 above wavy ground.

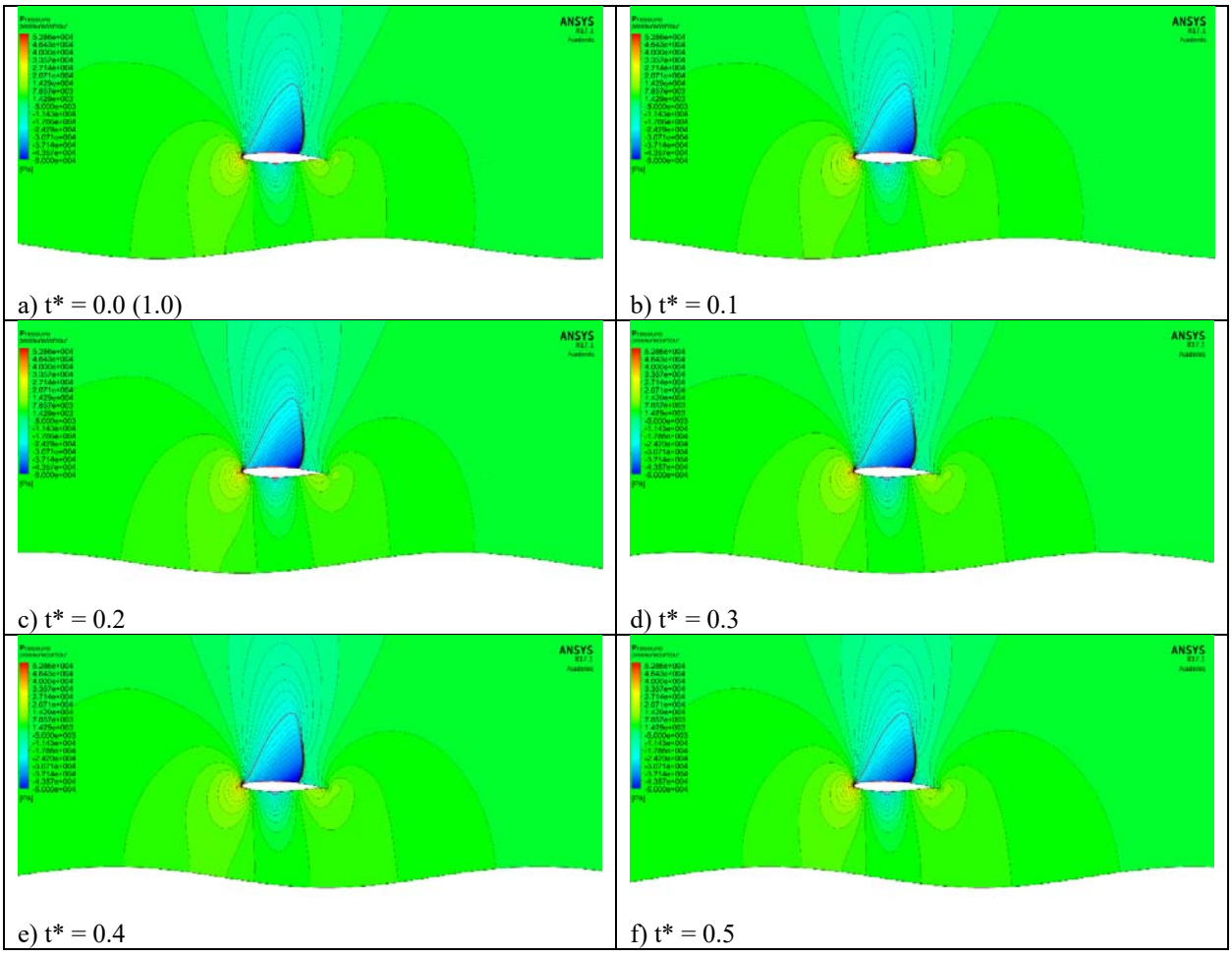

a) t* = 0.0 (1.0) b) t* = 0.1

c) t* = 0.2 d) t* = 0.3

e) t* = 0.4 f) t* = 0.5

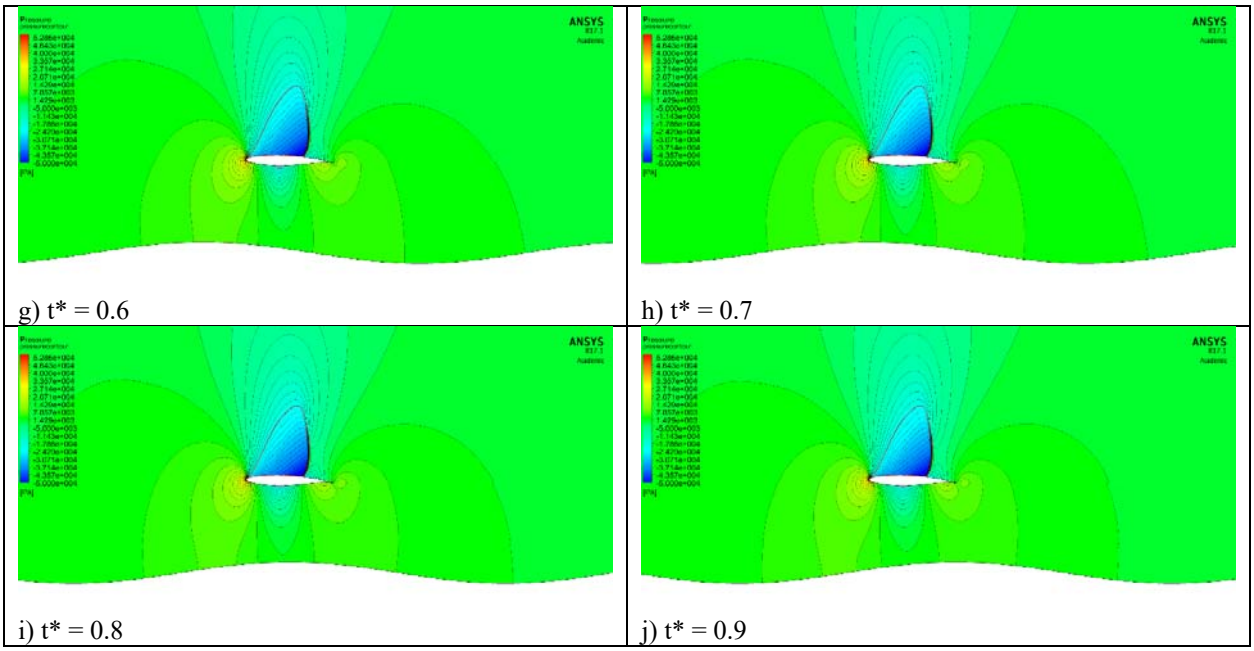

Figure 5.17 Pressure contours of the RAE2822 airfoil at M = 0.8, α = 2 deg and h/c = 1.0 above wavy ground.

Figures 5.16 and 5.17 show the pressure contours and the sonic line of the two cases analyzed. It is clear that despite the Mach number being the same, the reduced ground clearance accelerates the flow passing under the airfoil and thus creating a larger region of locally supersonic flow.

Another case of α = 0 deg, M = 0.8 and h/c = 0.5 is also analyzed due to its unique lower surface shock behavior. The lift and drag coefficient history is shown in Figure 5.18. The lift has a phase lead of 160 degree to the wavy ground which is much larger than in the previous cases. The pressure coefficient plot shows that the positions of both the upper and lower surface shocks remain stationary while the pressure behind the lower surface shock changes periodically. From t* = 0 to 0.4, the pressure behind the lower surface shock increases and then decreases from t* = 0.5 to 0.9. The sonic line shown in Figure 5.20 in red shows that the lower surface shock reaching the ground is periodically changing the height as the wavy ground oscillates.

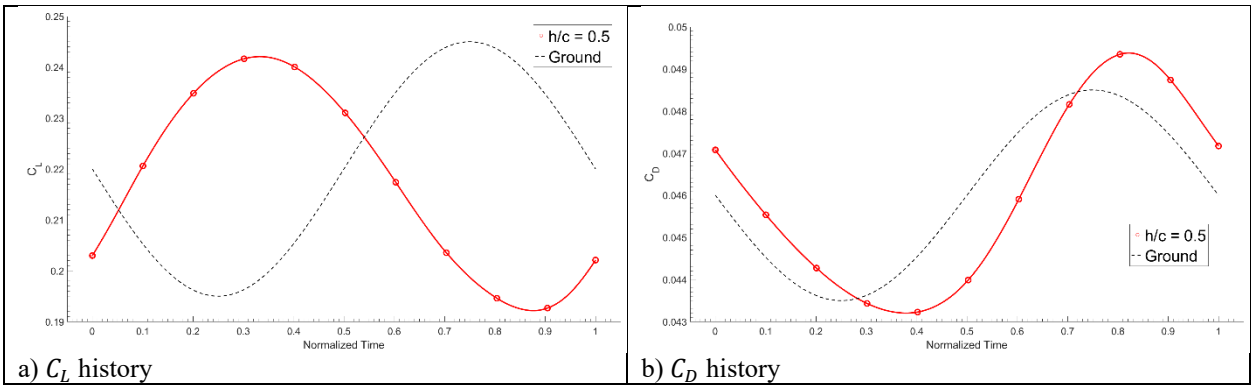

a) C_L history b) C_D history

Figure 5.18 C_L and C_D variation of the RAE2822 airfoil at M = 0.8, α = 0 deg and h/c = 0.5.

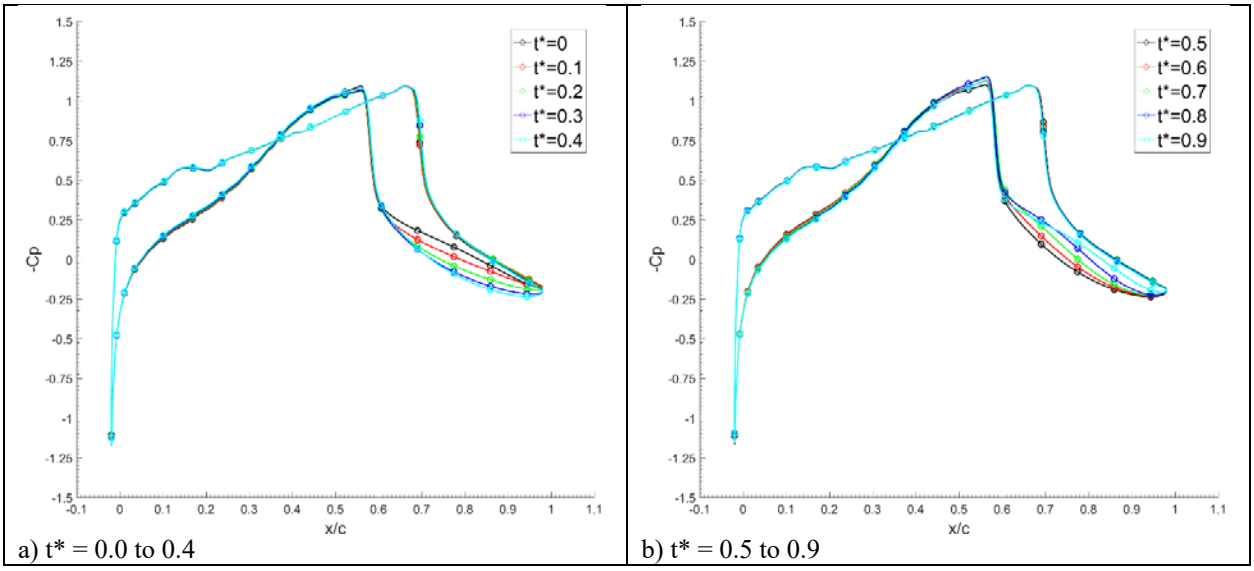

a) t* = 0.0 to 0.4 b) t* = 0.5 to 0.9

Figure 5.19 Pressure coefficient distribution on the RAE2822 airfoil at M = 0.8, α = 0 deg and h/c = 0.5.

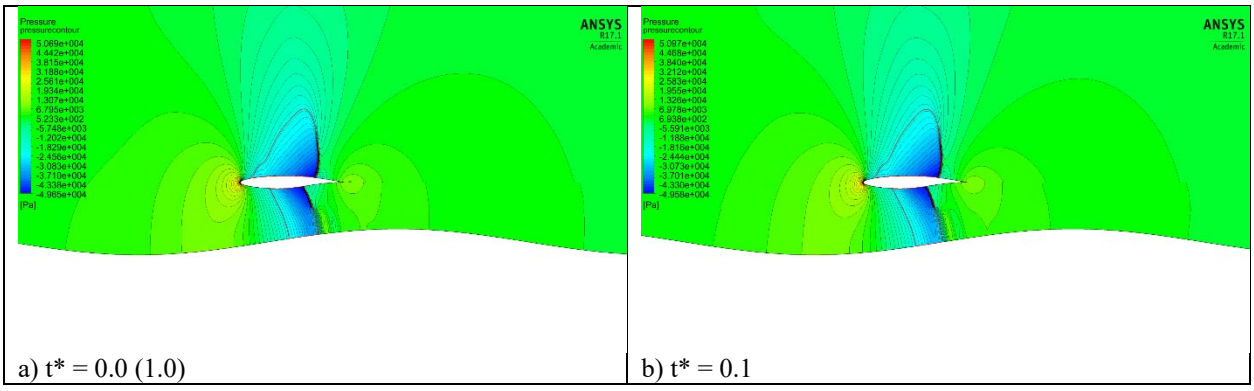

a) t* = 0.0 (1.0) b) t* = 0.1

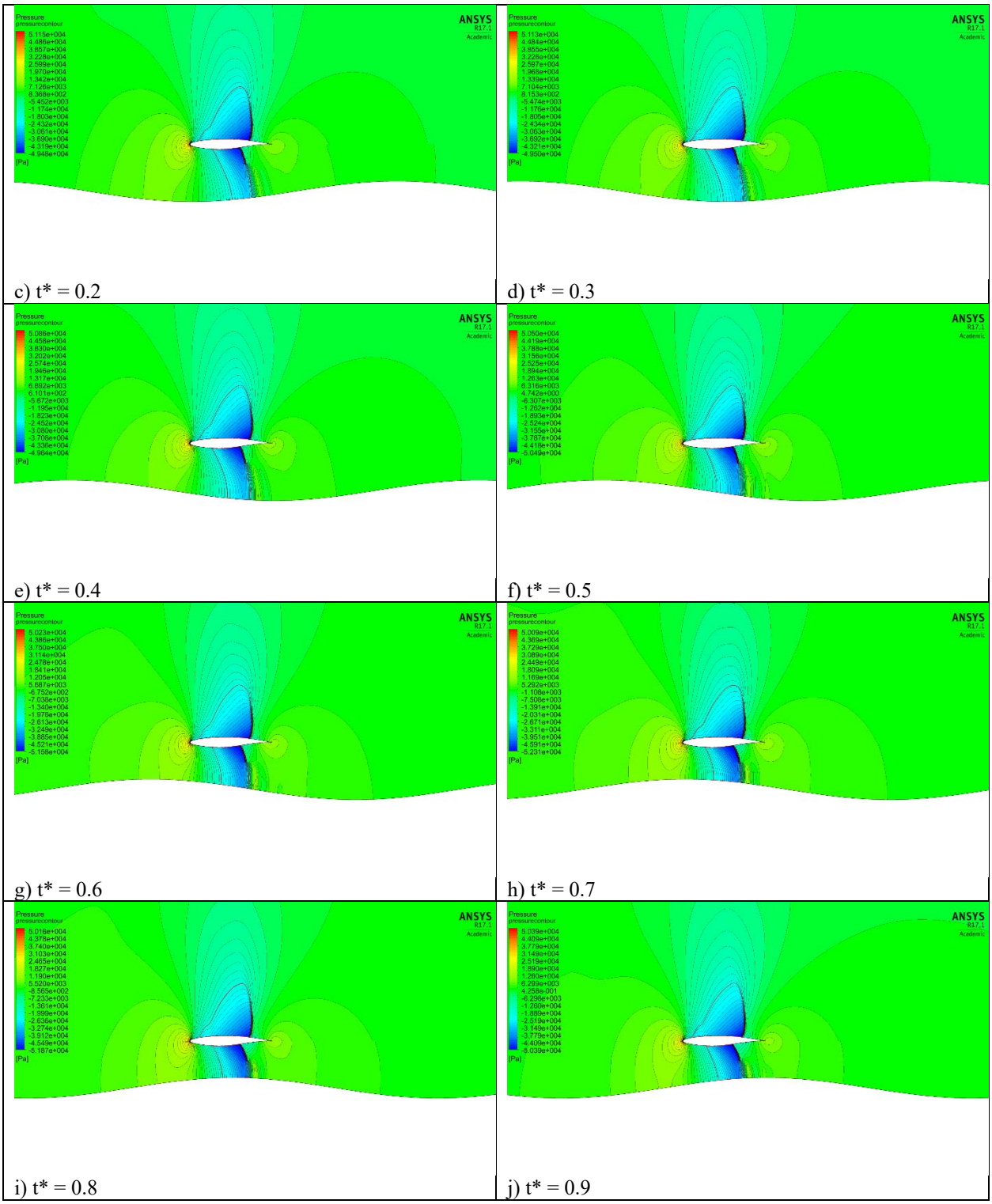

Figure 5.20 Pressure contours and sonic line of the RAE2822 airfoil at M = 0.8, α = 0 deg and h/c = 0.5.

Chapter 6: Conclusion

The flow field of an RAE2822 transonic airfoil in ground effect is simulated at six different angles of attack and four different Mach numbers with ground clearance varying from h/c = ∞ to 0.1. The effect of ground clearance on the shock formation on the airfoil can be classified into two regions based on the appearance of shock on the lower surface of the airfoil: (a) region I of high ground clearance and (b) region II of low ground clearance.

1) In case of high ground clearance, the downward movement of stagnation point moves the shock forward and reduces the strength of the shock. Pressure on the lower surface of the airfoil increases and the pressure on the upper surface decreases. The total lift on the airfoil shows a small increase. Drag on the lower surface of the airfoil increases and the wave drag caused by the shock on the upper surface decreases causing the total drag to decrease. At high angle of attack ranging from α = 6 deg to 12 deg, shock buffet phenomenon is observed with the lift and drag coefficient oscillating nearly 60% in one cycle. The shock buffet is combined with the boundary layer separation due to the shock/boundary layer interaction. The pressure waves behind the trailing edge generate pressure waves which travel upstream and interact with the shock.

2) In case of low ground clearance, the shock on the lower surface of the airfoil appears due to the converging-diverging nozzle like shape between the airfoil and the ground. Streamlines are deflected upward and the suction peak ahead of the shock increases causing the upper surface shock to increase strength. The lift decreases and the drag increases resulting in significant loss in aerodynamic efficiency. At high angle of attack, the shock buffet is present, the mechanism is similar to that for the shock buffet in the high ground clearance case. However, at low angle of attack and high Mach number, another type of shock buffet phenomenon is observed with the lower surface shock interacting with the boundary layer separation causing the pressure on the

lower surface at the trailing edge to oscillate. The pressure on the upper surface varies in accordance with the unsteady-Kutta condition. This coupled shock buffet has been for the first time observed in this thesis and analyzed.

By increasing the angle of attack and thus altering the channel shape, the airfoil can remain in the region of high ground clearance which would avoid the appearance of lower surface shock thereby increasing the aerodynamic efficiency.

Several unsteady phenomenon were also observed in the numerical simulations. The unsteadiness occurs due to shock-boundary layer interaction.

When the airfoil is above the wavy ground, the aerodynamic behavior shows periodic movements at the same frequency but with a phase difference due to the wavy ground. The oscillation amplitude of the aerodynamic forces is smaller compared to the shock buffet phenomenon.

References

[1] Qu, Q. L., Lu, Z., Liu, P. Q., and Agarwal, R. K., "Numerical Study of Aerodynamics of a Wing-in-Ground-Effect Craft," Journal of Aircraft, Vol. 51, No. 3, 2014, pp. 913–924. doi:10.2514/1.C032531

[2] Holloran, M., and O'Meara, S., "Wing in Ground Effect Craft Review", DSTO Aeronautical and Maritime Research Lab., Melbourne, Australia, Feb. 1999.

[3] Qu, Q. L., Jia, X., Wang,W., Liu, P. Q., and Agarwal, R. K., "Numerical Simulation of the Flowfield of an Airfoil in Dynamic Ground Effect," Journal of Aircraft, Vol. 51, No. 5, 2014, pp. 1659–1662. doi:10.2514/1.C032452

[4] Yang, Z. G., and Yang,W., "Complex Flow for Wing-in-Ground Effect Craft with Power Augmented Ram Engine in Cruise," Chinese Journal of Aeronautics, Vol. 23, No. 1, 2010, pp. 1–8. doi:10.1016/S1000-9361(09)60180-1

[5] Rozhdestvensky, K. V., "Wing-in-Ground Effect Vehicles," Progress in Aerospace Sciences, Vol. 42, No. 3, 2006, pp. 211–283. doi:10.1016/j.paerosci.2006.10.001

[6] Jung et al., "Experimental Investigation of Wing-in-Ground Effect with A NACA6409 Section," J Mar. Sci. Tech., Vol. 13, 2008, pp. 317-327, doi:10.1007/s00773-008-0015-4

[7] Zhang, X., and Zerihan, J., "Aerodynamics of a Double-Element Wing in Ground Effect," AIAA Journal, Vol. 41, No. 6, 2003, pp. 1007-1016. doi:10.2514/2.2711

[8] Qu, Q. L., Wang.W, Liu, P. Q., and Agarwal, R. K., "Airfoil Aerodynamics in Ground Effect for Wide Range of Angles of Attack," AIAA Journal, Vol. 53, No. 4, 2015, pp. 1048-1061. doi:10.2514/1.J053366

[9] Yang, Z. G., and Yang,W., "Aerodynamic Investigation of a 2D Wing and Flows in Ground Effect," Chinese Journal of Computational Physics, Vol. 26, No. 2, 2009.

[10] Doig, G., Barber, T.J., Neely. A.J., and Myre, D.D., "Aerodynamics of an Aerofoil in Transonic Ground Effect: Numerical Study at full-scale Reynolds Numbers," The Aeronautical Journal, Vol. 116, No. 1178, 2012, pp. 407-430, doi:10.1017/S0001924000005297

[11] McDevitt, J. B., Levy, L. L., and Deiwert, G. S., "Transonic Flow About a Thick Circular-Arc Airfoil," AIAA Journal, Vol. 14, No. 5, 1976, pp. 606–613.

[12] Levy, L. L., "Experimental and Computational Steady and Unsteady Transonic Flows About a Thick Airfoil," AIAA Journal, Vol. 16, No. 6, 1978, pp. 564–572.

[13] Rumsey, C. L., Sanetrik, M. D., Biedron, R. T., Melson, N. D., and Parlette, E. B., "Efficiency and Accuracy of Time-Accurate Turbulent Navier–Stokes Computation," Computers and Fluids, Vol. 25, No. 2, 1996, pp. 217–236.

[14] Edwards, J. W., "Transonic Shock Oscillations Calculated with a New Interactive Boundary Layer Coupling Method," AIAA Paper 93-0777, 1993.

[15] Oliver, R., Stylvie, P., and Vincent, C., "Numerical Simulation of Buffeting over Airfoil Using Dual Time-Stepping Method," European Congress on Computational Methods in Applied Science and Engineering, Sept. 2000.

[16] Barakos, G., and Drikakis, D., "Numerical Simulation of Transonic Buffet Flows Using Various Turbulence Closures," International Journal of Heat and Fluid Flow, Vol. 21, No. 5, 2000, pp. 620–626.

[17] Bartels, R. E., "Flow and Turbulence Modeling and Computation of Shock Buffet Onset for Conventional and Supercritical Airfoils," NASA TP-1998-206908, Feb. 1998.

[18] Bartels, R. E., and Edwards, J. W., "Cryogenic Tunnel Pressure Measurements on a Supercritical Airfoil for Several Shock Buffet Conditions," NASA TM-110272, 1997.

[19] Lee, B. H. K., "Transonic Buffet on a Supercritical Airfoil," Aeronautic Journal, Vol. 94, No. 935, 1990, pp. 143–152.

[20] Lee, B. H. K., Ellis, F. A., and Bureau, J., "Investigation of the Buffet Characteristics of Two Supercritical Airfoils," Journal of Aircraft, Vol. 26, No. 8, 1989, pp. 731–736.

[21] Lee, B. H. K., "Oscillatory Shock Motion Caused by Transonic Shock Boundary Layer Interaction," AIAA Journal, Vol. 28, No. 5, 1990, pp. 942–944.

[22] Lee, B. H. K., "Self-Sustained Shock Oscillations on Airfoils at Transonic Speeds," Progress in Aerospace Sciences, Vol. 37, No. 2, 2001, pp. 147–196.

[23] Xiao, Q., Tsai, H. M., and Liu, F., "Numerical Study of Transonic Buffet on a Supercritical Airfoil," AIAA Journal, Vol. 44, No. 5, 2006, pp. 620–628.

Appendix A

Journal file of Mesh Generation of RAE2822 Airfoil in ICEM

AOA = angle of attack;

FILE_PATH = path of project file;

MESH_FILENAME = name of generated mesh file;

ic_geo_cre_geom_input {FILE_PATHDown.txt} 0.000001 input PNTS {} Airfoil_down crv SURFS {}

ic_boco_solver

ic_boco_clear_icons

ic_csystem_display all 0

ic_csystem_set_current global

ic_boco_nastran_csystem reset

ic_geo_cre_geom_input {FILE_PATHUp.txt} 0.000001 input PNTS {} Airfoil_up crv SURFS {}

ic_boco_solver

ic_boco_clear_icons

ic_csystem_display all 0

ic_csystem_set_current global

ic_boco_nastran_csystem reset

ic_set_global geo_cad 0 toptol_userset

ic_set_global geo_cad 0.0005 toler

```
ic_geo_new_family FF
ic_boco_set_part_color FF
ic_point {} FF pnt.00 -60,60,0
ic_point {} FF pnt.01 -60,-60,0
ic_point {} FF pnt.02 80,-60,0
ic_point {} FF pnt.03 80,60,0
ic_set_global geo_cad 0.09 toler
ic_delete_geometry curve names crv.00 0
ic_curve point FF crv.00 {pnt.00 pnt.03}
ic_delete_geometry curve names crv.01 0
ic_curve point FF crv.01 {pnt.00 pnt.01}
ic_delete_geometry curve names crv.02 0
ic_curve point FF crv.02 {pnt.03 pnt.02}
ic_geo_new_family GROUND
ic_boco_set_part_color GROUND
ic_delete_geometry curve names crv.03 0
ic_curve point GROUND crv.03 {pnt.01 pnt.02}
ic_set_global geo_cad 0.09 toler
ic_geo_new_family GEOM
ic_boco_set_part_color GEOM
ic_point crv_par GEOM pnt.04 {crv1 0}
ic_point crv_par GEOM pnt.05 {crv1 1}
ic_geo_new_family FLUID
```

ic_boco_set_part_color FLUID

ic_hex_unload_blocking

ic_hex_initialize_mesh 2d new_numbering new_blocking FLUID

ic_hex_switch_blocking root

ic_hex_unblank_blocks

ic_hex_multi_grid_level 0

ic_hex_projection_limit 0

ic_hex_default_bunching_law default 2.0

ic_hex_floating_grid off

ic_hex_transfinite_degree 1

ic_hex_unstruct_face_type one_tri

ic_hex_set_unstruct_face_method uniform_quad

ic_hex_set_n_tetra_smoothing_steps 20

ic_hex_set_mesh_params AIRFOIL_DOWN AIRFOIL_UP FF GROUND GEOM FLUID -

version 110

ic_hex_error_messages off_minor

ic_hex_switch_blocking root

ic_hex_move_node 13 pnt.00

ic_hex_move_node 21 pnt.03

ic_hex_move_node 19 pnt.02

ic_hex_move_node 11 pnt.01

ic_hex_find_comp_curve crv.01

ic_hex_set_edge_projection 11 13 0 1 crv.01

ic_hex_find_comp_curve crv.00

ic_hex_set_edge_projection 13 21 0 1 crv.00

ic_hex_find_comp_curve crv.02

ic_hex_set_edge_projection 19 21 0 1 crv.02

ic_hex_find_comp_curve crv.03

ic_hex_set_edge_projection 11 19 0 1 crv.03

ic_hex_split_grid 11 19 0.427911 m AIRFOIL_DOWN AIRFOIL_UP FF GROUND GEOM FLUID VORFN

ic_hex_split_grid 33 34 0.498876 m AIRFOIL_DOWN AIRFOIL_UP FF GROUND GEOM FLUID VORFN

ic_hex_split_grid 38 34 0.00466771 m AIRFOIL_DOWN AIRFOIL_UP FF GROUND GEOM FLUID VORFN

ic_hex_split_grid 43 44 0.0139933 m AIRFOIL_DOWN AIRFOIL_UP FF GROUND GEOM FLUID VORFN

ic_hex_split_grid 49 44 0.00896465 m AIRFOIL_DOWN AIRFOIL_UP FF GROUND GEOM FLUID VORFN

ic_hex_mark_blocks unmark

ic_hex_mark_blocks superblock 14

ic_hex_mark_blocks superblock 22

ic_hex_mark_blocks superblock 27

ic_hex_mark_blocks numbers 39 44 edge_neighbors

ic_hex_ogrid distance 0.2 fix_dist not_marked m AIRFOIL_DOWN AIRFOIL_UP FF GROUND GEOM FLUID -version 50

ic_hex_mark_blocks unmark

ic_hex_mark_blocks unmark

ic_hex_mark_blocks unmark

ic_hex_mark_blocks superblock 22

ic_hex_mark_blocks superblock 27

ic_hex_collapse_blocks 1 version 410

ic_hex_mark_blocks unmark

ic_hex_mark_blocks unmark

ic_hex_split_grid 58 59 pnt.04 m AIRFOIL_DOWN AIRFOIL_UP FF GROUND GEOM FLUID VORFN

ic_hex_move_node 49 pnt.05

ic_hex_move_node 70 pnt.04

ic_hex_find_comp_curve crv1

ic_hex_set_edge_projection 43 49 0 1 crv1

ic_hex_project_to_surface 43 49

ic_hex_set_edge_projection 70 43 0 1 crv1

ic_hex_project_to_surface 70 43

ic_hex_find_comp_curve crv0

ic_hex_set_edge_projection 38 70 0 1 crv0

ic_hex_project_to_surface 38 70

ic_hex_set_edge_projection 38 49 0 1 crv0

ic_hex_project_to_surface 38 49

ic_hex_set_node_location x 0.04 -csys global node_numbers {{ 43 } { 38 }}

ic_hex_project_to_surface FLUID GEOM FF AIRFOIL_DOWN AIRFOIL_UP GROUND

ic_hex_set_node_location x -0.04 -csys global node_numbers {{ 71 }}

ic_hex_set_node_location x -0.01 y 0.06 -csys global node_numbers {{ 59 }}

ic_hex_set_node_location x -0.01 y -0.06 -csys global node_numbers {{ 58 }}

ic_hex_set_node_location x 1 y 0.05 -csys global node_numbers {{ 61 }}

ic_hex_set_node_location x 1 y -0.05 -csys global node_numbers {{ 60 }}

ic_hex_get_node_location { 61 } _tempx _tempy _tempz

ic_hex_get_node_location { 61 } _tempx _tempy _tempz

ic_hex_set_node_location y {$_tempy} -csys global node_numbers {{ 63 } { 65 }}

ic_hex_get_node_location { 60 } _tempx _tempy _tempz

ic_hex_set_node_location y {$_tempy} -csys global node_numbers {{ 62 } { 64 }}

ic_hex_get_node_location { 49 } _tempx _tempy _tempz

ic_hex_set_node_location x {$_tempx} -csys global node_numbers {{ 61 } { 60 } { 47 }
{ 50 }}

ic_hex_get_node_location { 59 } _tempx _tempy _tempz

ic_hex_set_node_location y {$_tempy} -csys global node_numbers {{ 42 }}

ic_hex_get_node_location { 58 } _tempx _tempy _tempz

ic_hex_set_node_location y {$_tempy} -csys global node_numbers {{ 37 }}

ic_hex_get_node_location { 49 } _tempx _tempy _tempz

ic_hex_set_node_location y {$_tempy} -csys global node_numbers {{ 55 } { 44 }}

ic_hex_set_mesh 59 43 n 2 h1rel 0.0341752987775 h2rel 1.70876493888e-005 r1 1.05 r2 1.05
lmax 0 default copy_to_parallel unlocked

ic_hex_set_mesh 71 59 n 40 h1rel 0.0 h2rel 0.0 r1 2 r2 2 lmax 0 default copy_to_parallel unlocked

ic_hex_set_mesh 71 59 n 40 h1rel 0.0 h2rel 0.0 r1 1.2 r2 1.2 lmax 0 default copy_to_parallel unlocked

ic_hex_set_mesh 58 71 n 40 h1rel 0.0 h2rel 0.0 r1 2 r2 2 lmax 0 default copy_to_parallel unlocked

ic_hex_set_mesh 58 71 n 40 h1rel 0.0 h2rel 0.0 r1 1.2 r2 1.2 lmax 0 default copy_to_parallel unlocked

ic_hex_set_mesh 43 49 n 310 h1rel 0.0 h2rel 0.0 r1 2 r2 2 lmax 0 default copy_to_parallel unlocked

ic_hex_set_mesh 43 49 n 310 h1rel 0.00155508580445 h2rel 0.00103672386963 r1 1.1 r2 1.05 lmax 0 default copy_to_parallel unlocked

ic_hex_set_mesh 61 63 n 9 h1rel 0.0 h2rel 0.0 r1 2 r2 2 lmax 0 default copy_to_parallel unlocked

ic_hex_set_mesh 61 63 n 9 h1rel 0.0 h2rel 0.0 r1 2 r2 2 lmax 0 default copy_to_parallel unlocked

ic_hex_set_mesh 61 63 n 95 h1rel 0.0 h2rel 0.0 r1 2 r2 2 lmax 0 default copy_to_parallel unlocked

ic_hex_set_mesh 61 63 n 95 h1rel 0.00135822876104 h2rel 0.0 r1 1.05 r2 1.1 lmax 0 default copy_to_parallel unlocked

ic_hex_set_mesh 55 44 n 2 h1rel linked 49 55 h2rel 0.0 r1 1.08 r2 1.1 lmax 0 default copy_to_parallel locked

ic_hex_set_mesh 59 34 n 100 h1rel 0.0 h2rel 0.0 r1 2 r2 2 lmax 0 default copy_to_parallel unlocked

ic_hex_set_mesh 59 34 n 100 h1rel 3.002997993e-005 h2rel 0.0 r1 1.1 r2 1.1 lmax 0 default copy_to_parallel unlocked

ic_hex_set_mesh 33 58 n 2 h1rel 0.0 h2rel 3.002997993e-005 r1 1.1 r2 1.1 lmax 0 default copy_to_parallel unlocked

ic_hex_set_mesh 69 71 n 120 h1rel 0.0 h2rel 0.0 r1 2 r2 2 lmax 0 default copy_to_parallel unlocked

ic_hex_set_mesh 69 71 n 120 h1rel 0.0 h2rel linked 71 70 r1 1.08 r2 1.08 lmax 0 default copy_to_parallel locked

ic_hex_list_family_projection

ic_hex_create_mesh AIRFOIL_DOWN AIRFOIL_UP FF GROUND GEOM FLUID proj 2 dim_to_mesh 3 nproc 10

ic_hex_set_mesh 33 58 n 120 h1rel 0.0 h2rel 3.002997993e-005 r1 1.1 r2 1.1 lmax 0 default copy_to_parallel unlocked

ic_hex_set_mesh 33 58 n 120 h1rel 0.0 h2rel 3.002997993e-005 r1 1.1 r2 1.1 lmax 0 default copy_to_parallel unlocked

ic_hex_list_family_projection

ic_hex_create_mesh AIRFOIL_DOWN AIRFOIL_UP FF GROUND GEOM FLUID proj 2 dim_to_mesh 3 nproc 10

ic_hex_set_mesh 59 43 n 120 h1rel 0.0341752987775 h2rel 1.70876493888e-005 r1 1.05 r2 1.05 lmax 0 default copy_to_parallel unlocked

ic_hex_list_family_projection

ic_hex_create_mesh AIRFOIL_DOWN AIRFOIL_UP FF GROUND GEOM FLUID proj 2

dim_to_mesh 3 nproc 10

ic_hex_mark_blocks unmark

ic_hex_mark_blocks superblock 14

ic_hex_mark_blocks superblock 42

ic_hex_change_element_id VORFN

ic_delete_empty_parts

ic_hex_undo_major_start auto_edge_split

ic_hex_auto_split_edge 70 43

ic_hex_auto_split_edge 43 49

ic_hex_auto_split_edge 38 49

ic_hex_auto_split_edge 38 70

ic_hex_undo_major_end auto_edge_split

ic_hex_link_shape 71 59 70 43 1.0

ic_hex_link_shape 58 71 38 70 1.0

ic_hex_link_shape 58 60 38 49 1.0

ic_hex_link_shape 59 61 43 49 1.0

ic_hex_list_family_projection

ic_hex_create_mesh AIRFOIL_DOWN AIRFOIL_UP FF GROUND GEOM FLUID proj 2

dim_to_mesh 3 nproc 10

ic_hex_set_mesh 55 44 n 120 h1rel linked 49 55 h2rel 0.0 r1 1.08 r2 1.1 lmax 0 default

copy_to_parallel locked

ic_hex_set_mesh 55 44 n 120 h1rel linked 49 55 h2rel 0.0 r1 1.08 r2 1.1 lmax 0 default

copy_to_parallel locked

ic_hex_list_family_projection

ic_hex_create_mesh AIRFOIL_DOWN AIRFOIL_UP FF GROUND GEOM FLUID proj 2

dim_to_mesh 3 nproc 10

ic_hex_set_mesh 55 44 n 120 h1rel linked 49 55 h2rel 0.0 r1 1.08 r2 1.1 lmax 0 default

copy_to_parallel locked

ic_hex_set_mesh 55 44 n 120 h1rel 0.000153327787978 h2rel 0.0 r1 1.08 r2 1.1 lmax 0 default

copy_to_parallel locked

ic_hex_list_family_projection

ic_hex_create_mesh AIRFOIL_DOWN AIRFOIL_UP FF GROUND GEOM FLUID proj 2

dim_to_mesh 3 nproc 10

ic_set_global geo_cad 0.09 toler

ic_move_geometry curve names {crv1 crv0} rotate -AOA rotate_axis {0 0 1} cent {0 0 0}

ic_move_geometry point names {pnt.05 pnt.04} rotate -AOA rotate_axis {0 0 1} cent {0 0 0}

ic_geo_reset_data_structures

ic_geo_configure_one_attribute surface shade wire

ic_geo_new_family __TEMP_BLOCK_SUBSET__

ic_hex_create_subset display __TEMP_BLOCK_SUBSET__

ic_hex_subset_add_items __TEMP_BLOCK_SUBSET__ block 6 30 31 32 33 34 41

ic_hex_undo_major_start transform_blocking

ic_hex_transform_blocking root rotate 0 0 0 0 0 1 -AOA m __TEMP_BLOCK_SUBSET__

ic_hex_undo_major_end transform_blocking

ic_geo_delete_family __TEMP_BLOCK_SUBSET__

ic_hex_delete_subset __TEMP_BLOCK_SUBSET__

ic_hex_link_shape 38 70

ic_hex_link_shape 38 49

ic_hex_link_shape 58 38

ic_hex_link_shape 58 71

ic_hex_link_shape 58 60

ic_hex_link_shape 60 49

ic_hex_link_shape 70 43

ic_hex_link_shape 71 70

ic_hex_link_shape 71 59

ic_hex_link_shape 43 49

ic_hex_link_shape 59 43

ic_hex_link_shape 59 61

ic_hex_link_shape 61 49

ic_hex_undo_major_start auto_edge_split

ic_hex_auto_split_edge 43 49

ic_hex_auto_split_edge 70 43

ic_hex_auto_split_edge 38 70

ic_hex_auto_split_edge 38 49

ic_hex_undo_major_end auto_edge_split

ic_hex_list_family_projection

ic_hex_create_mesh AIRFOIL_DOWN AIRFOIL_UP FF GROUND GEOM FLUID proj 2

dim_to_mesh 2 nproc 10

ic_hex_remove_edge_points 38 70

ic_hex_remove_edge_points 38 49

ic_hex_remove_edge_points 58 38

ic_hex_remove_edge_points 58 71

ic_hex_remove_edge_points 58 60

ic_hex_remove_edge_points 60 49

ic_hex_remove_edge_points 70 43

ic_hex_remove_edge_points 71 70

ic_hex_remove_edge_points 71 59

ic_hex_remove_edge_points 43 49

ic_hex_remove_edge_points 59 61

ic_hex_remove_edge_points 59 43

ic_hex_remove_edge_points 61 49

ic_hex_undo_major_start auto_edge_split

ic_hex_auto_split_edge 43 49

ic_hex_auto_split_edge 70 43

ic_hex_auto_split_edge 38 70

ic_hex_auto_split_edge 38 49

ic_hex_undo_major_end auto_edge_split

ic_hex_link_shape 71 59 70 43 1.0

ic_hex_link_shape 58 71 38 70 1.0

ic_hex_link_shape 58 60 38 49 1.0

ic_hex_link_shape 59 61 43 49 1.0

ic_hex_list_family_projection

ic_hex_create_mesh AIRFOIL_DOWN AIRFOIL_UP FF GROUND GEOM FLUID proj 2

dim_to_mesh 2 nproc 10

ic_hex_write_file {FILE_PATHhex.uns} AIRFOIL_DOWN AIRFOIL_UP FF GROUND

GEOM FLUID proj 2 dim_to_mesh 2 no_boco

ic_uns_load C:/Users/Boshun/Desktop/Boshun/RAE2882/GROUND~1/Mesh/hex.uns 3 0 {} 1

ic_uns_update_family_type visible {FLUID GEOM FF AIRFOIL_DOWN ORFN AIRFOIL_UP

GROUND} {!NODE !LINE_2 QUAD_4} update 0

ic_uns_diag_reset_degen_min_max

ic_boco_solver

ic_uns_update_family_type visible {FLUID GEOM FF AIRFOIL_DOWN ORFN AIRFOIL_UP

GROUND} {!NODE !LINE_2 QUAD_4} update 0

ic_boco_clear_icons

ic_csystem_display all 0

ic_csystem_set_current global

ic_boco_nastran_csystem reset

ic_boco_solver {ANSYS Fluent}

ic_solver_mesh_info {ANSYS Fluent}

ic_delete_empty_parts

ic_delete_empty_parts

ic_save_tetin project1.tin 0 0 {} {} 0 0 1

ic_uns_check_duplicate_numbers

ic_save_unstruct project1.uns 1 {} {} {}

ic_uns_set_modified 1

ic_hex_save_blocking project1.blk

ic_boco_solver

ic_boco_solver {ANSYS Fluent}

ic_solution_set_solver {ANSYS Fluent} 1

ic_boco_save project1.fbc

ic_boco_save_atr project1.atr

ic_cart_is_loaded

ic_save_project_file {FILE_PATHproject1.prj} {array\ set\ file_name\ \{ { catia_dir {C:/Users/Boshun/Desktop/Boshun/RAE2882/Ground Effect/Mesh}} { parts_dir {C:/Users/Boshun/Desktop/Boshun/RAE2882/Ground Effect/Mesh}} { domain_loaded 0} { cart_file_loaded 0} { cart_file {}} { domain_saved project1.uns} { archive {}} { med_replay {}} { topology_dir {C:/Users/Boshun/Desktop/Boshun/RAE2882/Ground Effect/Mesh}} { ugparts_dir {C:/Users/Boshun/Desktop/Boshun/RAE2882/Ground Effect/Mesh}} { icons {{$env(ICEM_ACN)/lib/ai_env/icons} {$env(ICEM_ACN)/lib/va/EZCAD/icons} {$env(ICEM_ACN)/lib/icons} {$env(ICEM_ACN)/lib/va/CABIN/icons}}} { tetin project1.tin} { family_boco project1.fbc} { prism_params {}} { iges_dir {C:/Users/Boshun/Desktop/Boshun/RAE2882/Ground Effect/Mesh}} { solver_params_loaded 1} { attributes_loaded 1} { project_lock {}} { attributes project1.atr} { domain project1.uns} { domains_dir .} { settings_loaded 0} { settings project1.prj} { blocking

project1.blk} { hexa_replay {}} { transfer_dir
{C:/Users/Boshun/Desktop/Boshun/RAE2882/Ground Effect/Mesh}} { mesh_dir
{C:/Users/Boshun/Desktop/Boshun/RAE2882/Ground Effect/Mesh}} { family_topo {}}
{ gemsparts_dir {C:/Users/Boshun/Desktop/Boshun/RAE2882/Ground Effect/Mesh}}
{ family_boco_loaded 1} { tetin_loaded 1} { project_dir
{C:/Users/Boshun/Desktop/Boshun/RAE2882/Ground Effect/Mesh}} { topo_mulcad_out {}}
{ solver_params {}} \} array\ set\ options\ \{ { expert 1} { remote_path {}}
{ tree_disp_quad 2} { tree_disp_pyra 0} { evaluate_diagnostic 0} { histo_show_default
1} { select_toggle_corners 0} { remove_all 0} { keep_existing_file_names 0}
{ record_journal 0} { edit_wait 0} { face_mode all} { select_mode all}
{ med_save_emergency_tetin 1} { user_name Boshun} { diag_which all}
{ uns_warn_if_display 500000} { bubble_delay 1000} { external_num 1} { tree_disp_tri
2} { apply_all 0} { default_solver {ANSYS Fluent}} { temporary_directory {}}
{ flood_select_angle 0} { home_after_load 1} { project_active 0}
{ histo_color_by_quality_default 1} { undo_logging 1} { tree_disp_hexa 0}
{ histo_solid_default 1} { host_name CFD128-1} { xhidden_full 1}
{ replay_internal_editor 1} { editor notepad} { mouse_color orange} { clear_undo 1}
{ remote_acn {}} { remote_sh csh} { tree_disp_penta 0} { n_processors 10}
{ remote_host {}} { save_to_new 0} { quality_info Quality} { tree_disp_node 0}
{ med_save_emergency_mesh 1} { redtext_color red} { tree_disp_line 0}
{ select_edge_mode 0} { use_dlremote 0} { max_mesh_map_size 1024} { show_tris 1}
{ remote_user {}} { icon_size Normal} { enable_idle 0} { auto_save_views 1}
{ max_cad_map_size 512} { display_origin 0} { uns_warn_user_if_display 1000000}

{ detail_info 0} { win_java_help 0} { show_factor 1} { boundary_mode all}
{ clean_up_tmp_files 1} { auto_fix_uncovered_faces 1} { med_save_emergency_blocking
1} { max_binary_tetin 0} { tree_disp_tetra 0} \} array\ set\ disp_options\
\{ { uns_dualmesh 0} { uns_warn_if_display 500000} { uns_normals_colored 0}
{ uns_icons 0} { uns_locked_elements 0} { uns_shrink_npos 0} { uns_node_type None}
{ uns_icons_normals_vol 0} { uns_bcfield 0} { backup Wire} { uns_nodes 0}
{ uns_only_edges 0} { uns_surf_bounds 0} { uns_wide_lines 0} { uns_vol_bounds 0}
{ uns_displ_orient Triad} { uns_orientation 0} { uns_directions 0} { uns_thickness 0}
{ uns_shell_diagnostic 0} { uns_normals 0} { uns_couplings 0} { uns_periodicity 0}
{ uns_single_surfaces 0} { uns_midside_nodes 1} { uns_shrink 100}
{ uns_multiple_surfaces 0} { uns_no_inner 0} { uns_enums 0} { uns_disp Wire}
{ uns_bcfield_name {}} { uns_color_by_quality 0} { uns_changes 0}
{ uns_cut_delay_count 1000} \} {set icon_size1 24} {set icon_size2 35} {set
thickness_defined 0} {set solver_type 1} {set solver_setup 1} array\ set\ prism_values\
\{ { n_triangle_smoothing_steps 5} { min_smoothing_steps 6}
{ first_layer_smoothing_steps 1} { new_volume {}} { height {}} { prism_height_limit
{}} { interpolate_heights 0} { n_tetra_smoothing_steps 10} { do_checks {}}
{ delete_standalone 1} { ortho_weight 0.50} { max_aspect_ratio {}} { ratio_max {}}
{ incremental_write 0} { total_height {}} { use_prism_v10 0} { intermediate_write 1}
{ delete_base_triangles {}} { ratio_multiplier {}} { verbosity_level 1}
{ refine_prism_boundary 1} { max_size_ratio {}} { triangle_quality {}}
{ max_prism_angle 180} { tetra_smooth_limit 0.30000001} { max_jump_factor 5}
{ use_existing_quad_layers 0} { layers 3} { fillet 0.1} { into_orphan 0}

{ init_dir_from_prev {}} { blayer_2d 0} { do_not_allow_sticking {}} { top_family {}} { law exponential} { min_smoothing_val 0.1} { auto_reduction 0} { stop_columns 1} { stair_step 1} { smoothing_steps 12} { side_family {}} { min_prism_quality 0.0099999998} { ratio 1.2} \} {set aie_current_flavor {}} array\ set\ vid_options\ \{ { wb_import_mat_points 0} { wb_NS_to_subset 0} { wb_import_surface_bodies 1} { wb_import_cad_att_pre {SDFEA;DDM}} { wb_import_mix_res_line 0} { wb_import_tritol 0.001} { auxiliary 0} { wb_import_cad_att_trans 1} { wb_import_mix_res -1} { wb_import_mix_res_surface 0} { show_name 0} { wb_import_solid_bodies 1} { wb_import_delete_solids 0} { wb_import_mix_res_solid 0} { wb_import_save_pmdb {}} { inherit 0} { default_part GEOM} { new_srf_topo 1} { wb_import_associativity_model_name {}} { DelPerFlag 0} { show_item_name 0} { wb_import_line_bodies 0} { wb_import_save_partfile 0} { wb_import_analysis_type 3} { composite_tolerance 1.0} { wb_NS_to_entity_parts 0} { wb_import_en_sym_proc 1} { wb_run_mesher tetra} { wb_import_sel_proc 1} { wb_import_work_points 0} { wb_import_reference_key 0} { wb_import_mix_res_point 0} { wb_import_pluginname {}} { wb_NS_only 0} { wb_import_geom 1} { wb_import_create_solids 0} { wb_import_refresh_pmdb 0} { wb_import_sel_pre {}} { wb_import_scale_geo Default} { wb_import_load_pmdb {}} { replace 0} { wb_import_cad_associativity 0} { same_pnt_tol 1e-4} { tdv_axes 1} { wb_import_mesh 0} { vid_mode 0} { DelBlkPerFlag 0} \} array\ set\ map_tetin_sizes\ \{ { densities 1} { msurfaces 1} { ppoint 1} { thincuts 1} { tetin {}} { psurfaces 1} { mcurves 1} { mpoint 1} { doit 0} { pcurves 1} { global 1} { subsets 1} { family 1} \} array\ set\ import_model_options\ \{ { from_source 0} { always_ref_key 0} { always_convert 0} { named_sel_only 0}

{ always_create_mpoint 1} { always_import 0} { convert_to Unitless} \} {set savedTreeVisibility {geomNode 1 geom_subsetNode 0 geomPointNode 2 geomCurveNode 2 meshNode 1 mesh_subsetNode 2 meshPointNode 0 meshLineNode 0 meshShellNode 2 meshQuadNode 2 blockingNode 1 block_subsetNode 2 block_vertNode 0 block_edgeNode 2 block_faceNode 0 block_blockNode 0 block_meshNode 0 topoNode 2 topo-root 2 partNode 2 part-AIRFOIL_DOWN 2 part-AIRFOIL_UP 2 part-FF 2 part-FLUID 2 part-GEOM 2 part-GROUND 2 part-VORFN 0}} {set last_view {rot {0 0 0 1} scale {132.964023666 132.964023666 132.964023666} center {10.0 0.0 0.0} pos {1224.34544603 -1.9194203072 0}}} array\ set\ cut_info\ \{ { active 0} \} array\ set\ hex_option\ \{ { default_bunching_ratio 2.0} { floating_grid 0} { project_to_topo 0} { n_tetra_smoothing_steps 20} { sketching_mode 0} { trfDeg 1} { wr_hexa7 0} { smooth_ogrid 0} { find_worst 1-3} { hexa_verbose_mode 0} { old_eparams 0} { uns_face_mesh_method uniform_quad} { multigrid_level 0} { uns_face_mesh one_tri} { check_blck 0} { proj_limit 0} { check_inv 0} { project_bspline 0} { hexa_update_mode 1} { default_bunching_law BiGeometric} { worse_criterion Quality} \} array\ set\ saved_views\ \{ { views {}} \}}

{ICEM CFD}

ic_exec {C:/Program Files/ANSYS Inc/v171/icemcfd/win64_amd/icemcfd/output-interfaces/fluent6} -dom {FILE_PATH/project1.uns} -b project1.fbc -dim2d {FILE_PATHMESH-FILENAME}

Appendix B

MATLAB Code and State file for batch CFD Results Post-processing

Matlab Code:

```
clc;
clear;
%Read cse original
% str_ori=fileread(CSEFILE.cse');
M=0.45:0.05:0.8;
angle=0:1:12;
ratio_name=[0.1,0.2,0.4,0.6,0.8,1,1000];

for a=1:length(angle)
    for r=1:length(ratio_name)
        for m=1:length(M)
            %Define varible names and path
            if ratio_name(r) ~= 1000
                filename_all=['angle',num2str(angle(a)),'ratio',num2str(ratio_name(r)),'-
M=',num2str(M(m))];
                data_location=['C:/Users/Boshun/Desktop/Boshun/RAE2882/Ground Effect/Fluent
Cases/alpha=',num2str(angle(a)),'/h to c=',num2str(ratio_name(r)),'/M=',num2str(M(m)),'/'];
            else
```

```
        %Free flow
        filename_all=['angle',num2str(angle(a)),'ratioinf-M=',num2str(M(m))];
        data_location=['C:/Users/Boshun/Desktop/Boshun/RAE2882/Ground Effect/Fluent
Cases/alpha=',num2str(angle(a)),'/free flow/M=',num2str(M(m)),'/'];
    end

    %Judge if the folder exists
    command=['cd ',data_location];
    [status,cmdout] = system(command);
    if status == 0
       cd (data_location)
       [status,dir] = system('dir /ON');
       %Should match the No. of DATA file(s)
       N=length(strfind(dir,'.dat'));

       if N >10
          %Unsteady

          %Define other varibles
          k=strfind(dir,'.dat');
          caselocation=strfind(dir,'.cas');
          digits=8; %x.6 (may require change)
          %Beginning of the time
```

```
data_start=str2double(dir((k(1)-digits):(k(1)-1)));
%Ending of the time
data_ending=str2double(dir((k(end)-digits):(k(end)-1)));
%Time step between cases
data_step=(data_ending-data_start)/(length(k)-1);


%File_prefix
temp=dir(caselocation-25:caselocation);
space=strfind(temp,' ')+1;
filename_prefix=[temp(space:end-1),'-'];
%Write
for i=1:N
   filename_change = num2str(data_start+(i-1)*data_step,'%1.6f');
   cse_filename = [filename_prefix,filename_change,'.cse'];
   fileID = fopen(cse_filename,'w');
   str = strrep(str_ori,'case_file',[data_location,filename_prefix,filename_change]);
   str = strrep(str,'output_file',[data_location,filename_prefix,filename_change]);
   fprintf(fileID,str);
   fclose(fileID);
end
%Change dir and being CFD-POST
for i=1:N
   filename_change = num2str(data_start+(i-1)*data_step,'%1.6f');
```

```
            cd 'C:\Program Files\ANSYS Inc\v171\CFD-Post\bin'
            cse_filename = [filename_prefix,filename_change,'.cse'];
            command=['cfdpost -batch "',data_location,cse_filename,""];
            [status,cmdout] = system(command,'-echo');
            fprintf('Ratio = %2.1f, angle=%2.0f M = %1.2f is unsteady. Total of %1.0f
cases, %1.0f cases to go.\n',ratio_name(r),angle(a),M(m),N,N-i+1);
        end
        %Clear temp data
        cd (data_location)
        for i=1:N
            filename_change = num2str(data_start+(i-1)*data_step,'%1.6f');
            cse_filename = [filename_prefix,filename_change,'.cse'];
            delete (cse_filename)
        end
    elseif N <= 10 && N >= 1
        %Judge how well the convergence is achieved by reading
        %either cl or cm
        cd (data_location)
        [status,dir] = system('dir /ON');
        clornot=length(strfind(dir,'cl-1-history'));
        %No cl-1-history, then cm-1-history
        if clornot == 0
            filename = [data_location,'cm-1-history.txt'];
```

```
            delimiter = ' ';
            startRow = 3;
            formatSpec = '%f%f%[^\n\r]';
            fileID = fopen(filename,'r');
            dataArray = textscan(fileID, formatSpec, 'Delimiter', delimiter,
'MultipleDelimsAsOne', true, 'EmptyValue' ,NaN,'HeaderLines' ,startRow-1, 'ReturnOnError',
false);
            fclose(fileID);
            convergence_varible = dataArray{:, 2};
            clearvars filename delimiter startRow formatSpec fileID dataArray ans;
        else
            %cl-1-history exists, then use cl data
            filename = [data_location,'cl-1-history.txt'];
            delimiter = ' ';
            startRow = 3;
            formatSpec = '%f%f%[^\n\r]';
            fileID = fopen(filename,'r');
            dataArray = textscan(fileID, formatSpec, 'Delimiter', delimiter,
'MultipleDelimsAsOne', true, 'EmptyValue' ,NaN,'HeaderLines' ,startRow-1, 'ReturnOnError',
false);
            fclose(fileID);
            convergence_varible = dataArray{:, 2};
            clearvars filename delimiter startRow formatSpec fileID dataArray ans;
```

```
            end
            %Judged by the last 200 iterations or timesteps
            convergence_varible=convergence_varible(end-200:end);
            %Percentage of the convergence
            convergence=(max(convergence_varible)-
min(convergence_varible))/mean(convergence_varible)*100;
            clearvars convergence_varible

            if abs(convergence) < 1
               %Steady
               cse_filename = [filename_all,'.cse'];
               fileID = fopen(cse_filename,'w');
               str = strrep(str_ori,'case_file',[data_location,filename_all]);
               str = strrep(str,'output_file',[data_location,filename_all]);
               fprintf(fileID,str);
               fclose(fileID);
               cd 'C:\Program Files\ANSYS Inc\v171\CFD-Post\bin'
               command=['cfdpost -batch "',data_location,cse_filename,""];
               [status,cmdout] = system(command,'-echo');
               fprintf('Ratio = %2.1f, angle=%2.0f M = %1.2f is done. Convergence is %1.5f
percent.\n',ratio_name(r),angle(a),M(m),convergence);
               %Clear temp data
               delete ([data_location,cse_filename])
```

```
                else
                    %Unsteady and need more data
                    fprintf('Ratio = %2.1f, angle=%2.0f M = %1.2f is unsteady and need more data.
Oscillation is %1.5f percent.\n',ratio_name(r),angle(a),M(m),convergence);
                end
            elseif N == 0
                %Folder exists, no data file
                fprintf('Ratio = %2.1f, angle=%2.0f M = %1.2f does NOT
exist.\n',ratio_name(r),angle(a),M(m));
            end
            clearvars k space temp caselocation cse_filename data_location dir filename_all i N str
            clearvars status cmdout command fileID
        else
            %Folder does NOT exist
            fprintf('Ratio = %2.1f, angle=%2.0f M = %1.2f does NOT
exist.\n',ratio_name(r),angle(a),M(m));
        end
    end
  end
end
clearvars a angle clornot convergence m M r ratio_name str_ori
cd ('C:\Users\Boshun\Desktop\Boshun\RAE2882\Ground Effect\Post-processing')
```

State file:

COMMAND FILE:

CFX Post Version = 17.1

END

DATA READER:

Clear All Objects = false

Append Results = false

Edit Case Names = false

Multi Configuration File Load Option = Separate Cases

Open in New View = true

Keep Camera Position = true

Load Particle Tracks = true

Construct Variables From Fourier Coefficients = True

Open to Compare = false

Files to Compare =

END

> load filename=case_file.dat, force_reload=true

VIEW:View 1

Camera Mode = User Specified

CAMERA:

Option = Pivot Point and Quaternion

```
    Pivot Point = 10, 29.5295, 0
    Scale = 0.0169909
    Pan = 0, 0
    Rotation Quaternion = 0.279848, -0.364705, -0.115917, 0.880476
  END

END

> update
CONTOUR:Contour 1
  Apply Instancing Transform = On
  Clip Contour = On
  Colour Map = Default Colour Map
  Colour Scale = Linear
  Colour Variable = Mach Number
  Colour Variable Boundary Values = Conservative
  Constant Contour Colour = On
  Contour Range = User Specified
  Culling Mode = No Culling
  Domain List = /DOMAIN GROUP:All Domains
  Draw Contours = On
  Font = Sans Serif
  Fringe Fill = On
  Instancing Transform = /DEFAULT INSTANCE TRANSFORM:Default Transform
  Lighting = On
```

Line Colour = 1, 0, 0

Line Colour Mode = User Specified

Line Width = 4

Location List = symmetry 1

Max = 1

Min = 1

Number of Contours = 2

Show Numbers = Off

Specular Lighting = On

Surface Drawing = Smooth Shading

Text Colour = 0, 0, 0

Text Colour Mode = Default

Text Height = 0.024

Transparency = 0.0

Use Face Values = Off

Value List = 0,1

OBJECT VIEW TRANSFORM:

Apply Reflection = Off

Apply Rotation = Off

Apply Scale = Off

Apply Translation = Off

Principal Axis = Z

Reflection Plane Option = XY Plane

Rotation Angle = 0.0 [degree]

Rotation Axis From = 0 [m], 0 [m], 0 [m]

```
   Rotation Axis To = 0 [m], 0 [m], 0 [m]
   Rotation Axis Type = Principal Axis
   Scale Vector = 1 , 1 , 1
   Translation Vector = 0 [m], 0 [m], 0 [m]
   X = 0.0 [m]
   Y = 0.0 [m]
   Z = 0.0 [m]
  END
END

# Sending visibility action from ViewUtilities
>show /CONTOUR:Contour 1, view=/VIEW:View 1

# Sending visibility action from ViewUtilities
>hide /DEFAULT LEGEND:Default Legend View 1, view=/VIEW:View 1


WIREFRAME:Wireframe
  Apply Instancing Transform = On
  Colour = 0, 0, 0
  Domain List = /DOMAIN GROUP:All Domains
  Edge Angle = 30 [degree]
  Instancing Transform = /DEFAULT INSTANCE TRANSFORM:Default Transform
  Line Colour Mode = Default
  Line Width = 4
```

Show Surface Mesh = Off

OBJECT VIEW TRANSFORM:

Apply Reflection = Off

Apply Rotation = Off

Apply Scale = Off

Apply Translation = Off

Principal Axis = Z

Reflection Plane Option = XY Plane

Rotation Angle = 0.0 [degree]

Rotation Axis From = 0 [m], 0 [m], 0 [m]

Rotation Axis To = 0 [m], 0 [m], 0 [m]

Rotation Axis Type = Principal Axis

Scale Vector = 1 , 1 , 1

Translation Vector = 0 [m], 0 [m], 0 [m]

X = 0.0 [m]

Y = 0.0 [m]

Z = 0.0 [m]

END

END

>setcamera viewport=1, camera=+Z

VIEW:View 1

Camera Mode = User Specified

CAMERA:

```
    Option = Pivot Point and Quaternion
    Pivot Point = 0.2, 0.2, 0
    Scale = 0.7
    Pan = -0.4, 0
    Rotation Quaternion = 0, 0, 0, 1
  END

END

> update
HARDCOPY:
  Antialiasing = On
  Hardcopy Filename = output_file.png
  Hardcopy Format = png
  Hardcopy Tolerance = 0.0001
  Image Height = 1080
  Image Scale = 100
  Image Width = 1920
  JPEG Image Quality = 90
  Screen Capture = Off
  Use Screen Size = Off
  White Background = On
END
>print
```

Curriculum Vita

Boshun Gao

Degrees	M.S. Mechanical Engineering, May 2017 B.S. Xi'an Jiaotong University, Applied Physics, June 2015
Publications	Boshun Gao, Qiulin Qu, and Ramesh K. Agarwal. "Aerodynamics of a Transonic Airfoil in Ground Effect", 35th AIAA Applied Aerodynamics Conference, AIAA AVIATION Forum, (AIAA 2017-3405), 2017, doi: 10.2514/6.2017-3405